QUANTITATIVE ANALYSIS OF CRYSTAL LATTICE AND DEFECTS IN NANOSCALE FUNCTIONAL MATERIALS BY ELECTRON DIFFRACTION

BY

RENLIANG YUAN

DISSERTATION

Submitted in partial fulfillment of the requirements
for the degree of Doctor of Philosophy in Materials Science and Engineering
in the Graduate College of the
University of Illinois Urbana-Champaign, 2021

Urbana, Illinois

Doctoral Committee:

Professor Jian-Min Zuo, Chair and Director of Research
Professor James N. Eckstein
Associate Professor Daniel P. Shoemaker
Assistant Professor Pinshane Y. Huang

ABSTRACT

Crystalline defects are critical to the properties of the material in both desired and undesired ways. In nanoscale functional materials, a small number of defects can change the material performance significantly. Transmission electron microscopy (TEM) has been one of best techniques to study crystalline defects due to its unparalleled spatial resolution. With the rapid advancements in electron detectors, data mining algorithms, and computation power for big data, a new experimental technique in TEM, called scanning electron nanodiffraction (SEND) or four-dimensional (4D) scanning transmission electron microscopy (STEM) or 4D-STEM, is emerging as a powerful way to provide information in both real space and reciprocal space at the same time based on electron nanodiffraction. This thesis aims to develop novel data analysis approaches of SEND datasets for quantitative analysis of crystal lattice and defects, taking advantage of the geometry and intensity of Bragg diffraction, and diffuse scattering in nanobeam diffraction.

First, we develop a powerful and versatile technique for lattice strain mapping using SEND. The measurement of strain is based on determining the Bragg peak positions recorded in the diffraction patterns from a local crystal volume. To address the issue of peak broadening from a focused electron probe, we propose a new method based on circular Hough transform to locate the position of non-uniform diffraction disks for high accuracy. Methods for fitting a 2D lattice to the detected disks for strain calculation are described, including error analysis. We demonstrate our technique on a FinFET device for strain mapping at the spatial resolution of 1 nm and strain precision of ~0.03%. By testing on the experimental and simulated four-dimensional diffraction datasets (4D-DDs), the experimental parameters involved in data acquisition and analysis are thoroughly investigated to construct an optimum strain mapping strategy using SEND.

Next, techniques for training artificial neural networks (ANNs) and convolutional neural networks (CNNs) using simulated dynamical electron diffraction patterns are described. Using the simulated diffraction patterns as input and trained ANNs, we aim for precise determination of crystal structural properties, such as crystal orientation and local strain. Further, by applying the trained ANNs to 4D-DDs collected using SEND or 4D-STEM techniques, the crystal structural properties can be mapped at high spatial resolution. We demonstrate the ANN-enabled possibilities for the analysis of crystal orientation and strain at high precision and benchmark the performance of ANNs and CNNs by comparing with previous methods. A factor of thirty improvement in angular resolution at 0.01˚ (0.16 mrad) or better for orientation mapping, sensitivity at 0.04% or less for strain mapping, and improvements in computational performance are demonstrated.

Lastly, we focus on imaging and characterization of different types of defects. This is demonstrated using SiGe. We explore the possibility to characterize local lattice distortion based on electron diffuse scattering in coherent SEND. Cepstral STEM imaging is proposed and tested on a dislocation core in SiGe to visualize different types of distortion. Using the results from Cepstral STEM, a deep learning-based method is designed to differentiate different types of defects by detecting features in diffuse scattering automatically.

ACKNOWLEDGMENTS

My first and deepest thanks go to my advisor, Prof. Jian-Min Zuo, for his tremendous support and guidance throughout my PhD study. I thank him for giving me the opportunity to study in his group at University of Illinois where I can learn how the real cutting-edge science is supposed to be done. I was lucky to have the privilege to focus on my study while Jim keeps out wind and rain for his students all the time. Research does have ups and downs, but Jim can always put me back on my feet again with his immense knowledge, boundless creativity, perpetual optimism, and everlasting motivation. I benefited not only from what he taught me, but also from his way of thinking, which has been life-changing to me.

I would like to thank all my thesis committee members, Prof. Jim Eckstein, Prof. Danial Shoemaker, and Prof. Pinshane Huang for their time and effort. In addition to their suggestions and guidance for my thesis work, I also learned a lot during previous collaboration with them. Pinshane also taught me all of the basics of electron microscopy when I first started as a graduate student knowing literally nothing about the field. I thank Prof. Robert Averback and Prof. Andre Schleife for serving as examiners of my qualifying exam.

I want to express my gratitude to Dr. Jiong Zhang from Intel Corporation, who is not only the designated mentor of my Intel-funded research project, but also a former Zuo group member and a friend. He shared with me so many insights from tips of tricks of PhD study to how semiconductor industry works, and also provided enormous help during my job search.

I would like to thank Dr. Lingfeng He from Idaho National Laboratory for inviting me to INL to do experiments that are not easily accessible elsewhere. I also wish to thank Dr. Xiang Liu, Dr. Tiankai Yao, and Dr. Xinchang Zhang for their help during my stay at INL.

During my PhD study, I was fortunate to be involved in numerous collaboration projects which allowed me to learn from Dr. Ping Lu from Sandia National Laboratories, Prof. Robert Maass, Dr. Chelsea Liu, Prof. Qian Chen, Dr. Wenxiang Chen, Dr. Cong Xu, Prof. Paul Braun, Prof. Huseyin Sehitoglu, Dr. Florian Brenne, and many others. I also owe a debt of gratitude to all research scientists working diligently at Materials Research Laboratory at U of I, especially Dr. Changqiang Chen, Dr. James Mabon, Dr. Honghui Zhou, and Dr. Waclaw Swiech who trained me on electron microscopes.

I enjoyed the privilege of being part of the Zuo group family. I thank Dr. Bin Jiang for helping me with the microscope, Prof. Yunfeng Shi for teaching me MD simulation, Dr. Hefei Hu for guidance during job search, Dr. Wenpei Gao for persuading me to join the group, Dr. Yifei Meng for teaching me the basics of various experimental techniques and leading me into the world of programming. I enjoyed sitting next to Dr. Yu-Tsun Shao for three years, with whom I discussed all sorts of research topics on a daily basis. My special thanks go to Haw-wen Hsiao and his wife Emily who gave us countless courage and help when my daughter was born. I am grateful to all other group members I have spent time with: Dr. Jihwan Kwon, Dr. Hyuk Park, Dr. Qun Yang, Dr. Xun Zhan, Dr. Yang Hu, Dr. Aram Yoon, Saran Pidaparthy, Kaijun Yin, Thomas Song, Jocelyn Lai, Hengyu Zhou, Yizhe Qin, Fujia Zhao, Chih-Hung Yeh, Qingyang Zhu, Stanley Tou, Haoyang Ni, Jiangchao Qian, and Zhixin Zhang.

Finally, my heartfelt gratitude goes to my family. I thank my parents for their unconditional love and support. I thank my wife, Chengxi, for her consistent love and encouragement that helped me survive all those hardest days. I thank my tiny little lovely daughter, Nicole, for bringing us so much joy that we never expected before, and for not deleting my thesis when messing with my computer.

To My Family

TABLE OF CONTENTS

CHAPTER 1

INTRODUCTION

Modern solid state physics has gained great success in predicting material properties based on the periodic model of atomic arrangement in crystalline solids. However, real crystals are never perfect. They contain various defects that disturb the periodicity and create lattice strain fields, orientation fluctuation, and symmetry breaking. Crystalline defects can modify the properties of the material in both desired and undesired ways. Especially in nanoscale functional materials, a small number of defects can change the material performance in a significant way. When they are introduced in a controllable way by design, the defects are critical to the material's function.

Study of crystalline defects has been one of the major applications of transmission electron microscopy (TEM) since its invention due to the unparallel spatial resolution of the technique. Defects in a crystal disrupt coherent Bragg scattering, leading to the so-called "diffraction contrast" in recorded TEM images. The strain fields around a defect can be visualized using such contrast. With the development of high-resolution electron microscopy (HREM), the atomic arrangement of defects can also be observed directly. Diffraction contrast imaging and HREM are two most popular ways of imaging defects, which have contributed to much of our experimental knowledge of crystalline defects.

With the rapid advancement of scanning transmission electron microscopy (STEM) in both probe forming optics and fast electron detectors, a new experimental technique in TEM is emerging as a powerful way to provide information in both real space and reciprocal space at the same time. The technique is called scanning electron nanodiffraction (SEND) or broadly four-dimensional STEM (4D-STEM), based on the beam configurations with the latter covers both nanobeams and large angle convergent beams. The major task of this thesis is to develop novel approaches for quantitative analysis of crystal lattice and defects at nanoscale based on SEND and advanced data analysis of SEND datasets, taking the advantage of nanobeam diffraction.

In this chapter, we will briefly introduce different types of defects in crystals and traditional ways to image defects. Notable applications of SEND will be reviewed to provide a high-level overview of the technique. We will finish with a summary of the organization of this thesis.

1.1. Defects in Crystals

Defects in crystals can be classified based on their dimensions.

Zero-dimensional (0D) defects are also called point defects. These include defects that alter the crystal lattice at a single site, such as solute or impurity atoms, substitutional or interstitial, and vacancies (Fig. 1.1a). Point defects apply chemical pressure to the lattice creating strain fields in the crystal.

One-dimensional (1D) defects are also called line defects. The most important line defect is dislocation, where a crystal plane terminates inside the crystal along a line of atoms. Two types of dislocations, edge and screw, are shown in Fig. 1.1b. Line defects produce extended strain fields along the line and break some of the crystal symmetries. Dislocations are also associated with lattice bending or local orientation fluctuation. In the 2D projection of a 3D crystal, the 1D defects may appear as 0D or 1D depending on whether the line is parallel to the viewing direction or not.

Two-dimensional (2D) defects are surfaces or interfaces separating two different crystals or crystal grains. Examples of stacking faults and grain boundaries are illustrated in Fig. 1.1c and

d. They can disturb the perfect lattice significantly by breaking the symmetry and introducing domains of different orientations. In 2D projection, the 2D defects may also appear as 1D lines.

Three-dimensional (3D) defects modify the crystal structure over a finite volume (Fig. 1.1e), like precipitates, large voids, or inclusions of second-phase particles. They usually disturb the lattice in all the ways that defects of 0D to 2D do.

Defects play a big role in influencing material properties. In functional materials, defects can also be introduced in a controllable way to enhance or create new properties. In semiconductors, impurities are used to modify the conductivity of the material (Fig. 1.2a) [1]. In high-temperature superconductors, doping is a major tool to tune the superconductivity (Fig. 1.2b) [2]. In nanocrystalline materials, grain boundaries act as pinning sites to dislocation motions, thus making the grain size the most important parameter in controlling the material's strength and hardness (Fig. 1.2c) [3]. The plasticity of crystals, which is critical for metal forming, for example, is governed by dislocation multiplications and avalanches (Fig. 1.2d) [4]. In silicon transistors, by introducing strain fields, carrier mobility can be improved by a large factor (Fig. 1.2e) [5]. On the other hand, the unwanted strain fields created by dislocations will deteriorate the material performance [6].

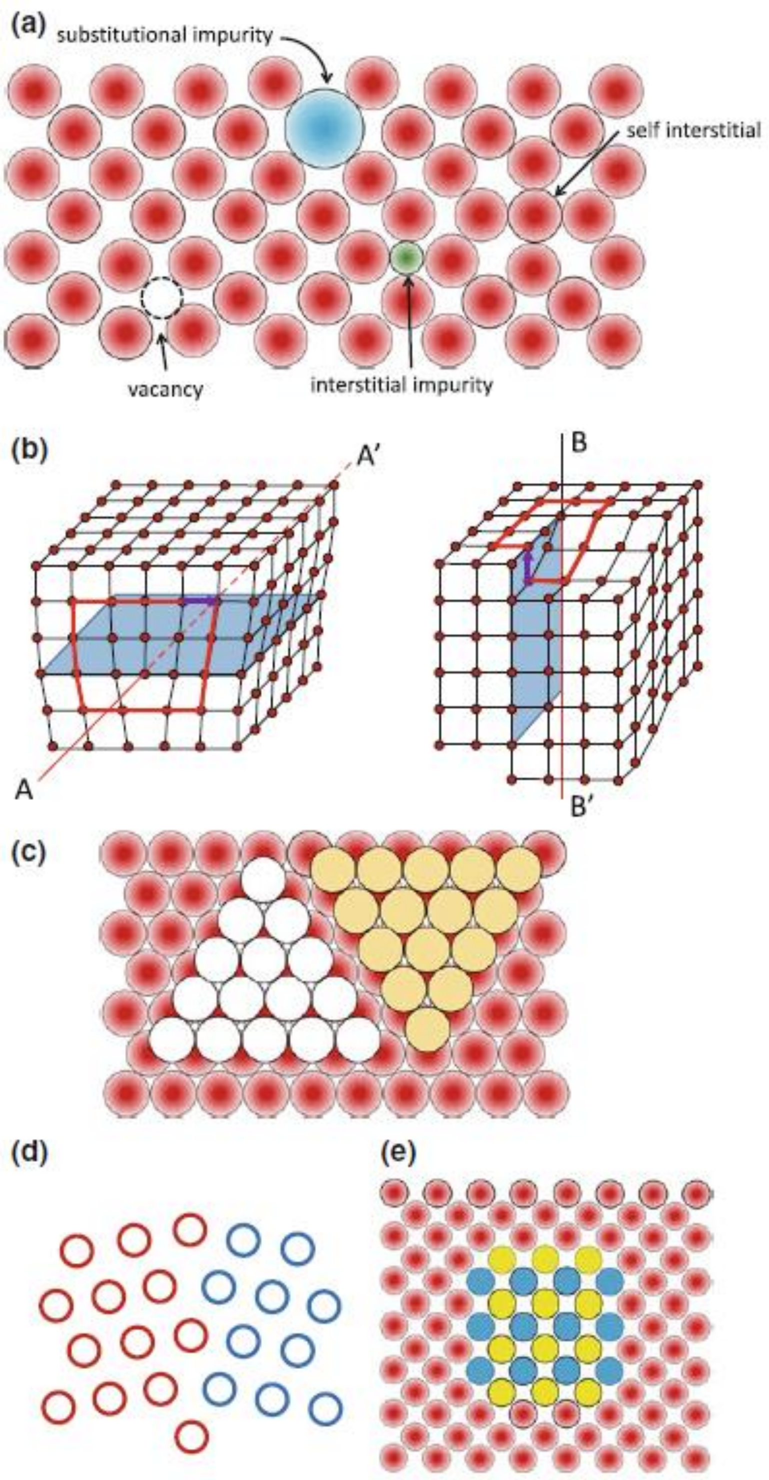

Fig. 1.1. Illustration of different types of crystalline defects. (a) Zero-dimensional defects. (b) One-dimensional defects: edge and screw dislocations. (c) Stacking fault. (d) Grain boundary. (e) Three-dimensional volume defects. (From Zuo et al. [7]).

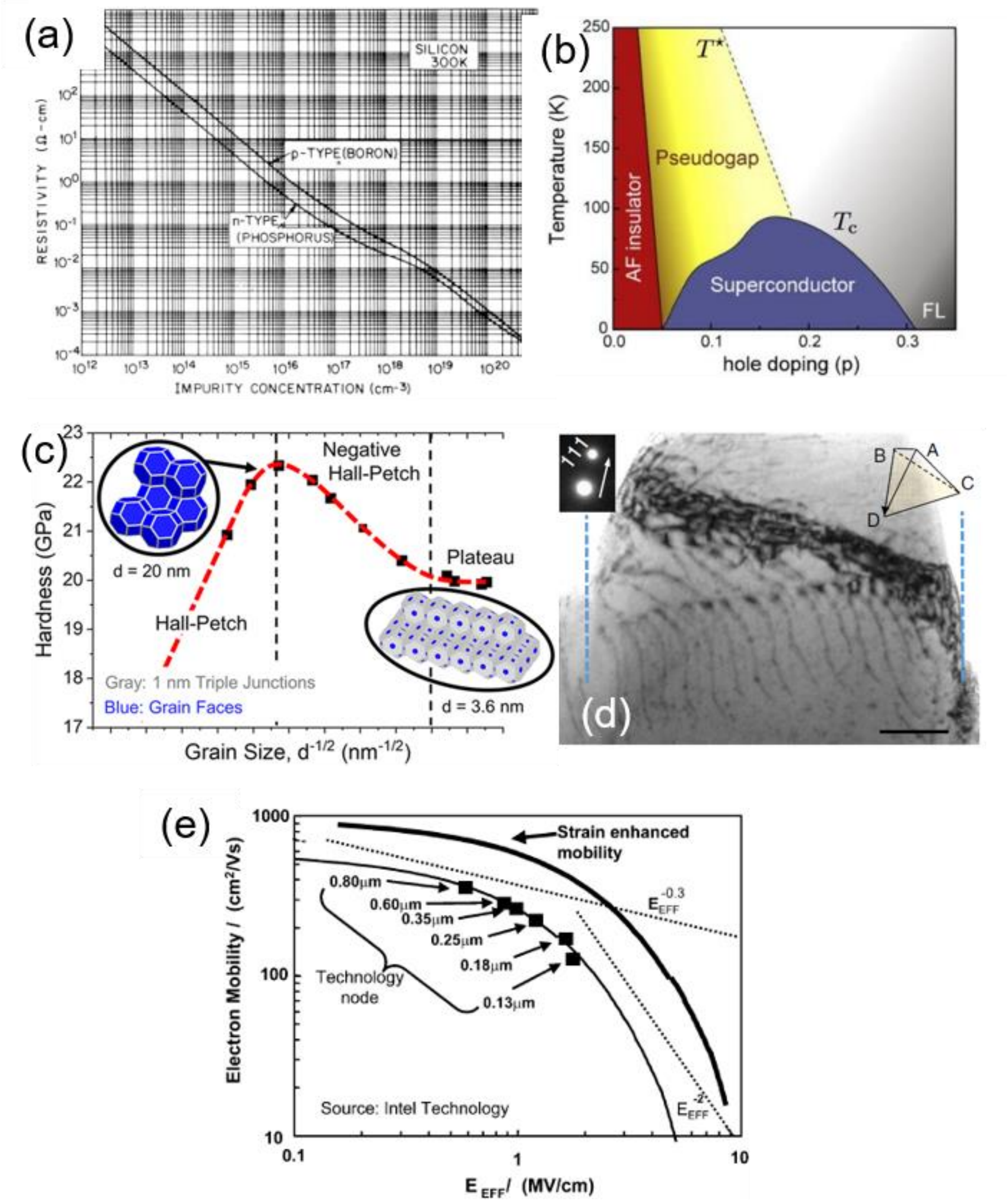

Fig. 1.2. (a) Relationship between resistivity and impurity concentration in silicon [1]. (b) Phase diagram of high-temperature superconductor with doping level as an important parameter [2]. (c) Relationship between material hardness and grain size [3]. (d) Dislocation pileup during crystal deformation [4]. (e) Strain enhanced electron mobility in transistor [5].

1.2. Imaging and Characterization of Crystalline Defects

As described in the previous section, defects in crystals disrupt coherent Bragg scattering from a perfect lattice. Under certain imaging conditions, the disruption will lead to "diffraction contrast" in TEM images formed from a single Bragg beam, which depends on the strain fields around a defect. On the other hand, using many beams for imaging at high resolution, the atomic structure around the defects may be directly observed. These two methods, diffraction contrast imaging and high-resolution electron microscopy (HREM), had been traditionally the most popular experimental techniques to image and characterize defects in crystals in TEM.

The basis for using diffraction contrast imaging for the study of extended defects is the recognition of characteristic contrast produced by the transmitted and diffracted beams under certain diffraction conditions. The theory for such work was largely developed by Hirsch, Howie, Whelan, and others in the 1960s [8]. An important approximation they developed behind the interpretation of diffraction contrast is the column approximation, which assumes that the strain fields change slowly away from the core of defects. And since electron scattering angles are very small, the diffracted intensity in a single-beam dark-field (DF) image can be expressed in terms of the diffracted beam intensity, dependent on the local diffraction conditions. The diffraction intensity is affected by the crystal composition, symmetry, thickness, orientation, defects and strain induced by defects, and other experimental factors. An example of diffraction contrast image is displayed in Fig. 1.3a, where dissociated dislocations in heavily deformed Si are imaged, using the so-called two-beam diffraction condition. Fig. 1.3b shows a variation of diffraction contrast imaging, obtained using the weak-beam technique, where a low-order diffracted beam with a large excitation error is used for imaging. This technique allows individual dislocations to be imaged as relatively intense and narrow peaks to increase the imaging resolution. The DF diffraction contrast images in general are only sensitive to atomic displacements along the lattice plane normal direction. If the atomic displacements around a defect all lie in the same planes used for imaging, the strain field will be invisible in the diffraction contrast technique. This feature can be used to determine the Burgers vector of a dislocation, for example.

Atomic resolution electron imaging is a direct way to study the structure of the defect core when individual atoms can be resolved. Being able to determine the defect core structure, which is very challenging for diffraction contrast imaging, is important for studying the properties of defects. For example, the dislocation core structure is responsible for the friction that the crystal structure offers to dislocation motion (the Peierls stress). The method of diffraction contrast imaging can resolve strain fields around a dislocation as described by the continuum elasticity theory, however, the dislocation core structure, which is not considered by the continuum elasticity theory, has to be determined by atomic resolution imaging, including HREM and STEM, or by simulations such as *ab initio* calculations based on the density functional theory (DFT) [9, 10]. Dislocations are usually observed along the end-on or the normal directions along line AA' or BB' as illustrated in Fig. 1.1b. One example using STEM imaging is displayed in Fig. 1.4, where two partial dislocations associated with a stacking fault are seen in SiGe. Dislocations can also be studied by imaging normal to the dislocation line, which requires additional experimental settings. Two typical approaches have been developed, one uses the forbidden reflections of bulk crystals (Fig. 1.5a) [11] and the other uses the depth-sectioning method based on high-angular annular dark-field (HAADF)-STEM (Fig. 1.5b) [12].

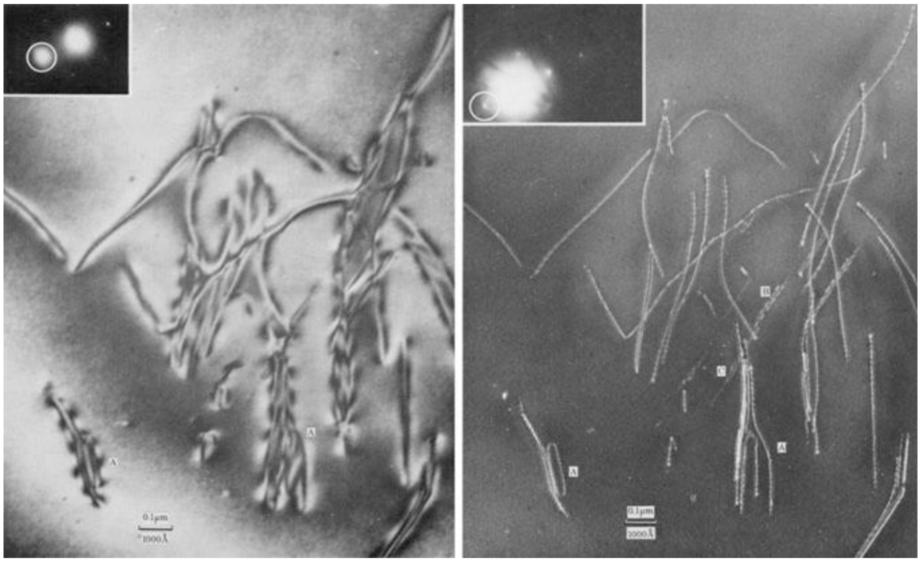

Fig. 1.3. Diffraction contrast imaging of the dislocations in an area of heavily deformed silicon. Left: imaged in a strong 220 diffracted beam. Right: imaged with a weak-beam 220 diffracted beam, which shows a considerable increase in the resolution of the dislocation details (from Ray and Cockayne [13]).

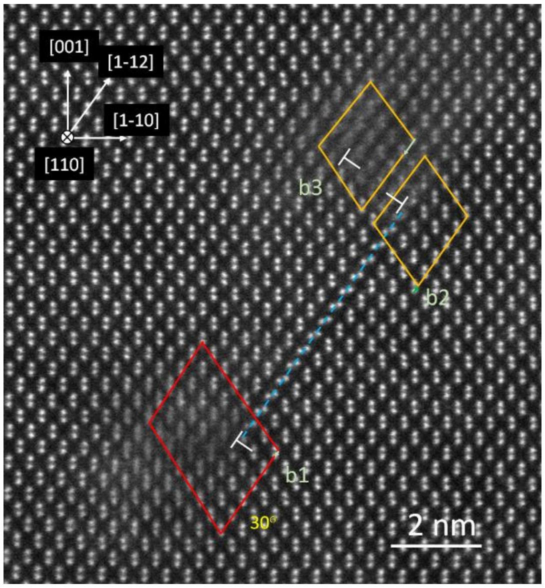

Fig. 1.4. Atomic resolution HAADF-STEM image of dislocations associated with a stacking fault in SiGe.

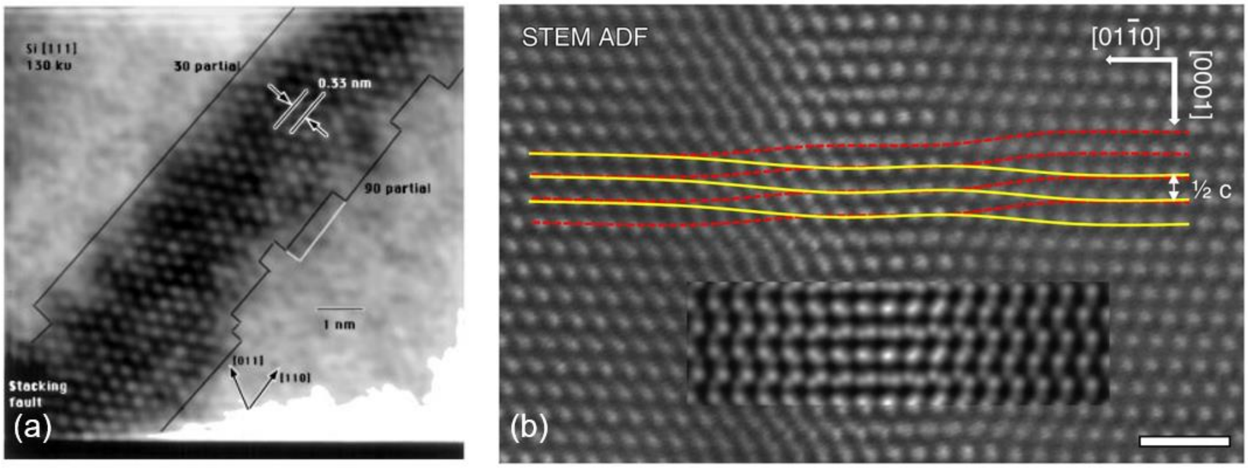

Fig. 1.5. Atomic resolution images of dislocations normal to the dislocation line. (a) TEM image of dissociated 60 degree dislocation in silicon after relaxation [11]. (b) Experimental and simulated ADF image of a dissociated dislocation whose line direction runs up the page [12].

1.3. Scanning Electron Nanodiffraction

Transmission electron diffraction (TED) performed in a TEM provides a highly quantitative way for material structure characterization. To fully utilize the high resolution of the TEM and the quantitative information in diffraction, Cowley [14] first introduced the electron nanodiffraction (END) technique, where the diffraction pattern is taken with the electron probe focused to nm size on the sample. In this way, nanostructures, nanocrystalline materials, defects, and materials' microstructure can be studied locally at the probe size determined spatial resolution, instead of being averaged over a large area illuminated by a spread-out electron beam.

When acquired on a crystalline sample, END patterns contain diffraction peaks which can be directly used to determine lattice parameters, crystal phase, and crystal orientation based on the position and intensity of the peaks. Prof. Zuo at University of Illinois pioneered the work on developing new techniques to extract information from END patterns beyond simple geometry.

Applications include accurate measurement of the structure factor from intensity distribution in convergent beam electron diffraction (CBED) [15, 16], and reconstruction of the atomic structure of nanocrystalline materials using nano-area coherent electron diffraction [17, 18].

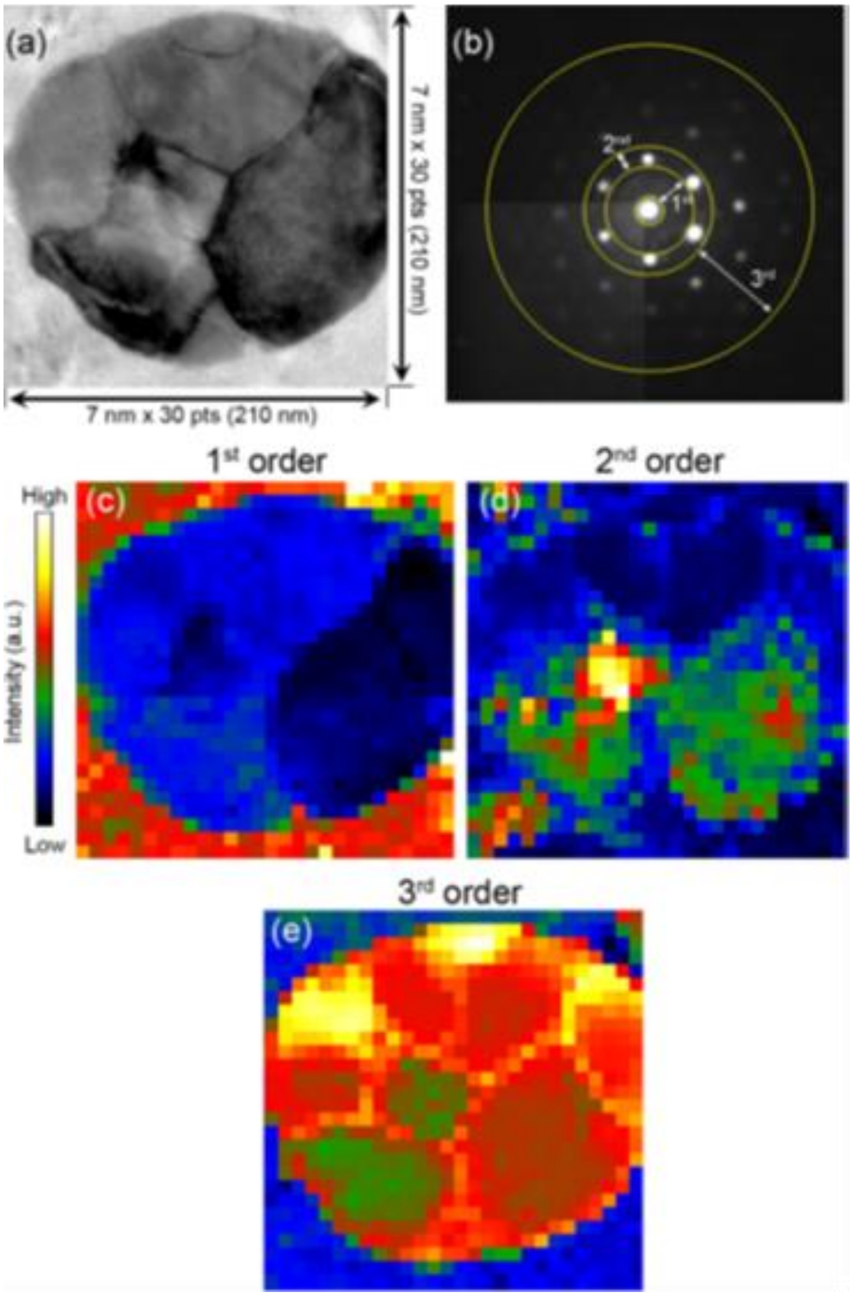

Fig. 1.6. Virtual annular dark-field (ADF) imaging of a nanostructured Au disk [19].

Acquiring multiple END patterns from different regions provide information about structural variations in the sample. This process can be automated by scanning a focused electron probe across a sample region of interest (ROI) in either the TEM mode using the TEM deflection coils [19, 20], or in STEM mode using the STEM scanning coils [21-24] and recording diffraction patterns at each probe position using a pixelated two-dimensional (2D) detector. This technique is called scanning electron nanodiffraction (SEND), which collects a 4D diffraction dataset (4D-DD) in the form of two spatial coordinates, the (x, y) in the real space and the (k_x, k_y) in the reciprocal space [25, 26]. It is also known as 4D-STEM when performed in STEM mode which covers both nanobeams and large angle convergent beams [27].

Once the 4D-DD is collected, several different methods can be employed to extract different information from the data. For example, a virtual aperture can be placed on certain regions of the diffraction patterns, and by integrating the intensity within the aperture, the virtual DF or bright-field (BF) images can be formed. The virtual DF images, similar to DF imaging using a physical objective aperture in TEM mode, or annular dark-field (ADF) imaging using a physical ADF detector in STEM mode. The advantage of having the 4D-DD is that multiple virtual images can be generated that can be used to differentiate different phases or grains and highlight their spatial distribution (Fig. 1.6) [19, 20, 28-31]. Another advantage of SEND over conventional dark-field imaging is that the virtual aperture is not limited to the size and shape of the physical ones. The other way around is to place the virtual aperture on the 2D real space coordinates and collect all the diffraction patterns within this aperture for averaging. A virtual selected area electron diffraction (SAED) pattern can be generated (Fig. 1.7) [31, 32]. The advantage of virtual SAED using 4D-DDs is that the virtual aperture can be designed in arbitrary shapes to cover specific phases, grains or interfaces in the sample, without introducing the extra peaks from other phases.

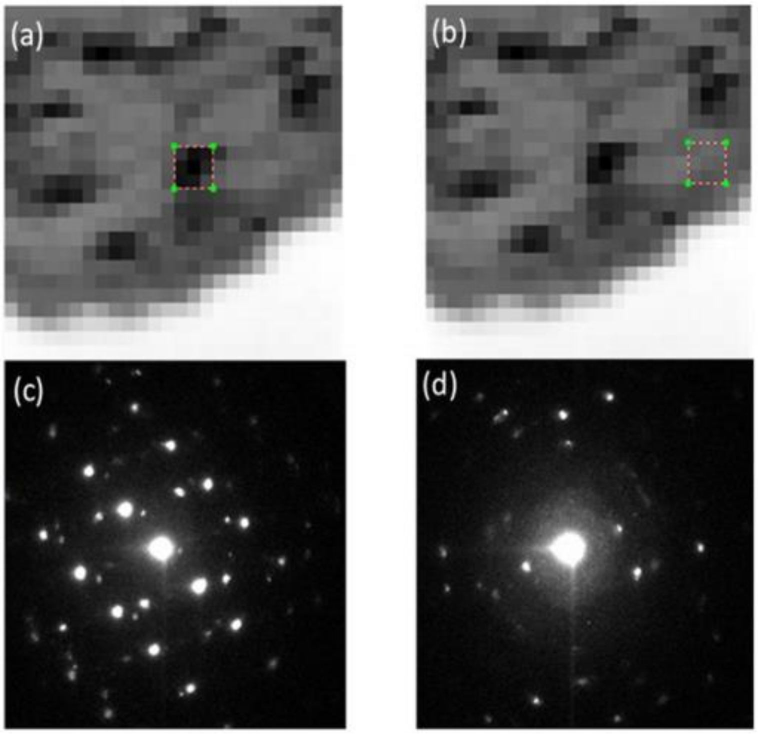

Fig. 1.7. (a)(b) Virtual bright-field (BF) images and (c)(d) virtual selected area electron diffraction (SAED) of a Nb island [32].

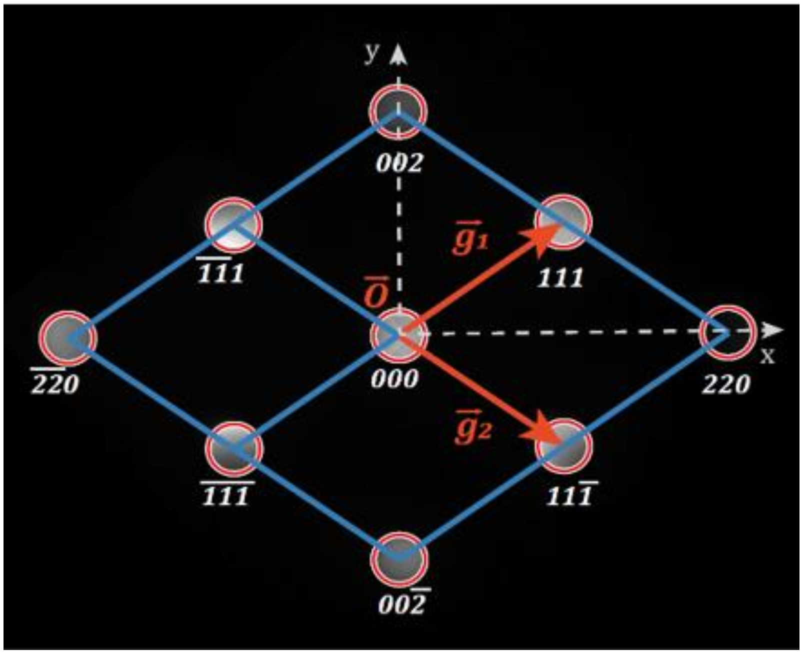

Fig. 1.8. Lattice strain measurement from Bragg diffraction geometry [33].

For SEND carried out on a sample region with several major phases/grains, the similarity between different diffraction patterns in the 4D-DD can be identified by the correlation analysis. After calculating correlation among all patterns, a clustering algorithm can be used to classify all patterns into groups. This helps to generate grain maps from the 4D-DD [30, 34]. Within the same grain, by measuring the relative position of diffraction peaks, lattice strain maps can be calculated (Fig. 1.8) [31, 33, 35]. By comparing the diffraction peak geometry and intensity with theoretical simulation, it is possible to index the diffraction patterns and calculate the orientation map (Fig. 1.9) [34, 36, 37]. When combined with tomographic reconstruction algorithms, 4D-DD taken from multiple tilt angles of the sample can be used to reconstruct nanograin morphology and orientation in 3D (Fig. 1.10) [38]. In CBED patterns, the symmetry of the intensity distribution in CBED disks is very sensitive to the symmetry of the crystal being examined (Fig. 1.11), which can be used to study local symmetry breaking undetectable by X-ray diffraction [39-41]. Other 4D-STEM applications include: position-averaged convergent beam electron diffraction (PACBED) for lattice characterization [42, 43], electric field imaging using differential phase contrast (DPC) imaging [44] or center of mass (COM) of diffraction [45], and high resolution phase reconstruction using ptychography [46-48].

With rapid advancements in electron detector, data mining algorithms and computation power for big data, SEND or 4D-STEM has become an increasingly popular technique for the characterization complex materials. This thesis further pushes forward the state of the art of SEND by developing new and better ways to extract information from the 4D-DD. With the help of SEND, we aim to study crystal lattice and defects more quantitatively where direct imaging methods like diffraction contrast imaging and HREM are limited.

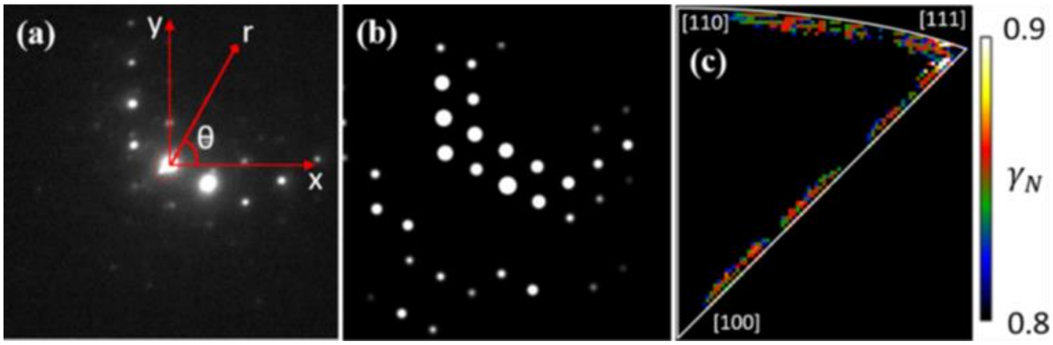

Fig. 1.9. Diffraction pattern indexing by comparing with simulated library for orientation mapping [36].

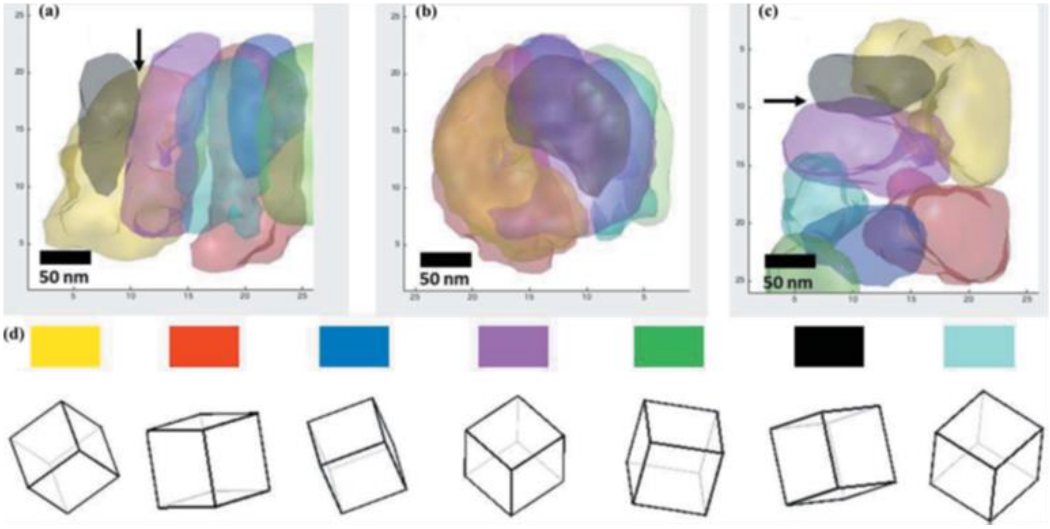

Fig. 1.10. Nanograin morphology and orientation in a nanocrystalline TiN sample determined by 3D-SEND technique [38].

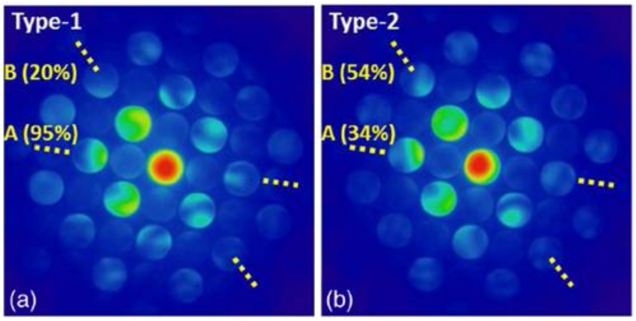

Fig. 1.11. Local crystal symmetry measurement by CBED patterns [40].

1.4. Organization of This Thesis

The remainder of the thesis is organized as follows:

In Chapter 2, we introduce the experimental technique of SEND. We start with the theoretical discussion of focused probe forming in a TEM. Then, the experimental procedure of performing SEND on modern STEM systems is detailed using Thermo Fisher Scientific Themis Z S/TEM microscope as an example. The numerical simulation of SEND patterns considering dynamical effects is also covered in this chapter.

In Chapter 3, we propose a new method for lattice strain mapping by accurately detecting diffraction disks in SEND datasets with dynamical effects. The method is tested and compared with traditional methods on both simulated diffraction patterns and experimental ones to evaluate its accuracy and precision. This chapter is primarily based on Yuan et al. [33].

In Chapter 4, we demonstrate how machine learning, especially supervised learning, can help to deal with complicated dynamic diffraction and large datasets of SEND by training the model with simulated diffraction patterns. The applications include diffraction disk detection for lattice strain measurement and precision orientation mapping of crystals. This chapter is primarily based on Yuan et al. [49].

In Chapter 5, we focus on the material system of SiGe where crystalline defects are critical to the material performance. In addition to the lattice strain mapping technique described in Chapter 3 and 4, we also explore a number of new defect imaging techniques including microprobe STEM imaging, Cepstral STEM imaging [50], and deep learning-based defect classification.

Finally, in Chapter 6, we conclude the thesis and provide future perspectives.

1.5. References

[1] W. Beadle, J. Tsai, R. Plummer, Quick reference manual for silicon integrated circuit technology, Wiley-Interscience, 1985.

[2] B. Vignolle, D. Vignolles, D. LeBoeuf, S. Lepault, B. Ramshaw, R.X. Liang, D.A. Bonn, W.N. Hardy, N. Doiron-Leyraud, A. Carrington, N.E. Hussey, L. Taillefer, C. Proust, Quantum oscillations and the Fermi surface of high-temperature cuprate superconductors, Cr Phys, 12 (2011) 446-460.

[3] H. Ryou, J.W. Drazin, K.J. Wahl, S.B. Qadri, E.P. Gorzkowski, B.N. Feigelson, J.A. Wollmershauser, Below the Hall-Petch Limit in Nanocrystalline Ceramics, Acs Nano, 12 (2018) 3083-3094.

[4] Y. Hu, L. Shu, Q. Yang, W. Guo, P.K. Liaw, K.A. Dahmen, J.M. Zuo, Dislocation avalanche mechanism in slowly compressed high entropy alloy nanopillars, Commun Phys-Uk, 1 (2018).

[5] S.E. Thompson, M. Armstrong, C. Auth, M. Alavi, M. Buehler, R. Chau, S. Cea, T. Ghani, G. Glass, T. Hoffman, C.H. Jan, C. Kenyon, J. Klaus, K. Kuhn, Z.Y. Ma, B. Mcintyre, K. Mistry, A. Murthy, B. Obradovic, R. Nagisetty, P. Nguyen, S. Sivakumar, R. Shaheed, L. Shiften, B. Tufts, S. Tyagi, M. Bohr, Y. El-Mansy, A 90-nm logic technology featuring strained-silicon, Ieee T Electron Dev, 51 (2004) 1790-1797.

[6] X. Chen, D. Zuo, S. Kim, J. Mabon, M. Sardela, J.G. Wen, J.M. Zuo, Large Area and Depth-Profiling Dislocation Imaging and Strain Analysis in Si/SiGe/Si Heterostructures, Microsc Microanal, 20 (2014) 1521-1527.

[7] J.M. Zuo, J.C.H. Spence, Advanced Transmission Electron Microscopy: Imaging and Diffraction in Nanoscience, in, Springer New York New York, NY, 2017.

[8] P.B. Hirsch, Electron microscopy of thin crystals, R. E. Krieger Pub. Co., Huntington, N.Y., 1977.

[9] J.C.H. Spence, Chapter 77 Experimental studies of dislocation core defects, Dislocations in Solids, 13 (2007) 419-452.

[10] D. Rodney, L. Ventelon, E. Clouet, L. Pizzagalli, F. Willaime, Ab initio modeling of dislocation core properties in metals and semiconductors, Acta Mater, 124 (2017) 633-659.

[11] H.R. Kolar, J.C.H. Spence, H. Alexander, Observation of moving dislocation kinks and unpinning, Phys Rev Lett, 77 (1996) 4031-4034.

[12] H. Yang, J.G. Lozano, T.J. Pennycook, L. Jones, P.B. Hirsch, P.D. Nellist, Imaging screw dislocations at atomic resolution by aberration-corrected electron optical sectioning, Nat Commun, 6 (2015).

[13] I.L.F. Ray, D.J. Cockayne, Dissociation of Dislocations in Silicon, Proc R Soc Lon Ser-A, 325 (1971) 543-&.

[14] J.M. Cowley, Electron nanodiffraction: Progress and prospects, J Electron Microsc, 45 (1996) 3-10.

[15] J.M. Zuo, M. Kim, M. O'Keeffe, J.C.H. Spence, Direct observation of d-orbital holes and Cu-Cu bonding in Cu2O, Nature, 401 (1999) 49-52.

[16] J.M. Zuo, Measurements of electron densities in solids: a real-space view of electronic structure and bonding in inorganic crystals, Rep Prog Phys, 67 (2004) 2053-2103.

[17] W.J. Huang, R. Sun, J. Tao, L.D. Menard, R.G. Nuzzo, J.M. Zuo, Coordination-dependent surface atomic contraction in nanocrystals revealed by coherent diffraction, Nat Mater, 7 (2008) 308-313.

[18] J.M. Zuo, I. Vartanyants, M. Gao, R. Zhang, L.A. Nagahara, Atomic resolution imaging of a carbon nanotube from diffraction intensities, Science, 300 (2003) 1419-1421.

[19] K.H. Kim, H. Xing, J.M. Zuo, P. Zhang, H.F. Wang, TEM based high resolution and low-dose scanning electron nanodiffraction technique for nanostructure imaging and analysis, Micron, 71 (2015) 39-45.

[20] J. Tao, D. Niebieskikwiat, M. Varela, W. Luo, M.A. Schofield, Y. Zhu, M.B. Salamon, J.M. Zuo, S.T. Pantelides, S.J. Pennycook, Direct Imaging of Nanoscale Phase Separation in La0.55Ca0.45MnO3: Relationship to Colossal Magnetoresistance, Phys Rev Lett, 103 (2009).

[21] A. Beche, J.L. Rouviere, L. Clement, J.M. Hartmann, Improved precision in strain measurement using nanobeam electron diffraction, Appl Phys Lett, 95 (2009).

[22] F. Uesugi, A. Hokazono, S. Takeno, Evaluation of two-dimensional strain distribution by STEM/NBD, Ultramicroscopy, 111 (2011) 995-998.

[23] K. Muller, A. Rosenauer, M. Schowalter, J. Zweck, R. Fritz, K. Volz, Strain Measurement in Semiconductor Heterostructures by Scanning Transmission Electron Microscopy, Microsc Microanal, 18 (2012) 995-1009.

[24] V.B. Ozdol, C. Gammer, X.G. Jin, P. Ercius, C. Ophus, J. Ciston, A.M. Minor, Strain mapping at nanometer resolution using advanced nano-beam electron diffraction, Appl Phys Lett, 106 (2015).

[25] J.-M. Zuo, J. Tao, Scanning electron nanodiffraction and diffraction imaging, in: Scanning Transmission Electron Microscopy, Springer, 2011, pp. 393-427.

[26] J.-M. Zuo, Electron nanodiffraction, in: Springer Handbook of Microscopy, Springer, 2019, pp. 905-969.

[27] C. Ophus, Four-Dimensional Scanning Transmission Electron Microscopy (4D-STEM): From Scanning Nanodiffraction to Ptychography and Beyond, Microsc Microanal, 25 (2019) 563-582.

[28] H.G. Zhang, H. Ning, J. Busbee, Z.H. Shen, C. Kiggins, Y. Hua, J. Eaves, J. Davis, T. Shi, Y.T. Shao, J.M. Zuo, X.H. Hong, Y. Chan, S.B. Wang, P. Wang, P.C. Sun, S. Xu, J. Liu, P.V. Braun, Electroplating lithium transition metal oxides, Sci Adv, 3 (2017).

[29] J.H. Kwon, Y.F. Meng, L.J. Wu, Y.M. Zhu, Y.F. Zhang, V. Selvamanickam, U. Welp, W.K. Kwok, J.M. Zuo, Extended electronic structure inhomogeneity created by double chain layer defects surrounding columnar tracks in heavy-ion irradiated YBa2Cu3O7-delta, Supercond Sci Tech, 31 (2018).

[30] W. Guo, Y.F. Meng, X. Zhang, V. Bedekar, H.B. Bei, S. Hyde, Q.Y. Guo, G.B. Thompson, R. Shivpuri, J.M. Zuo, J.D. Poplawsky, Extremely hard amorphous-crystalline hybrid steel

surface produced by deformation induced cementite amorphization, Acta Mater, 152 (2018) 107-118.

[31] H.W. Hsiao, S. Li, K.A. Dahmen, J.M. Zuo, Shear banding mechanism in compressed nanocrystalline ceramic nanopillars, Phys Rev Mater, 3 (2019).

[32] M. Durkin, R. Garrido-Menacho, S. Gopalakrishnan, N.K. Jaggi, J.H. Kwon, J.M. Zuo, N. Mason, Rare-region onset of superconductivity in niobium nanoislands, Phys Rev B, 101 (2020).

[33] R. Yuan, J. Zhang, J.-M. Zuo, Lattice strain mapping using circular Hough transform for electron diffraction disk detection, Ultramicroscopy, 207 (2019).

[34] Y. Hu, J.H. Huang, J.M. Zuo, In situ characterization of fracture toughness and dynamics of nanocrystalline titanium nitride films, J Mater Res, 31 (2016) 370-379.

[35] C. Liu, Z. Cai, X. Xia, V. Roddatis, R. Yuan, J.M. Zuo, R. Maass, Shear-band structure and chemistry in a Zr-based metallic glass probed with nano-beam x-ray fluorescence and transmission electron microscopy, Scripta Mater, 169 (2019) 23-27.

[36] Y.F. Meng, J.M. Zuo, Improvements in electron diffraction pattern automatic indexing algorithms, Eur Phys J-Appl Phys, 80 (2017).

[37] E. Mohammadi, C.K. Zhao, Y.F. Meng, G. Qu, F.J. Zhang, X.K. Zhao, J.G. Mei, J.M. Zuo, D. Shukla, Y. Diao, Dynamic-template-directed multiscale assembly for large-area coating of highly-aligned conjugated polymer thin films, Nat Commun, 8 (2017).

[38] Y.F. Meng, J.M. Zuo, Three-dimensional nanostructure determination from a large diffraction data set recorded using scanning electron nanodiffraction, Iucrj, 3 (2016) 300-308.

[39] K.H. Kim, D.A. Payne, J.M. Zuo, Determination of 60 degrees polarization nanodomains in a relaxor-based ferroelectric single crystal, Appl Phys Lett, 107 (2015).

[40] Y.T. Shao, J.M. Zuo, Lattice-Rotation Vortex at the Charged Monoclinic Domain Boundary in a Relaxor Ferroelectric Crystal, Phys Rev Lett, 118 (2017).

[41] Y.T. Shao, J.M. Zuo, Nanoscale symmetry fluctuations in ferroelectric barium titanate, BaTiO3, Acta Crystallogr B, 73 (2017) 708-714.

[42] J.M. LeBeau, S.D. Findlay, L.J. Allen, S. Stemmer, Quantitative atomic resolution scanning transmission electron microscopy, Phys Rev Lett, 100 (2008).

[43] C. Ophus, P. Ercius, M. Huijben, J. Ciston, Non-spectroscopic composition measurements of SrTiO3-La0.7Sr0.3MnO3 multilayers using scanning convergent beam electron diffraction, Appl Phys Lett, 110 (2017).

[44] N. Shibata, T. Seki, G. Sanchez-Santolino, S.D. Findlay, Y. Kohno, T. Matsumoto, R. Ishikawa, Y. Ikuhara, Electric field imaging of single atoms, Nat Commun, 8 (2017).

[45] W.P. Gao, C. Addiego, H. Wang, X.X. Yan, Y.S. Hou, D.X. Ji, C. Heikes, Y. Zhang, L.Z. Li, H.X. Huyan, T. Blum, T. Aoki, Y.F. Nie, D.G. Schlom, R.Q. Wu, X.Q. Pan, Real-space charge-density imaging with sub-angstrom resolution by four-dimensional electron microscopy, Nature, 575 (2019) 480-+.

[46] H. Yang, R.N. Rutte, L. Jones, M. Simson, R. Sagawa, H. Ryll, M. Huth, T.J. Pennycook, M.L.H. Green, H. Soltau, Y. Kondo, B.G. Davis, P.D. Nellist, Simultaneous atomic-resolution

electron ptychography and Z-contrast imaging of light and heavy elements in complex nanostructures, Nat Commun, 7 (2016).

[47] Y. Jiang, Z. Chen, Y.M. Hang, P. Deb, H. Gao, S.E. Xie, P. Purohit, M.W. Tate, J. Park, S.M. Gruner, V. Elser, D.A. Muller, Electron ptychography of 2D materials to deep sub-angstrom resolution, Nature, 559 (2018) 343-+.

[48] S. Gao, P. Wang, F.C. Zhang, G.T. Martinez, P.D. Nellist, X.Q. Pan, A.I. Kirkland, Electron ptychographic microscopy for three-dimensional imaging, Nat Commun, 8 (2017).

[49] R. Yuan, J. Zhang, L. He, J.-M. Zuo, Training artificial neural networks for precision orientation and strain mapping using 4D electron diffraction datasets, Ultramicroscopy, (2021).

[50] Y.-T. Shao, R. Yuan, H.-W. Hsiao, Q. Yang, Y. Hu, J.-M. Zuo, Cepstral Scanning Transmission Electron Microscopy Imaging of Severe Lattice Distortions, Ultramicroscopy, (2021).

CHAPTER 2

SCANNING ELECTRON NANODIFFRACTION

In this chapter, we introduce the experimental technique of scanning electron nanodiffraction (SEND), which is used throughout this thesis. We start with an overview of electron diffraction in TEM. The major features recorded in different types of electron diffraction patterns and how they relate to the structure of materials are presented. After the broader background of diffraction in a TEM, we define the scope of SEND used in this thesis and describe how it is performed experimentally. In the end, two simulation methods for SEND based on dynamical diffraction theory are introduced, which provide important complementary information to the experimental data.

2.1. Transmission Electron Diffraction

In a TEM, a beam of high energy electrons is incident on a thin sample. The incident electrons are scattered because of interactions with the electrons and nuclei within the sample through Coulombic forces. With the wavelength of incident electrons much shorter than atomic spacings within the sample, constructive interference occurs among forward-scattered electron waves, which leads to the formation of transmission electron diffraction (TED) patterns. Quantitative information captured by diffraction patterns can be used to study the atomic structure of materials. The most prominent features in a TED pattern are the geometry and intensity of diffraction spots.

2.1.1. Geometry of Electron Diffraction

A typical TED pattern is formed with a parallel-beam electron illumination, passing through a thin sample. When the sample is crystalline, the diffracted beams give rise to diffraction spots in the detector placed at the far field. The detector used for recording TED patterns in a TEM is usually a two-dimensional (2D) pixelated detector. As a result, the acquired diffraction pattern is a 2D image.

The geometry of a spot diffraction pattern can be simply described based on the Ewald sphere construction as illustrated in Fig. 2.1. The incident wave is represented by a wave vector $\overrightarrow{K_0}$ pointing downward. The length of it is the incident wave number $K_0 \approx 1/\lambda$ and λ is the electron wavelength, which is determined by the electron accelerating voltage, ϕ in volts, according to

$$\lambda = \frac{12.2643}{\sqrt{\phi(1+0.97865\times10^{-6}\phi)}}, \tag{2.1}$$

in angstroms (Å). In this thesis, the most used accelerating voltages are 200kV, corresponding to 0.025079 Å in wavelength, and 300kV, corresponding to 0.019688 Å. Using the incident wave number as the radius, a sphere is constructed, which is called the Ewald sphere (Fig. 2.1). Any diffracted wave vector $\vec{K}$ must fall on the Ewald sphere because of energy conservation. The relationship between the incident wave, the diffracted wave, and the crystalline sample is determined by the Laue diffraction condition,

$$\vec{K} - \overrightarrow{K_0} = \vec{g} + \overrightarrow{S_g}, \tag{2.2}$$

where $\vec{g}$ is a reciprocal lattice vector of the crystal

$$\vec{g} = h\overrightarrow{a^*} + k\overrightarrow{b^*} + l\overrightarrow{c^*}, \tag{2.3}$$

with $\overrightarrow{a^*}$, $\overrightarrow{b^*}$, and $\overrightarrow{c^*}$ are the reciprocal basis vectors of the crystal. And $\overrightarrow{S_g}$ is the so-called excitation error, which describes the deviation from the Bragg condition. At the Bragg condition, $\overrightarrow{S_g} = 0$, while $\overrightarrow{S_g}$ is positive when the length of $\overrightarrow{K_0} + \vec{g}$ is shorted than K_0. The direction of $\overrightarrow{S_g}$ is taken along the sample surface normal direction.

The angle between $\vec{K}$ and $\overrightarrow{K_0}$ determines the distance D between diffraction spots O and g in the 2D diffraction pattern recorded, proportional to camera length L:

$$D = L \tan 2\theta, \tag{2.4}$$

At the Bragg condition, both the origin of the reciprocal lattice and lattice point $\vec{g}$ are on the Ewald sphere, which leads to the famous Bragg's law

$$2d_{hkl} \sin \theta_B = \lambda, \tag{2.5}$$

where d_{hkl} is the interplanar spacing, with $d_{hkl} = \frac{1}{g_{hkl}}$. Thus, once the camera length is calibrated, the lattice spacings of a crystal can be directly calculated from the distances between the corresponding diffraction spots recorded in a diffraction pattern:

$$d_{hkl} = \frac{\lambda L}{D_{hkl}}. \tag{2.6}$$

The ability to measure local d-spacing using a small-diameter electron beam forms the basis of lattice strain measurement, which is described in the following chapters.

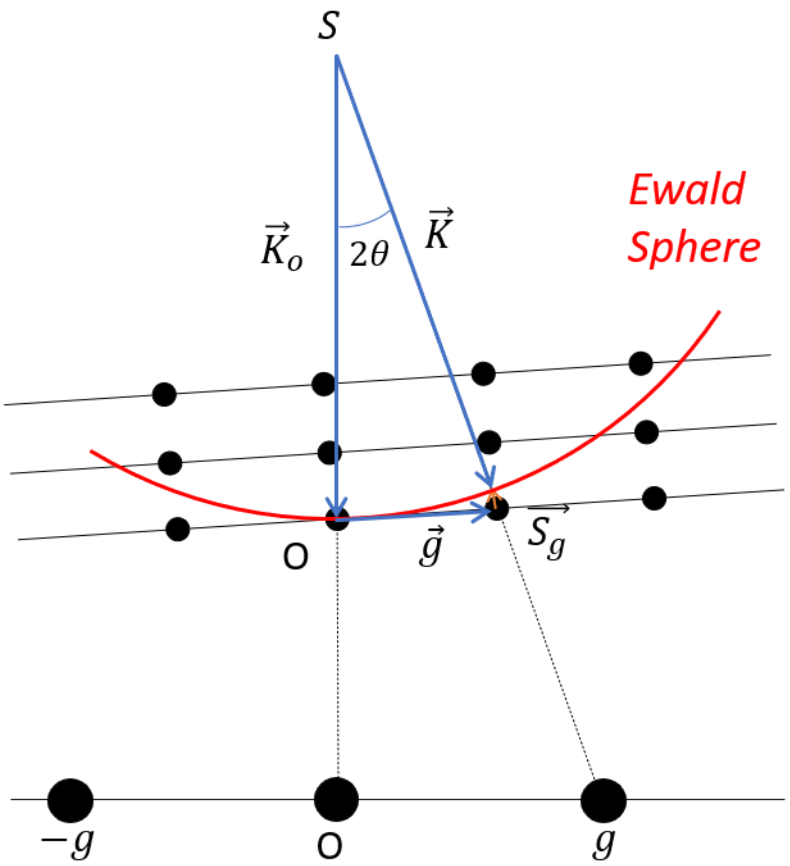

Fig. 2.1. Ewald sphere construction for transmission electron diffraction geometry.

The diffraction spots are expected to stay at their positions with the incident beam direction fixed, while the crystal is rotated by a small angle. This is because the diffraction angle (2θ) remains unchanged. The intensity of the diffraction spot changes as the diffracted beam goes in and out of the Bragg condition. When the crystal is rotated from one zone axis to another, the geometry of diffraction will also change. These features can be used to measure the crystal orientation from the recorded electron diffraction patterns.

2.1.2. Intensity of Electron Diffraction

Electrons are diffracted by interacting with the electrostatic potential $V(\vec{r})$ of the sample, which can be described by the time-independent Schrodinger equation:

$$\frac{1}{4\pi^2}\nabla^2\phi + k^2\phi = -\frac{2me}{h^2}V(\vec{r})\phi = -U(\vec{r})\phi, \tag{2.7}$$

where $k^2 = \frac{2mE}{h^2} = 2me\Phi/h^2$, with Φ denoting the electron accelerating voltage. $U(\vec{r}) = 2meV(\vec{r})/h^2$ is called the interaction potential. By taking $\phi_0(\vec{r}) = e^{2\pi i\overrightarrow{k_0}\cdot\vec{r}}$ for an incident plane wave, Eq. 2.7 can be transformed to:

$$\phi(\vec{r}) = e^{2\pi i\overrightarrow{k_0}\cdot\vec{r}} + \pi\int d^3\overrightarrow{r'}\,\frac{e^{2\pi ik\left|\vec{r}-\overrightarrow{r'}\right|}}{\left\|\vec{r}-\overrightarrow{r'}\right\|}U\left(\overrightarrow{r'}\right)\phi\left(\overrightarrow{r'}\right) \tag{2.8}$$

In the first order Born approximation, the scattered wave (the second term in Eq. 2.8) is assumed to be weak. So the wavefunction inside the integral can be taken approximately as the incident wave $e^{2\pi i\overrightarrow{k_0}\cdot\vec{r}}$. Also by assuming that the detector is placed far away from the object and the object is small, the solution of Eq. 2.8 can be simplified as:

$$\phi(\vec{r}) \approx e^{2\pi i\overrightarrow{k_0}\cdot\vec{r}} + \pi\frac{e^{2\pi ikr}}{r}\int d^3\overrightarrow{r'}e^{-2\pi i\left(\vec{k}-\overrightarrow{k_0}\right)\cdot\vec{r}}U\left(\overrightarrow{r'}\right) \tag{2.9}$$

The total scattered wave is then given by:

$$\phi_s \approx \frac{2\pi me}{h^2}\frac{e^{2\pi ikr}}{r}\int V\left(\overrightarrow{r'}\right)e^{-2\pi i\left(\vec{k}-\overrightarrow{k_0}\right)\cdot\vec{r}}d^3\overrightarrow{r'}, \tag{2.10}$$

which is proportional to the Fourier transform of the potential $V(\vec{r})$.

The use of the first order Born approximation implicitly assumes that only direct scattering from the incident wave contributes to the scattered wave. Therefore, it is also called single scattering, or kinematical, approximation. While the kinematical diffraction theory usually suffices for the X-ray and neutron diffraction analysis, it has been mostly treated as an overly simplified model in electron diffraction, because the typical experimental electron diffraction conditions do involve strong multiple scattering due to the strong Coulomb interaction between the incident electrons and sample. The exceptions are 2D materials with negligible thicknesses and the development of precession electron diffraction (PED) which averages diffraction intensity with a rocking beam. The diffraction patterns we acquired and analyzed in this thesis mostly contain multiple scattering effects, which are better described by the dynamical diffraction theory.

There are three major approaches to the dynamical theory of high-energy transmission electron diffraction. The first approach, called the Bloch wave method, is based on the study of few-beam solutions in arbitrary orientations, following Bethe's original work [1]. This powerful method was first developed in Europe and Japan for the study of reflection electron diffraction, transmission diffraction from simple structures, Kikuchi lines, and high-order Laue zone (HOLZ) line analysis and phase measurement [2, 3]. It has been applied most successfully to small unit cell crystals. The second approach, called Howie-Whelan equations [4], was developed in the UK in the late 1950s for nanometer-resolution diffraction contrast imaging of crystals with defects, which we introduced in Section 1.2. It treats electron propagation in the nanometer-sized columns of crystal by considering scattering among a small number of diffracted beams under the so-called column approximation. This method approximates the atomic structure of defects by a thickness-dependent rigid and uniform displacement within the small column of crystal. The third approach, called the multislice method, was developed initially in Australia by Cowley and Moodie [5]. It has been shown to be highly efficient for numerical simulations of large unit cell crystals where hundreds of beams may be involved and can also be used for disordered materials or small nanostructures using a computational superlattice [5]. As a numerical method, it is less well suited for developing theoretical insights, but due to its flexibility it has produced the most widely used algorithm in electron microscopy for the interpretation of HREM images and STEM images. In this thesis, we used the Bloch wave method and the multislice method for numerical simulation of SEND patterns, which will be described in Section 2.4.

2.1.3. Different Types of Transmission Electron Diffraction

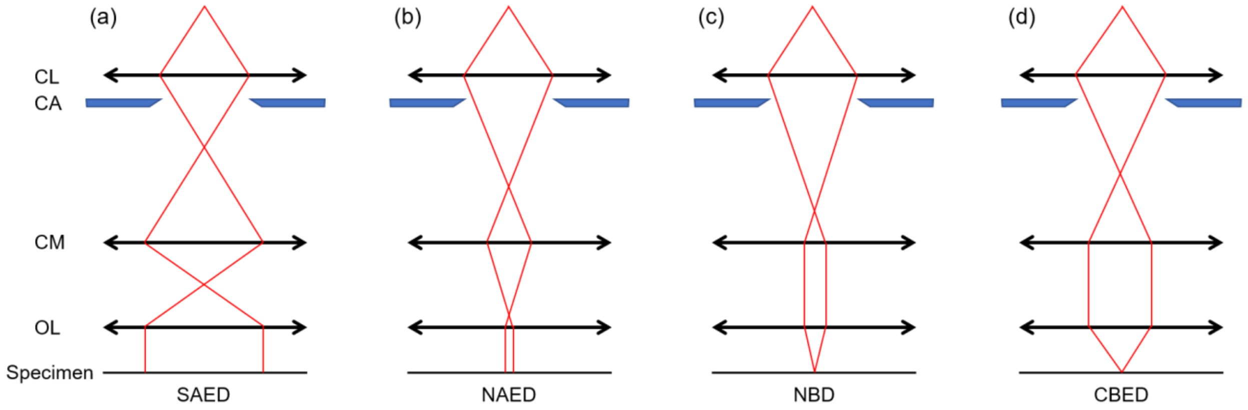

Fig. 2.2. Comparison between (a) SAED, (b) NAED, (c) NBD, and (d) CBED. CL: condenser lens; CA: condenser lens aperture; CM: condenser minilens; OL: objective prefield lens.

The types of electron diffraction patterns formed in a TEM are determined by the electron beam illumination, as depicted in Fig. 2.2.

Selected area electron diffraction (SAED) is the most popular diffraction technique in TEM. As shown in Fig. 2.2a, SAED is formed using the broad and parallel illumination, which is spread out over a large area of the specimen. The diffraction pattern is recorded by placing a selected area aperture at the image plane of the objective lens. The image plane is conjugate to the sample. Therefore, the recorded diffraction pattern comes from the specimen area defined by the image of the aperture at the sample plane. This technique is useful for getting diffraction information averaged over a large volume.

Nanoarea electron diffraction (NAED) is a direct improvement from SAED for small area analysis instead of averaging over a large area. As illustrated in Fig. 2.2b, NAED is formed by a nanometer-sized parallel beam with the help of a condenser minilens (CM) [6]. For a condenser aperture of 10 um in diameter, the probe diameter is about 50 nm with an overall magnification factor of 1/200 in the JEOL 2010 electron microscope (JEOL, USA). The beam size is much smaller than can be achieved by SAED. The major difference from SAED is that the diffraction volume is defined directly by the electron probe in NAED since all the electrons illuminating the sample are recorded in the diffraction pattern without the use of an aperture.

Nanobeam diffraction (NBD) is similar to NAED but using a slightly converging probe. The focused probe is achieved by weakening the condenser lens (CL) and placing the crossover at the front focal plane of the CM lens (Fig. 2.2c). The specimen is placed at the focal plane of the objective prefield lens (OL) where the probe is focused. When using a small condenser aperture with a small convergence angle, the beam is coherent, and the probe size becomes diffraction limited in a field-emission gun (FEG) TEM. The diffraction spots become small disks instead of sharp peaks.

Convergent-beam electron diffraction (CBED) is also recorded using a focused probe at the specimen. What is different from NBD is that the convergence angle is usually several times larger, achieved by changing the strength of CL and CM (Fig. 2.2d). In the conventional CBED mode, the incident plane-wave components are treated incoherently without interference between diffracted beams.

In this thesis, we use the name of electron nanodiffraction (END) to refer to both NBD and CBED, focusing on the fact that a nanometer-sized electron probe is placed on the specimen for diffraction.

2.2. Electron Probe Formation

2.2.1. Probe Size

The focused electron probe used in END helps to obtain diffraction information from a small volume of a sample. The spatial resolution of END largely depends on the probe size. When a LaB6 gun is used or the effective source angle after the condenser C1 lens is large, the electron lateral coherence length is much smaller than the diameter of the condenser aperture. In this case, the probe is considered as partially coherent or incoherent. The probe diameter d_0 at Gaussian focus is then given approximately by adding in quadrature the various probe broadening contributions. We have:

$$d_0^2 = d_s^2 + d_d^2 + d_{sa}^2 + d_c^2 + d_f^2, \tag{2.11}$$

where d_s is the geometrical source image diameter. d_d is the diffraction broadening equal to $0.6\lambda/\theta_c$ with θ_c being the beam convergence angle. d_{sa} is the contribution from lens aberrations (in a TEM without a probe corrector, it is equal to $0.5C_s\theta_c^3$ in the plane of least confusion, not the Gaussian image plane). d_c is the contribution from chromatic aberration, given by $\left(\frac{\Delta E_0}{E_0}\right)C_c\theta_c$, with ΔE_0 the energy spread in the electron beam. $d_f = 2\theta_c\Delta f$ is the contribution from a small focusing error Δf. For a typical modern TEM instrument with $C_s = 2$ mm at 100 kV, the contribution of diffraction d_d and spherical aberration d_{sa} are equal at an angle of about 7 mrad.

The smallest probe is obtained by minimizing all terms in Eq. (2.11). d_s can be made smaller than d_d and d_{sa} by combining a small physical source with a large demagnification. The illumination then becomes necessarily coherent, which is usually the case of using a FEG source. For a diffraction limited focused probe with a small convergence angle around 1 mrad, its intensity distribution is expressed by

$$I(r) \propto \left[\frac{J_1\left(\frac{2\pi r \sin\theta_C}{\lambda}\right)}{\frac{\pi r \sin\theta_C}{\lambda}}\right]^2, \tag{2.12}$$

where θ_c is the beam's half-convergence angle, and J_1 the first-order Bessel function. The first zeros of $J_1(x)$ occurs at $x = 3.832$, which gives the so-called Rayleigh criterion for resolution

$$r_0 = 0.61\frac{\lambda}{\theta}. \tag{2.13}$$

The intensity distribution in Eq. (2.12) can be fitted approximately by a Gaussian peak with a full width at half maximum (FWHM) of

$$d_{FWHM} = 0.52\frac{\lambda}{\theta}. \tag{2.14}$$

Fig. 2.3 shows a comparison between the theoretical FWHMs of different probes and experimentally measured ones using a Thermo Fisher Scientific Themis Z S/TEM with different beam convergence angles at 300 kV.

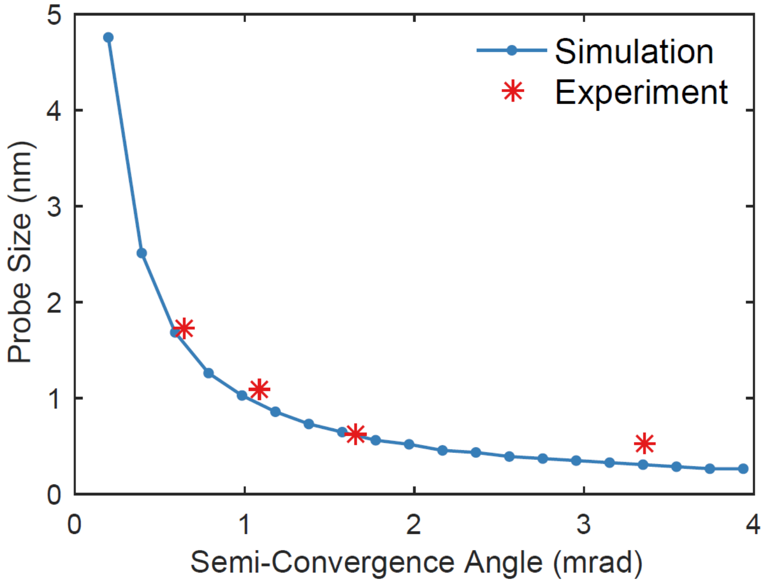

Fig. 2.3. Relation between the electron probe size and beam semi-convergence angle at 300 kV. The probe size is measured by the full width at half maximum (FWHM).

2.2.2. Beam Convergence

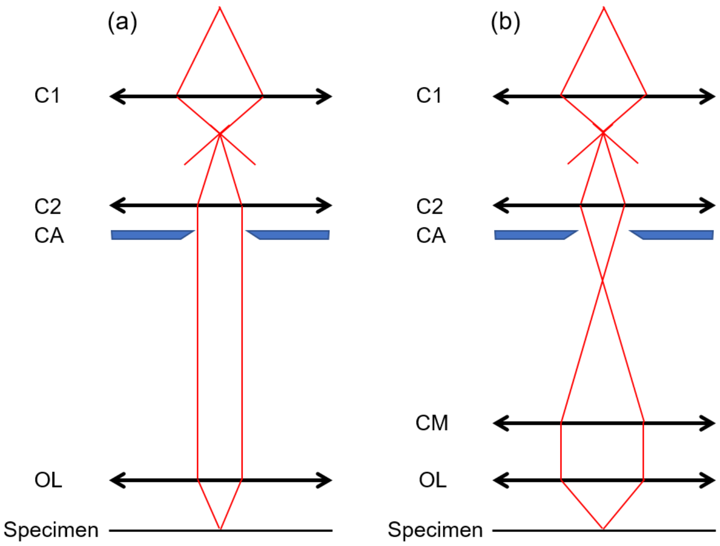

Fig. 2.4. Controlling convergence angle in a two-lens system. (a) Without the condenser minilens. (b) With the condenser minilens.

As shown in Eq. 2.14, for a diffraction limited probe, the size depends on beam convergence angle once the wavelength or accelerating voltage is fixed. In a TEM, the convergence angle can be controlled by the size of the condenser lens aperture or the strength of the condenser lenses. In a simple two condenser lens system, the specimen is placed at the focal plane of the objective prefield lens. The convergence angle in this case is determined by the beam size on the objective prefield lens, which is the same as the size of the condenser lens aperture (Fig. 2.4a). Since the number of different condenser lens aperture available is limited in a TEM, controlling convergence angle in a two-lens system is not very flexible. An improvement to this is by adding a condenser minilens (CM) immediately above the objective prefield lens. By varying the strength of C2 and CM lenses, convergence angle can be changed in addition to switching the condenser lens aperture (Fig. 2.4b). JEOL 2100 and JEOL 2200FS microscopes have NBD and CBD modes which provide a number of presets of strength of C2 and CM lens for different convergence angle. Thermo Fisher Scientific Themis Z S/TEM uses a three-condenser lens system with condenser minilens (Fig. 2.5). It allows users to continuously adjust convergence angle within a certain range by varying the strength of C2 and C3 lenses [7].

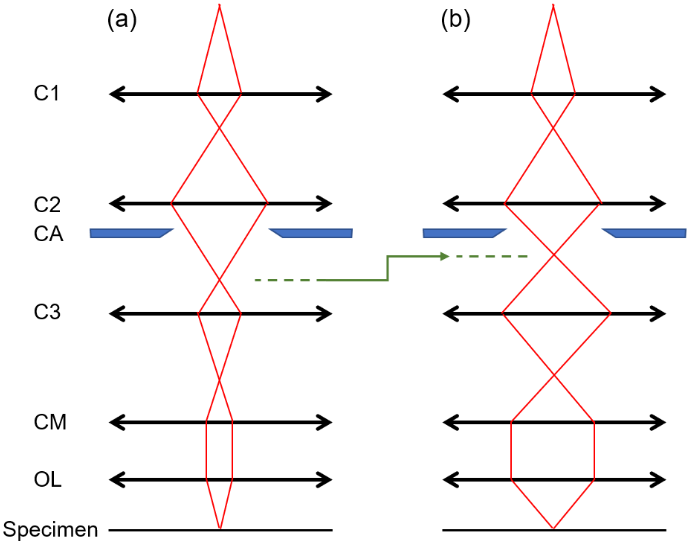

Fig. 2.5. Continuous changing of the beam convergence angle by varying the strength of C2 and C3 lenses in a three-condenser lens system. (a) Small convergence angle. (b) Large convergence angle.

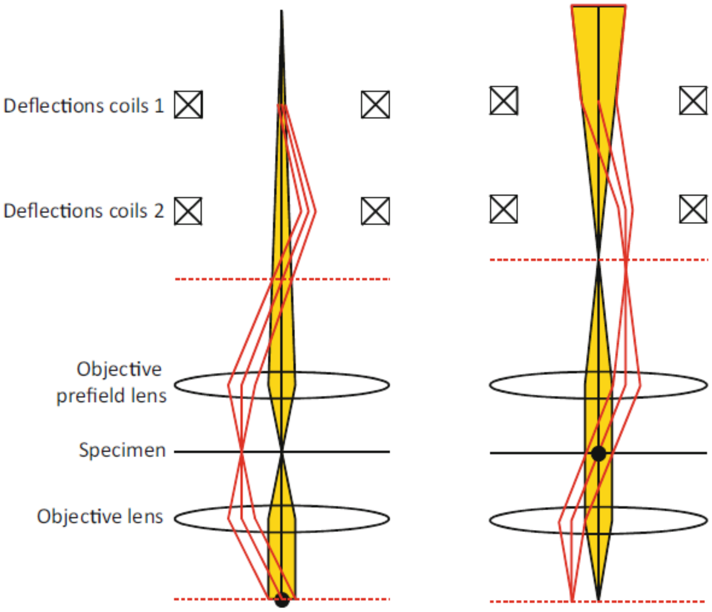

Fig. 2.6. Beam deflection coils used for beam shift (left) and beam tilt (right). The black disks mark the pivot point, and the red dash lines mark the front and back focal planes of objective prefield and objective lenses (from [8]).

2.2.3. Beam Scanning

Once a nanometer-sized electron probe is formed, we need to scan it across the sample to acquire a SEND dataset. A set of two deflectors (double deflection coils) are placed below the condenser lens and above the condenser minilens to deflect the beam. While the electron beam can be deflected by either electric or magnetic fields, magnetic coils are used in modern TEMs for beam deflection. When a pair of deflection coils are arranged perpendicular to each other, they apply uniform forces on the beam along horizontal directions. Together, they can be used to shift or tilt the beam along any direction in the x-y plane. As in Fig. 2.6, to shift a ray along the optical axis, it must be first deflected away from, and then toward the optical axis by the first and second deflectors successively. The beam must intersect the optical axis at the front focal plane of the lens above the specimen, which then brings it to the specimen running parallel to the optical axis. To shift the beam, we actually tilt the beam. To tilt the beam, it is first deflected away from the optical axis and then back toward the optical axis in such a way that all rays in the beam converge to the same point on the front focal plane as undeflected rays, but now shifted laterally.

The deflection coils can be configured in a number of ways for beam rocking for LACBED [9], conical scan as used in precession electron diffraction [10], and beam scan as used in SEND [11]. The beam scanning in SEND can be automated by a scan generator connected to the microscope for STEM imaging, or by an additional dedicated hardware attachment to synchronize the scan and diffraction pattern acquisition (NanoMegas, Belgium), or by using the computer control over the TEM scanning coils and image recording using the electron camera. An implementation of the latter approach was reported by Kim et al. [12]. The beam scanning and diffraction pattern acquisition are controlled using a custom script written in DigitalMicrograph (Gatan Inc, USA) by communicating with the host processor built into the TEM. This method was later improved by Shao et al. [13] to allow for beam scanning in the STEM mode as well. Ultimately, the acquisition speed of a SEND dataset is limited by the camera readout speed, the speed of beam deflection inside the TEM, communication between the computer and the TEM, and data writing speed of the memory. The recent progress in electron detectors has greatly improved the readout speed either using complementary metal-oxide-semiconductor (CMOS) sensors [14] or a hybrid pixel array detector (PAD) [15].

2.3. Microscope Setup for Scanning Electron Nanodiffraction

In a SEND experiment, the microscope must be aligned properly to obtain 4D-DDs from SEND without significant artifacts. Key aspects to be checked before a SEND acquisition include: (a) electron probe alignment, (b) beam tilt-shift purity, (c) diffraction pattern shift during beam scanning, (d) diffraction focus, and (e) sample height position. Spatial resolution of SEND is directly related to the size of the electron probe. To reach the theoretical diffraction limit (Section 2.2.1) as close as possible, column must be aligned so that the beam is focused at the back focal plane of the objective prefield lens. For SEND, beam tilt due to beam shift is undesired, which can introduce systematic error into orientation mapping, for example (discussed in Chapter 4). Also, beam tilt will cause diffraction pattern to shift on the detector. This can be corrected by the pivot-point alignment. Diffraction pattern shift on the detector during beam scanning can be minimized by proper intermediate lens alignment [12] or compensated by descan deflectors if available in the microscope. In the diffraction mode, the projection lens system projects the information on the back focal plane of the objective lens onto the detector. If the diffraction focus is off, Fresnel fringes will appear in the recorded diffraction disks, which is another artifact that can impact on quantitative analysis. Finally, the sample height must be adjusted to the back focal plane of the objective prefield lens where the electron probe is focused. Otherwise, shadow image will appear in diffraction disks, obscuring the feature of diffraction. In summary, the microscope alignment procedure for SEND is listed as follows:

1. Perform gun alignments (gun shift, gun tilt, monochromator) so that the beam is travelling along the optical axis with a desired beam current.
2. Switch the condenser aperture and adjust the strength of condenser lenses to have a desired beam convergence angle for the probe.
3. Fine tune the condenser aperture position, condenser lens astigmatism, beam shift, beam focus, pivot point alignment, and rotation center to make a smallest focused probe. Under coherent illumination, interference rings (ripples) around the probe can be seen, which is an indicator of good alignment.
4. Acquire an image of the probe using CCD and measure the FWHM of the probe. The number can be used to compare with theoretical diffraction limit to evaluate the alignment and as a reference for the spatial resolution.
5. During beam scanning, observe the diffraction pattern on CCD in live mode and align descan deflectors so that the diffraction pattern is not moving along with the scan. Use diffraction alignment to bring the center disk to the center of the CCD.
6. Adjust the projection lenses so that the diffraction disks are sharp without oscillations near the edges. This can be checked by imaging diffraction disks on a CCD.
7. Place the aligned probe on the sample. In image mode, adjust sample height until only a focused probe (with some modifications from the sample) is visible but not

diffracted beams. This can be hard when the sample is tilted to a high angle. Find a minimal spreading of the probe as possible in this case.

The procedure above ensures a proper alignment of the scanning probe used for SEND experiments. To complete the setup for SEND acquisition, one also needs to configure the scanning and the detector for diffraction pattern recording.

For a 2D scanning, the key parameters to determine are total scan size and step size. After calibration, these can be converted to the strength of deflector coils to shift electron beam by the control program. The step size defines the resolution of the 2D map of SEND, which is ultimately limited by the electron probe size. When the step size is smaller than the probe size, it is called oversampling. When the feature of interest is large, one can adjust the step size larger than the probe size, which is called undersampling. The total scan size and step size together determine the number of steps in total, which means how many diffraction patterns captured in the 4D-DDs. Adjust these parameters to balance the requirement of the experiment and total acquisition time and datafile size. For long acquisition, the sample is going to drift. It can be compensated by capturing an image of the sample every certain frames using an ADF detector (HAADF detector is usually preferred due to its larger inner radius to block less diffraction which should be captured on the camera underneath) to check how much drift is happening and apply beam shift to compensate it.

The parameters of a detector to consider include recording area, pixel binning, acquisition time, number of sub-frames per acquisition. Recording area and pixel binning will determine the size of each diffraction pattern, which can be adjusted to balance the experimental need and datafile size as well as camera readout speed. Full area with no binning will provide the best quality of diffraction patterns but may end up with unnecessarily large datafile and low framerate.

Acquisition time, along with the beam current, determines the total dose of electrons captured in a single diffraction pattern. Adjust accordingly to balance the signal-to-noise ratio (SNR) and beam damage to the sample. Number of sub-frames per acquisition (if available) allows one to achieve higher dynamic range as well as protect the detector from being damaged, which works by dividing a single acquisition into multiple sub-frames and adding them up together digitally afterwards.

2.4. Dynamical Diffraction Simulation

In this thesis, we focus on samples of 30 to 100 nm in thicknesses, where the dynamical diffraction effect is not negligible. To better understand our experimental data as well as to test our analysis methods, two types of dynamical diffraction simulation are used: the Bloch wave method and the multislice method.

The Bloch wave method is accurate for diffraction simulations on single crystals with small unit cells. When the length scale of sample variation is larger than our electron probe size (~1 nm), we can approximate the structure being illuminated as a single crystal. In this case, we use the Bloch wave method to simulate SEND patterns with different sample thickness, orientation, and beam convergence angle. The program we used is called Bloch written by Prof. Jian-Min Zuo in Fortran [3]. We add customized python script to automate the process of generating a large number of input files with different thickness and orientation and executing Bloch program. The simulated datasets are used for training and testing artificial neural networks (ANNs) described in Chapter 4.

The multislice method divides the sample potential into a sequence of thin slices so that each slice can be approximated as a weak phase object. In this way, diffraction from a thick sample even without periodicity can be simulated. This method is used when the length scale of sample variation is comparable to or smaller than our electron probe size. In Chapter 3, we use the multislice method to simulate SEND patterns from a fluctuating strain field with relaxation along the thickness direction. The program Zmult is written by Prof. Jian-Min Zuo in Fortran and C language [3]. To accelerate the speed, we reimplement the computation intensive fast Fourier transform part in Matlab using CUDA for parallel computing with a graphics processing unit (GPU).

2.5. References

[1] H. Bethe, Theory on the diffraction of electrons in crystals, Ann Phys-Berlin, 87 (1928) 55-129.

[2] C.J. Humphreys, Scattering of Fast Electrons by Crystals, Rep Prog Phys, 42 (1979) 1825-&.

[3] J.C.H. Spence, J.M. Zuo, Electron microdiffraction, Plenum Press, New York, 1992.

[4] A. Howie, M.J. Whelan, Diffraction Contrast of Electron Microscope Images of Crystal Lattice Defects .2. Development of a Dynamical Theory, Proc R Soc Lon Ser-A, 263 (1961) 217-+.

[5] J.M. Cowley, A.F. Moodie, The Scattering of Electrons by Atoms and Crystals .1. A New Theoretical Approach, Acta Crystallogr, 10 (1957) 609-619.

[6] J.M. Zuo, M. Gao, J. Tao, B.Q. Li, R. Twesten, I. Petrov, Coherent nano-area electron diffraction, Microsc Res Techniq, 64 (2004) 347-355.

[7] ThermoFisher, Titan - Condenser manual.

[8] J.M. Zuo, J.C.H. Spence, Advanced Transmission Electron Microscopy: Imaging and Diffraction in Nanoscience, in, Springer New York New York, NY, 2017.

[9] M. Tanaka, R. Saito, K. Ueno, Y. Harada, Large-Angle Convergent-Beam Electron-Diffraction, J Electron Microsc, 29 (1980) 408-412.

[10] R. Vincent, P.A. Midgley, Double Conical Beam-Rocking System for Measurement of Integrated Electron-Diffraction Intensities, Ultramicroscopy, 53 (1994) 271-282.

[11] J.-M. Zuo, J. Tao, Scanning electron nanodiffraction and diffraction imaging, in: Scanning Transmission Electron Microscopy, Springer, 2011, pp. 393-427.

[12] K.H. Kim, H. Xing, J.M. Zuo, P. Zhang, H.F. Wang, TEM based high resolution and low-dose scanning electron nanodiffraction technique for nanostructure imaging and analysis, Micron, 71 (2015) 39-45.

[13] Y.T. Shao, Determination of local crystal symmetry in complex, multielement, ferroelectric perovskites and alloys, PhD Thesis, (2018).

[14] G. McMullan, A.R. Faruqi, D. Clare, R. Henderson, Comparison of optimal performance at 300 keV of three direct electron detectors for use in low dose electron microscopy, Ultramicroscopy, 147 (2014) 156-163.

[15] M.W. Tate, P. Purohit, D. Chamberlain, K.X. Nguyen, R. Hovden, C.S. Chang, P. Deb, E. Turgut, J.T. Heron, D.G. Schlom, D.C. Ralph, G.D. Fuchs, K.S. Shanks, H.T. Philipp, D.A. Muller, S.M. Gruner, High Dynamic Range Pixel Array Detector for Scanning Transmission Electron Microscopy, Microsc Microanal, 22 (2016) 237-249.

CHAPTER 3

LATTICE STRAIN MAPPING USING CIRCULAR HOUGH TRANSFORM FOR DIFFRACTION DISK DETECTION

In this chapter, we develop a powerful and versatile technique for lattice strain mapping in nano-devices and nanomaterials using scanning electron nanodiffraction (SEND). The measurement of strain is based on determining the Bragg peak positions recorded in the diffraction patterns from a local crystal volume. However, the resolution and precision of SEND based strain measurement are fundamentally limited by the uncertainty principle and scattering that govern electron diffraction. Here, we propose a new method to measure lattice strain using a focused probe for high resolution and circular Hough transform to locate the position of non-uniform diffraction disks for high accuracy. Methods for fitting a 2D lattice to the detected disks for strain calculation are described, including error analysis. We demonstrate our technique on a FinFET device for strain mapping at the spatial resolution of 1 nm and strain precision of $\sim 3 \times 10^{-4}$. By testing on experimental and simulated four-dimensional diffraction datasets (4D-DD), the experimental parameters involved in data acquisition and analysis are thoroughly investigated to construct an optimum strain mapping strategy using SEND.

3.1. Introduction

Strain is an important structural property in materials science, as it impacts on many other physical properties. In semiconductor technologies, for example, strain is introduced to boost the performance of transistors by tuning the electronic band structure [1, 2]. In metals and ceramics, inhomogeneous strain is introduced by defects or doping, and strain characterization is therefore critical to understanding materials mechanical, electronic and chemical properties. In transmission electron microscopy, strain is also a major source of image contrast [3] that has attracted continuous research interest [4-8]. In X-ray and neutron diffraction [9], the average strain is measured by diffraction peak broadening [10], although the recent trend is toward strain mapping using scanning techniques [11]. Indirect measurement of strain can also be made using micro-Raman spectroscopy [12]. However, at the nm scale, transmission electron microscopy is the method of choice for high-resolution strain mapping.

Electron beam-based strain mapping can be performed in either imaging or diffraction mode. If the lattice fringes are resolved, strain can be calculated from electron images using the geometric phase analysis (GPA) method [4, 5]. At atomic resolution, strain can be measured using GPA [13], or by analyzing individual atomic positions using the methods such as template matching analysis (TeMa) [14] or peak fitting [15]. Diffraction-based techniques measure the lattice d-spacing in the reciprocal space using Bragg's law. Lattice parameters can be determined at high precision from high-order Laue-zone (HOLZ) lines in convergent beam electron diffraction (CBED) [16, 17]. In electron nanodiffraction (END) or nanobeam diffraction (NBD) using a parallel beam, lattice spacing is directly measured from the diffraction peak positions [18-23]. END describes all types of electron diffraction with a focused probe of nm size, which was first proposed by Cowley [24], while NBD is often associated with parallel beam diffraction [7]. The acronym SEND, adding the scanning aspect to END, was introduced in 2009 by Tao et al. [25], which was then further described in a book chapter in 2011 [26]. The END, NBD and SEND are versatile techniques as electron diffraction does not rely on high-resolution imaging and can work with both thin and thick samples. Also, the strain measurement using diffraction also does not require the exact zone axis condition, as long as multiple diffracted beams are visible. This helps in dealing with sample bending, which is an issue in the samples with a large strain field. The detection of multiple diffracted beams can be further helped with precession electron diffraction (PED) [27]. In addition, diffraction patterns from different materials can be separated in the reciprocal space, which makes the characterization of complex device structures possible. The field of view (FOV) in SEND or NBD is determined by the scanning step size and number of steps used during acquisition [21, 28].

The major challenge in the SEND or NBD based strain measurement comes from the uncertainty principle, as the spatial resolution (Δx) and the peak width (Δk) are coupled. In a SEND experiment on a thin sample, the spatial resolution is determined by the size of the focused electron probe, which is controlled by the beam convergence angle. In NBD, a near-parallel illumination is often selected to produce sharp, and well-defined, diffraction spots using probes of several nm in diameter [18, 19]. When the convergence angle is increased for higher spatial resolution, the diffraction peak is enlarged, which eventually becomes a disk as in CBED. The complicated contrast in a CBED disk due to diffraction presents a significant challenge to disk position detection, making strain measurement using CBED disks inaccurate [22]. To overcome this problem, Rouviere et al. [29] applied precession to the electron beam to reduce dynamic effects in the recorded diffraction patterns. Other efforts made to locate non-uniform diffraction disks include the radial gradient maximization method [20, 30], template matching using cross-correlation and its variations [21, 31]. These methods improve the measurement precision, but still suffer from the detection error due to issues such as half-moon-shaped disks and the difference between the intensity of different diffraction orders, which limits the measurement accuracy.

In this paper, we examine the entire procedure of strain mapping using SEND and propose a method for diffraction disk detection based on circular Hough transform (CHT). This method exploits the fact that although each diffraction disk has a different intensity distribution, their shapes are approximately similar, which is determined largely by the circular condenser aperture. The CHT can locate the center of a non-uniform diffraction disk even when a part of the disk edge is missing. Based on this, we develop a weighted 2D lattice fitting method to calculate the deformation matrix from the detected diffraction disk positions. The method is demonstrated through strain mapping on a 3D tri-gate FinFET device. An evaluation of the spatial resolution and strain accuracy and precision of our method is then presented based on the experimental result with the help of simulation, followed by suggestions on ways to achieve high resolution and high precision by optimizing the experimental parameters. In the end, we discuss and explain the effect of non-uniform strain field on the diffraction disk shape.

3.2. Methods

3.2.1. SEND data acquisition

In SEND, a focused electron probe is rastered across a sample region of interest (ROI). Diffraction patterns are recorded at each probe position using a pixelated two-dimensional (2D) detector. Thus, SEND collects a 4-D dataset, in the form of two spatial coordinates, the (x, y) in the real space and the (k_x, k_y) in the reciprocal space. SEND can be done in either the transmission electron microscopy (TEM) mode using the TEM deflection coils [25, 28], or in STEM mode [18-21]. When collecting the SEND data in a STEM, the HAADF detector can be used to record STEM images before, during, and after the acquisition to measure the sample drift and to apply drift correction accordingly. This is especially helpful when scanning a large area at a small step size as the entire acquisition could take hours to complete.

Data acquisition is automated using either a dedicated hardware to synchronize the scan and diffraction pattern recording or by using computer control of the TEM and the electron camera. An implementation of SEND using the second approach is reported by Kim et al. [28]. The speed of acquisition is largely limited by the camera readout speed. For high precision strain mapping, the quality of electron diffraction patterns is critical in terms of the signal-to-noise ratio, the size and the dynamic range of diffraction patterns. The impact of these factors on the measurement precision are discussed in Section 3.4.

To evaluate the proposed 2D strain mapping method, we acquired a SEND dataset, taken from a source/drain region of a fin field effect transistor (FinFET). The TEM sample was a cut-out by focused-ion beam (FIB) from a p-MOSFET device processed with Intel 14 nm technology. The sample is about 30 to 40 nm in thickness and oriented near the [1-10] zone axis. The SEND data was acquired using a Themis Z S/TEM (Thermo Scientific, Waltham, USA), installed at University of Illinois, which was operated in the μProbe STEM mode with the acceleration voltage of 300 kV. The electron probe was focused on the sample with a semi-convergence angle of 0.8 mrad, and the probe size of 1.0 nm in full width at half maximum (FWHM). Camera length was set at 360 mm where all 8 diffraction peaks adjacent to the center beam in the [1-10] zone axis were included in the recorded image. Diffraction patterns were taken using a CMOS camera (Ceta, Thermo Scientific) at the resolution of 1024×1024 pixels and 0.1 s exposure time per diffraction pattern. No pixel binning was applied. The scanning and diffraction data acquisition were automated by a function in the TEM control software provided by Thermo Scientific. During the scan, a new STEM image, containing the scanned region, was acquired by the HAADF (high-angle annular dark-field) detector every 60 frames for sample drift correction. Additionally, the sample was observed using ADF STEM images, which were acquired using the same electron probe and camera length setting as for SEND. The ADF detector collection angle is 16-96 mrad, and the recorded STEM images contain information from both Z-contrast and diffraction contrast.

3.2.2. Diffraction disk detection using circular Hough transform

After a SEND dataset is recorded, the first step is to reduce the 2D diffraction pattern into a list of diffracted beam positions. Several image processing techniques can be employed for this purpose based on the feature in the diffracted beam. In NBD using a parallel beam illumination, the diffracted beams are recorded as sharp diffraction spots. Locating the peak position, in this case, can be done by using a 2D peak searching and fitting algorithm. Under the convergent-beam condition in SEND, however, the diffracted beams become disks. In this case, the template matching method (TMM) using cross-correlation has been used to transform the disks into correlation peaks in the calculated correlation map [21]. Another method is to use edge detection and CHT to reduce diffraction disks into sharp spots [32]. In what follows, we describe the details of the CHT based diffraction disk detection technique.

3.2.2.1. Circular Hough transform

In the theory of high energy electron diffraction from a periodic crystal, the only similarity among the diffraction disks is the shape of the disk, resembling the approximate circular shape of the condenser aperture. Within the diffraction disks, varying rocking curve features are recorded, which depend sensitively on the crystal orientation and thickness, which presents a significant challenge for the accurate measurement of the diffracted disk position. To overcome this challenge, we propose an edge-based detection method to locate the diffraction disks. At the core of this method is CHT [33, 34]. As illustrated in Fig. 3.1a, all points on a circle, as specified by their coordinate (a, b), are transformed into circles in the so-called accumulator matrix of coordinates (x, y), satisfying the equation $(x-a)^2+(y-b)^2={r_o}^2$, where r_o is the radius of the circle. Here, each (a, b) point is the center of one circle. After accumulating all circles, the point where the circles intersect is exactly at the center (a_o, b_o) of the original circle, $(a-a_o)^2+(b-b_o)^2={r_o}^2$. In the pixelated accumulator matrix at the same resolution as the original image, each pixel counts the number of circles passing through it. When the exact value of the radius r_o is unknown, an estimated range of radius is used to generate the accumulator matrix. After CHT, the problem of disk detection is simplified to 2D peak finding in the accumulator matrix.

The procedure of detecting diffraction disks using CHT is summarized in Fig. 3.1b-e. First, a Sobel filter:

$$\begin{pmatrix} 1 & 0 & -1 \\ 2 & 0 & -2 \\ 1 & 0 & -1 \end{pmatrix}, \tag{3.1}$$

and its transpose are used to obtain the gradients in horizontal and vertical directions, $\partial\mathrm{X}$ and $\partial\mathrm{Y}$. Combined together, $\partial\mathrm{X}^2+\partial\mathrm{Y}^2$ is the filtered edge as shown in Fig. 3.1c. Next, the edge is transformed into an accumulator matrix using CHT. An estimated radii range of ± 5 pixels around the exact radius is applied to provide sufficient sampling to represent the transformed peak. The transformed peak is then projected both vertically and horizontally to allow for 1D peak fitting as described in Section 3.2.2.2. The fitted peak positions are taken as the coordinates of the diffraction disk center $\left(G_x, G_y\right)$.

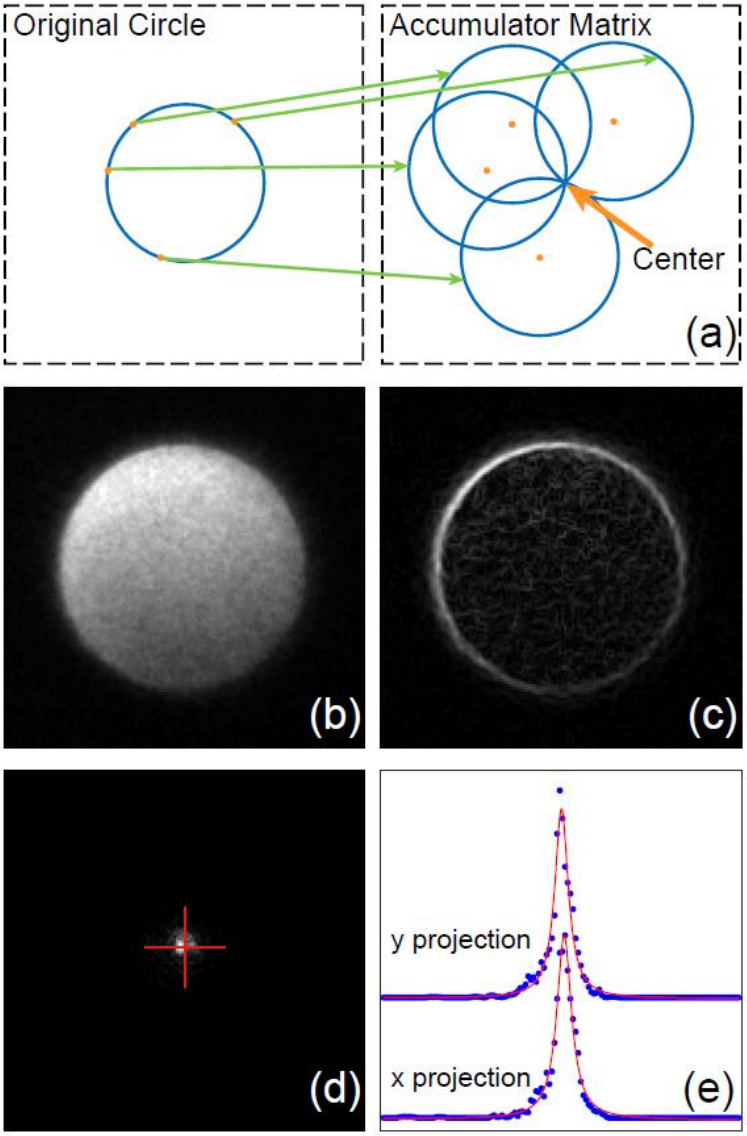

Fig. 3.1. Diffraction disk detection using CHT. (a) A schematic illustration of CHT, where points on the original circle are transformed into circles in the accumulator matrix, the center is defined by the intersection of the transformed circles. (b) An example of experimental diffraction disk is edge-filtered (c) and then transformed using CHT (d). (e) The disk center is determined by fitting the horizontal and vertical projections of the accumulator matrix using Lorentzian peak fitting. The center identified by this method is marked by a red crosshair in (d).

As shown in Fig. 3.1c, information inside the disk is mostly discarded by the Sobel filter. The CHT works well even when parts of the edge are missing. The detection is sensitive to the intensity of a few edge pixels. The width of the edge reflects the sharpness of the disks. This fact also makes the combined edge detection and CHT method sensitive to intensity noises. Section 3.4 gives a detailed discussion on this issue.

3.2.2.2. Peak fitting

To detect the position of a CHT peak, we use the peak fitting method. The peak finding method can also be applied directly to spot diffraction patterns. The method we describe here is based on 1D peak fitting to the projected peak intensity profiles (line profiles) in horizontal and vertical directions, respectively. First, a sub-image containing only the peak of interest is cropped out. The sub-image is then projected horizontally and vertically to produce two line-profiles. For the peak model, depending on the peak shape, we use the Lorentzian profile:

$$\boldsymbol{L}(x; x_0, \gamma) \equiv \frac{\gamma}{\pi((x-x_0)^2+\gamma^2)}, \tag{3.2}$$

where x_0 is peak position, and γ is half-width at half-maximum. The peak model is fitted to the line profiles to extract the horizontal and vertical positions of the diffraction peak $\left(G_x, G_y\right)$. Error analysis can be performed as part of the fitting.

3.2.3. Diffraction disk detection using template matching

The image processing technique described below based on template matching can be used to transform the disks into spots for peak fitting. This method, which was proposed before [31], will be compared with the CHT method in this paper.

Template matching works by comparing the targeted image I of size $k \times l$ with a template image T of size $m \times n$ $(m < k, n < l)$ to find the best match between T and a sub-image $I(r, s)$, where (r, s) is the position of the sub-image in I. The way to do so is by calculating correlation coefficient C_C between T and $I(r, s)$ for $r = 1,2, \dots, k - m + 1$ and $s = 1,2, \dots, l - n + 1$:

$$C_C(r, s) = \frac{\sum_{i,j}[I(r+i,s+j) - \bar{I}(r,s)][T(i,j) - \bar{T}]}{\sqrt{\sum_{i,j}[I(r+i,s+j) - \bar{I}(r,s)]^2}\sqrt{N\sigma_T^2}}, \tag{3.3}$$

where the summation runs over all $i = 1,2, \dots, m$ and $j = 1,2, \dots, n$. $\bar{I}(r, s)$ and $\bar{T}$ are average value of image $I(r, s)$ and T. $N = m \times n$ is the total number of pixels in T. σ_T^2 is the variance of T. In addition to Eq. 3.3, several other definitions of correlation exist [31]. Fig. 3.2 shows an example of template matching for an END pattern (Fig. 3.2a). A template (Fig. 3.2b inset) was obtained by cropping out a relatively uniform center disk. Using this template, the END pattern in Fig. 3.2a is transformed into correlation peaks, which can be measured using the peak fitting method from Section 3.2.2.2.

The TMM works best when the diffracted beams recorded in diffraction pattern are similar. The assumption that all disks are similar is approximately valid only in kinematical CBED (KCBED) [35]. The intensities within a given diffraction disk can also be made uniform by using PED [27]. To reduce the diffraction collection time, a setup of PED using a fast precession control unit is also required. For CBED patterns recorded without precession, the variations of rocking curve intensities are the major sources of error for strain analysis using template matching.

3.2.4. Determining the two-dimensional (2D) reciprocal lattice

In a diffraction pattern taken at or near a zone-axis, diffraction peaks lie on a 2D grid defined by the reciprocal basis vectors $\overrightarrow{g_1}$ and $\overrightarrow{g_2}$, and the center position $\vec{O}$ (Fig. 3.3).

The measured diffraction peak position gives $\overrightarrow{G_i}$. A fitting to the measured peak positions is carried out to determine $(\vec{O}, \overrightarrow{g_1}, \overrightarrow{g_2})$, where

$$\overrightarrow{G_i} = \overrightarrow{G_i^{fit}} + \vec{\epsilon}, \tag{3.4}$$

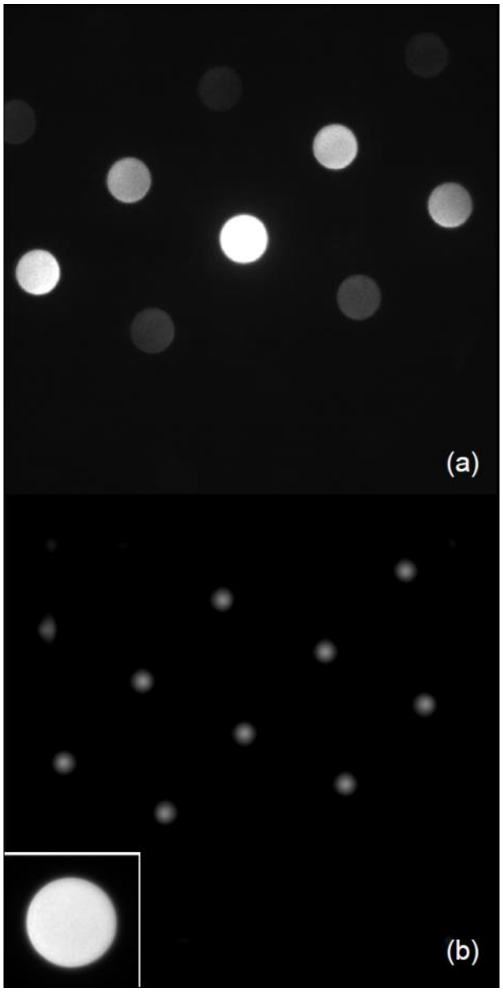

Fig. 3.2. Diffraction disk detection using template matching (TMM). (a) Example diffraction pattern. (b) Correlation map C_C calculated using the template image in inset.

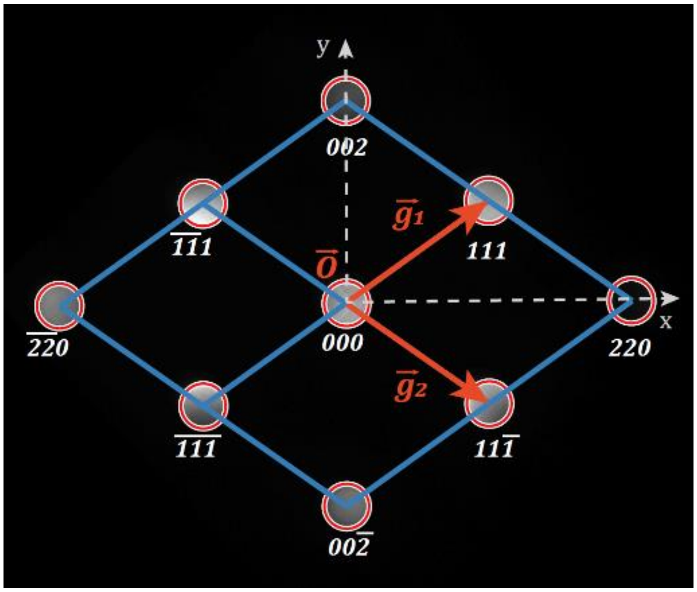

Fig. 3.3. Schematic of measuring the reciprocal basis vectors $\overrightarrow{g_1}$ and $\overrightarrow{g_2}$ from a diffraction pattern by fitting a 2D lattice to the position of the detected disks.

Here $\overrightarrow{G_i^{fit}} = \vec{O} + n_{i1} \cdot \overrightarrow{g_1} + n_{i2} \cdot \overrightarrow{g_2}$ (n_{i1} and n_{i2} are integers) and $\vec{\epsilon}$ represents error. The best fit is obtained when the distance between the measured and the fitted peak position is minimized with respect to the measurement error. To meet this requirement, we define a weighted residual sum of squares

$$\chi^2 = \sum_i \left(\frac{G_{ix} - G_{ix}^{fit}}{\sigma_{ix}}\right)^2 + \left(\frac{G_{iy} - G_{iy}^{fit}}{\sigma_{iy}}\right)^2, \tag{3.5}$$

where (G_{ix}, G_{iy}), $(G_{ix}^{fit}, G_{iy}^{fit})$ are the horizontal and vertical components of the measured and fitted positions of the peak, respectively. σ_{ix} and σ_{iy} are the standard deviation in the measured peak position, which are used as a weight to increase the contribution from those well-measured peaks. Calculation of σ_{ix} and σ_{iy} is detailed in next section. If σ_{ix} and σ_{iy} are both set to 1, no weight is applied, and Eq. 3.5 becomes the sum of squares of the distance between measured and fitted peak position. The summation runs over all detected peaks in the image. Written in the matrix form, we have

$$\chi^2 = (G_x - \mathbf{N_x}\beta_x)^{\mathrm{T}}(G_x - \mathbf{N_x}\beta_x) + \left(G_y - \mathbf{N_y}\beta_y\right)^{\mathrm{T}}\left(G_y - \mathbf{N_y}\beta_y\right), \tag{3.6}$$

where

$$G_x = \begin{pmatrix} \frac{G_{1x}}{\sigma_{1x}} \\ \frac{G_{2x}}{\sigma_{2x}} \\ \cdots \\ \frac{G_{ix}}{\sigma_{ix}} \end{pmatrix}, G_y = \begin{pmatrix} \frac{G_{1y}}{\sigma_{1y}} \\ \frac{G_{2y}}{\sigma_{2y}} \\ \cdots \\ \frac{G_{iy}}{\sigma_{iy}} \end{pmatrix}, \tag{3.7}$$

$$\mathbf{N}_{\boldsymbol{x}} = \begin{pmatrix} \frac{1}{\sigma_{1x}} & \frac{n_{11}}{\sigma_{1x}} & \frac{n_{12}}{\sigma_{1x}} \\ \frac{1}{\sigma_{2x}} & \frac{n_{21}}{\sigma_{2x}} & \frac{n_{22}}{\sigma_{2x}} \\ \cdots & \cdots & \cdots \\ \frac{1}{\sigma_{ix}} & \frac{n_{i1}}{\sigma_{ix}} & \frac{n_{i2}}{\sigma_{ix}} \end{pmatrix}, \mathbf{N}_{\boldsymbol{y}} = \begin{pmatrix} \frac{1}{\sigma_{1y}} & \frac{n_{11}}{\sigma_{1y}} & \frac{n_{12}}{\sigma_{1y}} \\ \frac{1}{\sigma_{2y}} & \frac{n_{21}}{\sigma_{2y}} & \frac{n_{22}}{\sigma_{2y}} \\ \cdots & \cdots & \cdots \\ \frac{1}{\sigma_{iy}} & \frac{n_{i1}}{\sigma_{iy}} & \frac{n_{i2}}{\sigma_{iy}} \end{pmatrix}, \tag{3.8}$$

$$\beta_x = \begin{pmatrix} O_x \\ g_{1x} \\ g_{2x} \end{pmatrix}, \ \beta_y = \begin{pmatrix} O_y \\ g_{1y} \\ g_{2y} \end{pmatrix}. \tag{3.9}$$

The minimum is achieved when $\frac{\partial\chi^2}{\partial\beta_x} = \frac{\partial\chi^2}{\partial\beta_y} = 0$, which gives

$$\begin{cases} \beta_x = (\mathbf{N_x^T N_x})^{-1}\mathbf{N}_{\mathrm{x}}^{\mathrm{T}} G_x \\ \beta_y = \left(\mathbf{N_y^T N_y}\right)^{-1}\mathbf{N_y^T} G_y \end{cases}. \tag{3.10}$$

The above solution is used to set up the reciprocal lattice matrix $\mathbf{G} = \begin{pmatrix} g_{1x} & g_{2x} \\ g_{1y} & g_{2y} \end{pmatrix}$.

3.2.5. Estimate of measurement precision

Error in the peak position can be estimated using the 0.95 confidence interval of the peak fitting:

$$C = b \pm \sigma = b \pm t\sqrt{S}, \tag{3.11}$$

where b is the fitted peak position, σ is the error in peak position. t is a constant dependent on the confidence level and the degree of freedom, which can be calculated from Student's t distribution. $t \approx 1.96$ when degree of freedom is large at 0.95 confidence level. S is the covariance matrix of the coefficient estimates:

$$S = (X^{\mathrm{T}}X)^{-1}s^2, \tag{3.12}$$

where X is the Jacobian of the fitted values with respect to the coefficients and s^2 the mean squared error.

According to Eq. 3.10, error in refined reciprocal lattice vectors can be calculated as

$$var(\beta_j) = \left(\mathbf{N_j^T N_j}\right)^{-1}\mathbf{N_j^T}var(G_j)\left(\left(\mathbf{N_j^T N_j}\right)^{-1}\mathbf{N_j^T}\right)^{\mathrm{T}}, \tag{3.13}$$

where $j = x, y$.

Error in g vector along any reciprocal direction $\vec{G}(= a\overrightarrow{g_1} + b\overrightarrow{g_2}, a, b \in \mathrm{R})$ is

$$var(G_j) = (0 \quad a \quad b)var(\beta_j)\begin{pmatrix}0\\a\\b\end{pmatrix}. \tag{3.14}$$

Finally, error in strain along $\vec{G}$ is

$$Error\big(strain(G)\big) = var\left(\frac{\frac{1}{G}-\frac{1}{G_{ref}}}{\frac{1}{G_{ref}}}\right)^{\frac{1}{2}} = \frac{G_{ref}}{G^2}var(G)^{\frac{1}{2}}. \tag{3.15}$$

3.2.6. Calculation of the strain tensor

Based on the reciprocal lattice matrix **G** and a reference matrix $\mathbf{G_0}$**,** the real space lattice matrix **A** and its reference $\mathbf{A_0}$, and local deformation matrix **D** in Lagrange convention can be calculated:

$$\mathbf{D} = \mathbf{A}\mathbf{A_0^{-1}} = (\mathbf{G}^{\mathrm{T}})^{-1}\mathbf{G_0^{\mathrm{T}}}. \tag{3.16}$$

For the general case without infinitesimal approximation, the deformation matrix $\mathbf{D} = \begin{pmatrix} d_{11} & d_{12} \\ d_{21} & d_{22} \end{pmatrix}$ can be separated into a rotation matrix **R** and a pure deformation matrix **F** through polar decomposition [5].

Following the derivations in Ref. [5], rotation angle $\theta = \arctan\left(\frac{d_{21}-d_{12}}{d_{22}+d_{11}}\right)$. Pure deformation is a symmetric matrix:

$$\mathbf{F} = \mathbf{R}^{-1}\mathbf{D} = \begin{pmatrix} \cos\,\theta & sin\theta \\ -sin\theta & \cos\,\theta \end{pmatrix}\mathbf{D}. \tag{3.17}$$

The local 2D strain tensor can be expressed as the difference between **F** and unit matrix:

$$\boldsymbol{\varepsilon} \equiv \begin{pmatrix} \varepsilon_{xx} & \varepsilon_{xy} \\ \varepsilon_{yx} & \varepsilon_{yy} \end{pmatrix} = \mathbf{F} - \mathbf{I}. \tag{3.18}$$

3.2.7. Diffraction pattern simulations

To help interpret our experimental results, we use the multislice method to simulate electron nanodiffraction using a modified version of the MULTIS program published in [36]. For the simulation, the electron probe is assumed to be fully coherent and is formed by Fourier transform of the aperture function without aberrations. A supercell of 40 nm by 40 nm in dimensions and 4096 by 4096 in sampling points is constructed to model the sample using the atomic scattering potential with the absorption due to the effect of phonon scattering included. The probe is then scanned across the supercell and its diffraction pattern is recorded at each probe position.

3.3. Application

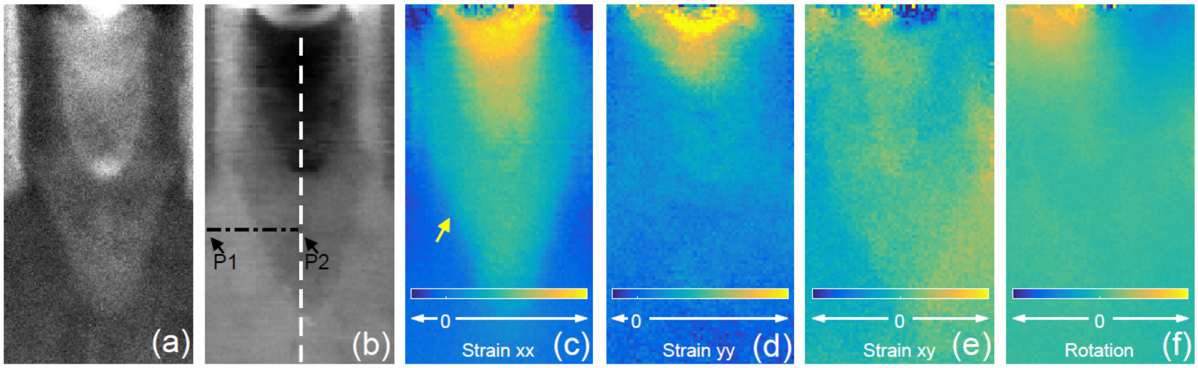

Fig. 3.4. Strain mapping of a Si-based FinFET device. (a) Medium-angle (16-96 mrad) annular dark-field image of the scanned region taken by an ADF detector with the same condition for strain mapping, which is used for drift correction during scanning. (b) Reconstructed virtual bright-field image of the scanned region shows that sample drift is well compensated. Maps of (c) ε_{xx}, (d) ε_{yy}, (e) ε_{xy}, and (f) rotation calculated from the scanning diffraction dataset at 1 nm spatial resolution. The image dimension is 60×120 nm^2. Vertical dashed lines in (b) and horizontal dash-dotted lines denote the position of strain profiles shown in Figs. 3.7a and 3.11a, respectively. The black arrows mark the probe position where diffraction disks in Fig. 3.11b and c are taken. The white arrows in (c-f) mark the increasing (pointing right) and decreasing (pointing left) strain and rotation. The maximum strain is smaller than the difference between the lattice constants of pure Si and Ge, which is 4%. The exact values are not shown in accordance with Intel's regulation.

Fig. 3.4 shows the results of 2D strain mapping on the source/drain area of a FinFET. The SEND map size is 60 by 120 pixels with the pixel (step) size of 1 nm. The designated scan area is shown in Fig. 3.4a, which is an ADF-STEM image taken at the beginning of the SEND experiment. Additional STEM images were also acquired during the SEND acquisition, which are used for drift correction based on the sharp features in the image for sample registration. Fig. 3.4b shows a virtual bright-field (VBF) image, reconstructed from the SEND dataset by integrating the intensity in the center disks. The good correspondence between the ADF-STEM image and the VBF image, apart from the inverse contrast, indicates that the sample drift during acquisition was well-compensated using our drift correction procedure.

Fig. 3.4c-f display the strain maps of longitudinal ε_{xx} and ε_{yy}, shear ε_{xy}, and rotation θ, which are obtained following the methods described in Section 3.2. The diffraction disk positions were detected using the CHT method and the CHT peak fitting by the Lorentzian profile. The 8 low-order diffracted beams and the center disk as shown in Fig. 3.3 were used to refine the reciprocal lattice matrix G, where the (111) disk was designated as $\overrightarrow{g_1}$ and the (11-1) disk as $\overrightarrow{g_2}$ (Fig. 3.3). The strain tensor was calculated based on the averaged reference matrix from a flat substrate region near the bottom of the scanned area.

The x direction in Fig. 3.4c-f is defined as the [110] direction of the reference lattice, and the y direction is [001]. Strain map ε_{xx} shows clearly the interface between SiGe and Si substrate, marked by yellow arrow in Fig. 3.4c, as can also be seen in ADF-STEM or VBF images, while it is not visible in ε_{xy}, reflecting the epitaxial nature of strain. The maximum of strain in both ε_{xx} and ε_{yy} is reached at the top of source/drain where it is attached to metal contact. The crystal shear and rotation are also most severe in this region. Another interesting feature in Fig. 3.4 is that the ε_{yy} map appears noisier than the ε_{xx} map, meaning that the precision in ε_{yy} measurement is lower.

This is correlated with the shorter length of (002) compared with that of (220). Assuming that the disk detection error is similar for the two cases, the strain error is larger where the length of g is shorter. Further discussion on the precision can be found in Section 3.4.4.

3.4. Discussions

3.4.1. Spatial resolution of SEND based strain mapping

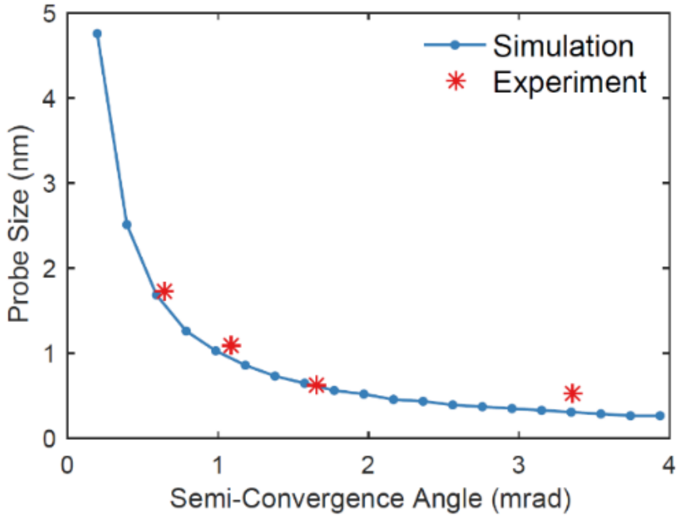

Fig. 3.5. Relation between the electron probe size and beam semi-convergence angle at 300kV. The probe size is measured by the full width at half maximum (FWHM).

The spatial resolution of strain mapping using SEND can be taken approximately as the electron probe size or the column diameter $\sqrt{\lambda t}$, whichever is larger [28]. The electron probe is diffraction limited according to Rayleigh criterion $r = 0.61\frac{\lambda}{\theta}$, for a small convergence angle. For a given acceleration voltage, the electron probe size decreases as the convergence angle increases, which then stabilizes because of aberrations, as can be seen in Fig. 3.5. In high-resolution STEM, the beam convergence angle is much larger at ~10 to 30 mrad. The large convergence angle is used to form Å or sub-Å sized electron probes. For strain analysis using SEND, however, the convergence angle is kept small so that neighboring diffraction disks do not overlap, as the overlapping disks make disk detection imprecise. At the limit where the disks touch each other, the probe size is about the size of d-spacing, which is the limit for strain mapping since strain is defined at the lattice level in most applications. The measurement precision improves as the volume of crystal for diffraction increases. Because of this, a nm-sized electron probe is preferred over the smaller, sub-nm sized, probes. The same correlation between the spatial resolution and the precision of strain measurement is also found in the real-space based strain mapping techniques [14].

3.4.2. Impact of sample orientation and thickness on the strain measurement accuracy

Real samples are often bent and have varying thicknesses, the error caused by change in the diffraction condition is systematic that limits the strain measurement accuracy. Here, we examine the strain measurement accuracy as impacted by variations in the sample orientation and thickness with the help of simulation. We compare the intensity-based method (TMM) with the edge-based method (CHT) based on the simulated SEND patterns.

The model we used to test the methods is a perfect Si crystal oriented along the [1-10] zone-axis. Electron diffraction was simulated using the multislice method as described in Section 3.2.7. The first set of simulations tilted the beam around the zone axis from 0.1° to 0.4° along the x || [110] and y || [001] directions for a sample of 8 nm in thickness. Since there is no strain built in the model and the distances between the diffraction disks in the simulated diffraction patterns are determined by the reciprocal lattice vectors, any measured strain (change in the measured d-spacing) can be attributed to the error of the diffraction disk detection method due to change in diffraction intensity, which we simply refer as strain error. Fig. 3.6a and b display the strain error from the simulated diffraction patterns using the CHT and TMM, respectively. Comparison between these two figures shows that while the strain error in TMM is strongly correlated with the beam tilt, the error in the CHT method is much less.

We then repeated the simulation with the sample thickness by varying the simulation thickness from 8 nm to 80 nm. Fig. 3.6c plots the strain error from these simulations. Each data point in the plot is an average of 25 strain values measured from 25 simulated patterns of different beam tilt following the same routine in Fig. 3.6a and b.

The above results show that the edge-based detection method tends to have a higher accuracy than the intensity-based method when it comes to detecting non-uniform diffraction disks. The CHT method is relatively insensitive to the intensity changes due to sample bending and variations in sample thickness. Especially when the sample is thick and the intensity pattern is complicated, the strain error using CHT is kept below 0.05%, which is far better than the performance of TMM.

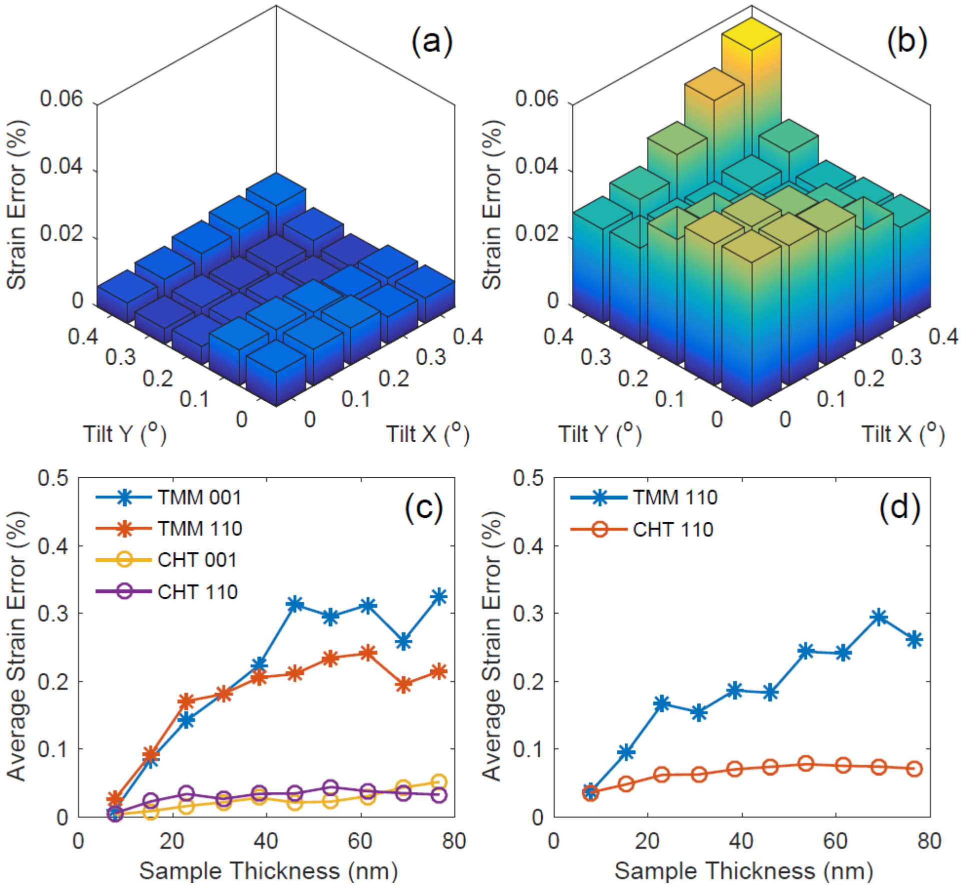

Fig. 3.6. Comparison between accuracy of template matching (TMM) method and circular Hough transform (CHT) method based on multislice simulation of unstrained/strained Si model structure. Error in strain along [110] direction of using the (a) CHT or (b) TMM method to detect diffraction disks from a sample of 8 nm thick. Different intensity distribution in the disks is achieved by tilting electron beam around x ∥ [110] direction and y ∥ [001] direction. (c) Comparison of strain measurement error on single crystal sample between two methods along 110 and 001 directions at various sample thickness. Each data point is an average of a tilt series of 25 patterns. (d) Comparison of strain measurement error on sample strained along [110] direction. Each data point is an average of 10 different probe positions and 25 beam-tilt combinations, totaling 250 patterns.

3.4.3. Strain measurement accuracy of a sinusoidal strain field

Next, we test our methods using an artificial strain model by displacing atoms from their original positions in the model Si structure along the [110] direction. The strain field we introduced is sinusoidal with the amplitude of displacement at 1% over the period of 80 unit cells. The electron probe was scanned over the area where the strain changes from -1% to 1%. Overall, 10 different strain values and different local strain gradients are sampled here. At each probe position, 25 beam tilts as in the unstrained case of previous section were simulated. The strain error was averaged over 250 simulated patterns. The results are plotted vs sample thickness in Fig. 3.6d. The error using the CHT method is less than 0.1% for sample thicknesses up to 80 nm. The difference between Fig. 3.6d and c is attributed to the effect of local strain variation on electron diffraction. The volume illuminated by the electron beam is no longer a perfect lattice here. Thus, the diffraction patterns of different beam tilt come from differently strained regions, and the variations in the sample orientation and thickness cause fluctuations in the measured strain, which reduces the accuracy of the CHT method. Deviation due to a finite-sized probe will be further discussed in Section 3.4.6.

3.4.4. Strain measurement precision

In this section, we evaluate the precision of strain measurement using two different methods. One is by performing a calibration experiment on an unstrained crystal. The other is through error analysis based on the fitting error of diffraction disks as described in Section 3.2.5. The error analysis method can be applied directly to the experimental dataset. Both methods provide an assessment of the measurement precision or sensitivity. As electron diffraction from a strained crystal is different from that of an unstrained crystal, the measurement precision is also sample dependent. In applications, the 3D nature of sample strain is often unknown. Because of this, we prefer to discuss the measurement precision rather than the measurement accuracy, which is discussed in the previous section for a known strain model.

The calibration experiment was carried out on a flat region of Si substrate in the FinFET device measured in Section 3.3, using the same experimental condition as in Fig. 3.4. The scanned area was selected to be close to the strained source/drain region in Fig. 3.4 so the sample thicknesses in the two measurements are similar (~40 nm). The scan size is 10 by 10 pixels with a step size of 1 nm. The measured strain value is plotted in Fig. 3.7 along with the strain profiles extracted from the 2D strain maps in Fig. 3.4. The standard deviation obtained from the calibration scan can be taken as the strain measurement precision, which is 0.036% along the [110] direction and 0.076% along the [001] direction, respectively. The difference in the strain measurement precision along two different directions explains that the difference in smoothness seen in Fig. 3.4c and d, where Fig. 3.4c appears smoother than Fig. 3.4d. The smoothness reflects the measurement precision.

The calibration experiment was performed on a single crystal region. Thus, it does not capture the diffraction features from a strain field. Because of this, it tends to underestimate the error in real experiments on a strained lattice.

The strain measurement precision can be estimated directly from the acquired SEND data via an error analysis based on the fitting error of each diffraction peak. From the description in Section 3.2, in both TMM and CHT, the peak position is determined by peak fitting.

We calculated the error maps for the strain maps ε_{xx} and ε_{yy} using the method described in Section 3.2.5, the results are shown in Fig. 3.8. From the error maps, we can see that strain precision is lower at the interfaces, especially near the bright edge at the top of both maps where the crystalline structure meets the amorphous film. The average error excluding the interfacial region at the top is 0.029% and 0.075% along the [110] and [001] directions, respectively. This agrees with the trend that the strain along [110] can be measured at a higher precision than along [001] as observed in the Si substrate calibration experiment.

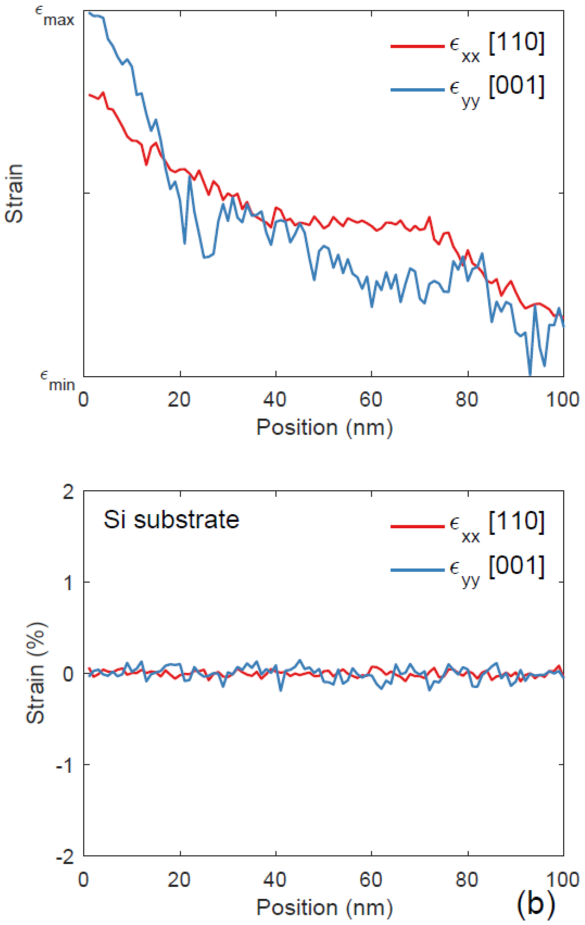

Fig. 3.7. Example strain profiles from strained and unstrained regions of a FinFET transistor. (a) Profiles of strain ε_{xx} along [110] and ε_{yy} along [001] extracted from the strain maps in Fig. 3.4c and d. (b) Profiles of ε_{xx} and ε_{yy} measured from a relatively uniform substrate region for calibration.

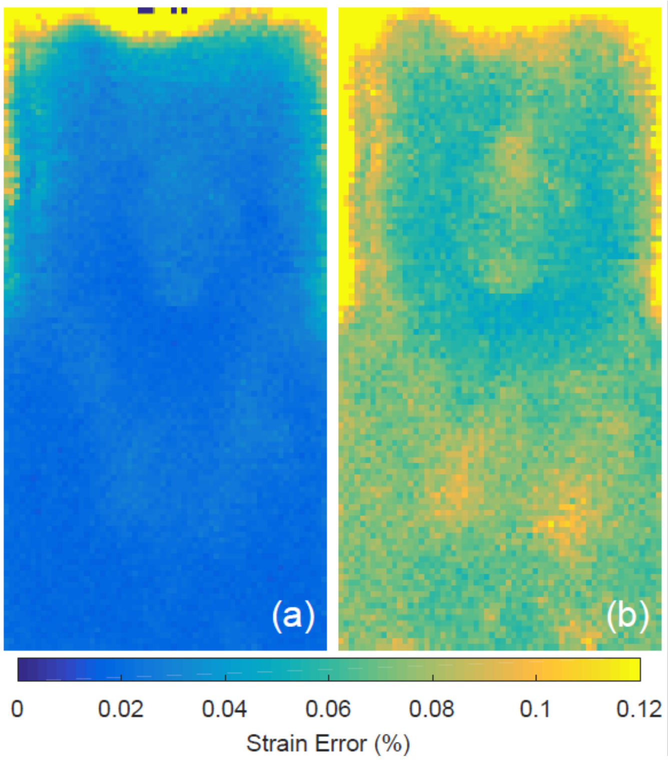

Fig. 3.8. The calculated error maps for strain (a) ε_{xx} and (b) ε_{yy} on the FinFET device.

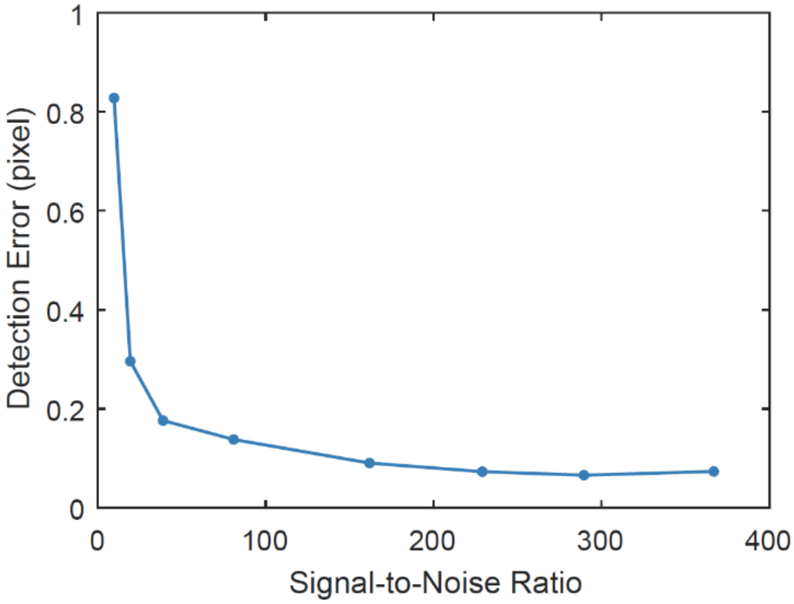

Fig. 3.9. Diffraction disk detection error using CHT at different signal-to-noise ratios.

3.4.5. Optimize the experimental conditions for higher precision

The strain measurement precision is determined by the precision of disk detection, which can be improved by optimizing the experimental conditions, including the diffraction intensity level and noise, the diffraction camera length and the beam convergence angle.

The diffraction intensity level and noise in an acquired diffraction pattern is measured by the signal-to-noise ratio (SNR), which is a critical parameter. Here we define the SNR of a diffraction disk as

$$SNR = \frac{\overline{I_{disk}}}{\sigma_{noise}}, \tag{3.19}$$

where $\overline{I_{disk}}$ is the average intensity in a diffraction disk, and σ_{noise} is the standard deviation of the background intensity.

To examine the effect of SNR on disk detection, we performed a calibration experiment in vacuum (without sample) using the same electron probe for the strain measurement described in Section 3.2. The experiment was done without scanning to avoid the scan noise. The SNR was controlled by changing the electron beam intensity using mono-focus in the Themis Z STEM. At each SNR level, 100 diffraction patterns were acquired. The recorded diffraction patterns contain a single flat disk that differ in intensity and in noise (including the electron beam noise due to the instrument and environmental instabilities). The error in the detected disk position is calculated from the standard deviation of the measured disk positions in the acquired patterns. The result of using CHT to detect the disk is shown in Fig. 3.9. The detection error is inversely proportional to SNR. The proportionality can be attributed to the effect of noise on the disk edges, which become less defined as noise increases, leading to larger errors in disk detection. The error decreases as the

SNR increases, and the improvement slows down when $SNR > 100$, which can be taken as a cutoff for acquiring a good diffraction dataset for the strain measurement using CHT.

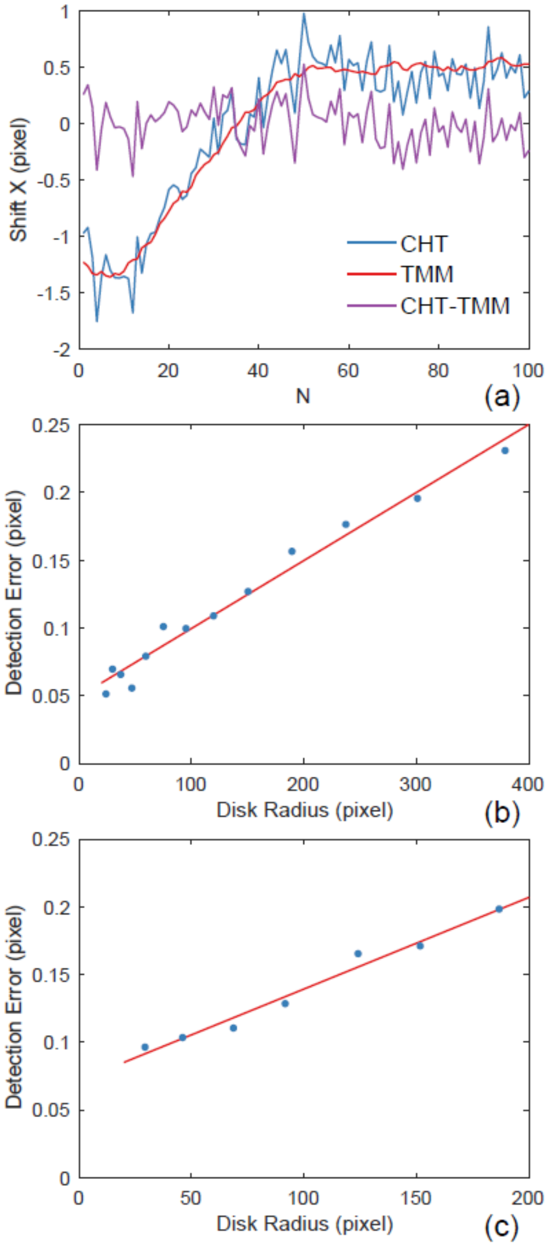

Fig. 3.10. Diffraction disk detection error using CHT for different disk radius. (a) An example of the measured disk position x from 100 patterns recorded over vacuum using CHT and TMM and their difference. Error in diffraction disk detection using CHT for different disk size achieved by changing (b) the camera length and (c) the convergence angle.

Another deciding factor for disk detection is the disk size, which is determined by the camera length as well as the convergence angle. Fig. 3.10b and c show the relation between the disk detection error and the disk radius. Following the same procedure as in Fig. 3.9, the plotted detection error here was calculated from the standard deviation of the detected disk position from 100 exposures in vacuum using the CHT method, while the SNR was kept same for all disk radii. The fluctuation in the detected disk position came from the error of the CHT method and the electron beam deflection due to instrument and environmental instabilities. To separate these two effects, we also applied TMM to detect the position of the uniform diffraction disk. Because the disk is uniform in intensity for all patterns, TMM does not suffer from the issues as discussed in Section 3.4.2, and thus, it is can be used to detect the disk position accurately in this case. TMM is used as the reference for examining the error of CHT, as shown in Fig. 3.10a.

At a fixed beam convergence angle of 0.8 mrad with the SNR kept at 280, the disk radius is proportional to camera length. The detection error σ plotted as function of the camera length L in Fig. 3.10b can be approximately fitted with $\sigma = \sigma_o + s \cdot L$, where σ_o and s are the intercept and slope of the linear fit. The strain measurement precision Δg is then given by $\Delta g = \sigma/L = s + \sigma_o/L$ for $L < L_{max}$. The upper limit L_{max} is determined by the detector size, which has to record enough diffraction disks in order to measure the reciprocal lattice. The precision improves as L increases. This improvement was confirmed by a calibration experiment performed on the unstrained region of our FinFET sample similar to the one in Section 3.4.4 using a CCD of 2048 by 2048 pixels with the camera length increased to the maximum allowed for keeping all nine disks for strain calculation (see Fig. 3.3). The strain precision estimated by the standard deviation is 0.030% along [110] direction and 0.031% along [001] direction, compared with the 0.036%

along [110] direction and 0.076% along [001] direction reported in Section 3.4.4 using a detector of 1024 by 1024 pixels.

At a fixed camera length, the diffraction disk radius increases as the beam convergence angle increases. Fig. 3.10c shows the increase in the CHT detection error as the convergence angle of the electron probe increases. Both camera length and SNR were kept constant at 360 mm and 150 in this case. Under these conditions, at the radius of 90 pixels, the beam semi-convergence angle is 1.6 mrad. Thus, the strain measurement precision decreases as the convergence angle increases using CHT, and the probe size and strain precision are competing factors. In other words, the convergence angle should be chosen as small as needed for the required spatial resolution. The minimum number of circular points for CHT is ~10.

3.4.6. Strain effect on the diffraction disk shape

Fig. 3.11 examines the effect of strain on the diffraction disk edge intensity. The change in the edge intensity is observed for the diffraction patterns taken at the positions P1 and P2 in Fig. 3.4b, in the form of bright and dark rings at one side of the diffracted disk. To understand the origin of this effect, we simulated electron nanodiffraction from a Si crystal model with a sinusoidal strain field along [110] direction. The model strain profile is plotted in Fig. 3.11d, which was designed to replicate the experimental strain distribution (Fig. 3.11a) along the dash-dotted line connecting P1 and P2 in Fig. 3.4b. Diffraction patterns simulated from P3 to P4 in the model using the same convergence angle as in experiment show similar ring effect at the edge of diffraction disks, as can be seen in the simulated (-2-20) disk at the P3 and P4 probe positions (Fig. 3.11e and f).

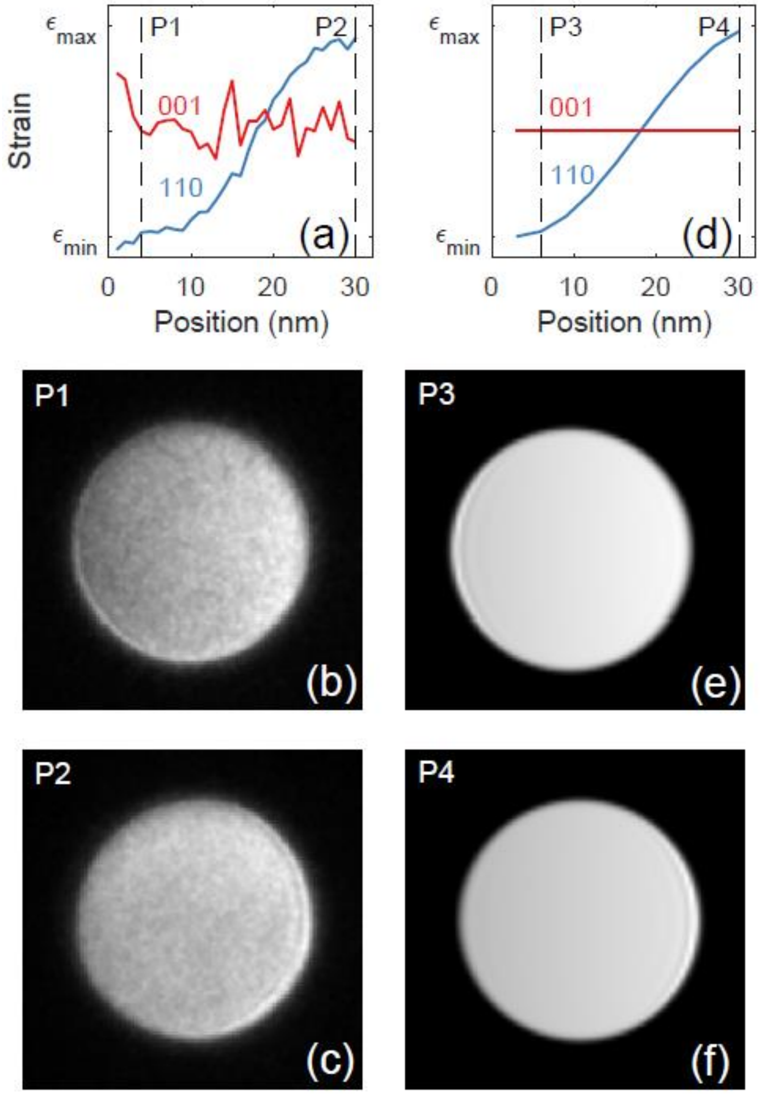

Fig. 3.11. Interference effect on the diffraction disk shape without an abrupt interface. (a) Experimental strain profiles extracted from Fig. 3.4c and d along the dash-dotted line in Fig. 3.4b. The (-2-20) diffraction disk taken at the probe position of (b) P1 and (c) P2. (d) Strain profiles of a strained Si model for simulation with $\epsilon_{max} - \epsilon_{min} = 1\%$. The simulated (-2-20) diffraction disk at the probe position of (e) P3 and (f) P4 using the multislice method, showing the same feature as in (b) and (c). The center disk of the diffraction pattern is on the right side to the displayed disks.

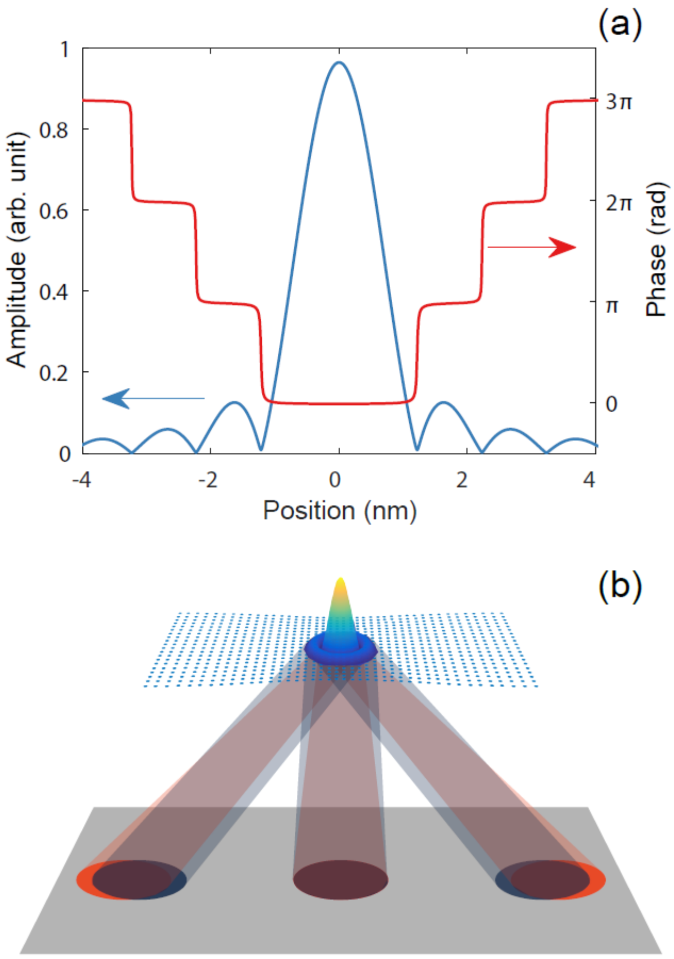

Fig. 3.12. Mechanism of interference effect in diffraction disks. (a) The distribution of amplitude and phase in the electron probe used for multislice simulation in Fig. 3.11. (b) Schematic diagram of convergent beam diffraction at a local strain minimum.

Next, we consider the complex wave function of the electron probe. Fig. 3.12a shows the line profiles for the amplitude and phase of the complex wave function across the probe center. The amplitude profile shows the characteristic primary peak at the center and the much smaller secondary peaks on both sides, while the phase increases by π for each secondary peak. Because of the change in phase, contributions from the secondary peaks cancel each other to a good approximation when the sample illuminated by the primary and secondary peaks are the same.

For a probe illuminated over a strained structure with a large strain gradient, the structures beneath the primary and secondary peaks have different lattice constants. As a first-order approximation, we only consider the largest secondary peak in the electron probe, which is in antiphase with the primary peak (Fig. 3.12a), while ignoring the effects of other secondary peaks. The ring effect is explained schematically in Fig. 3.12b. The ray paths of the direct and diffracted beams from the primary and secondary peaks are illustrated in colors (orange and blue). The average lattice constants differ at the sample regions illuminated by the primary and the secondary peak. The destructive interference between the two paths at the overlapping areas lowers the intensity in the diffracted beams and results in a bright edge where the interference is absent. The brighter edge, which is only obvious on one side of the disk (Fig. 3.11), is due to the fact that the diffraction of the primary peak contributes more in intensity than the secondary peak. Therefore, the position of the bright edge provides information about the local strain environment. In Fig. 3.11b and e, the bright edge is away from the central beam, and the probe is at a strain minimum. On the other hand, in Fig. 3.11c and f, the bright edge is close to the center beam, as the probe is at a strain maximum. The change in edge intensity impacts the strain measurement accuracy dependent on the detection method, and the impact in the case of CHT is small from the same benefit of edge detection as discussed before.

Next, we consider electron nanodiffraction at an abrupt interface of two different crystal lattices. For this purpose, we built a Si crystal model of 8 nm in thickness with half of the structure unstrained, while the other half has a 3% tensile strain. The elastic relaxation is applied to mimic the real thin-film sample [37]. The cross-section of the model is illustrated in Fig. 3.13a with the exaggerated lattice distortion. Electron nanodiffraction was simulated at the same conditions as the previous case of continuous strain. The (-2-20) diffraction disks from unstrained region, interfacial region, and 3% strained region are shown in Fig. 3.13b, c, and d, respectively. Severe disk distortion is observed at the interface (Fig. 3.13c). The oval distortion is due to the overlapping of two disks originated from differently strained regions, which is similar to the selected area electron diffraction over a region with two different lattice spacings. This effect was also observed previously by Mahr et al. [30]. The elastic relaxation used in our simulation makes the strain variation relatively smooth near the interface, which leads to bright edges and dark rings similar to Fig. 3.11 as well. The CHT measures the center of the oval disk and thus the average d-spacing under the electron probe. By detecting the weak, secondary edges, it is possible to separate the lattices on the two sides of the interface [30].

3.5. Conclusions

We have developed a strategy for high resolution strain mapping based on SEND. The key to achieve high measurement precision in strained samples, while pushing for high spatial resolution using a convergent beam, is to develop an intensity insensitive method for diffraction disk detection. A method using circular Hough transform to detect the diffraction disks is described here. A weighted 2D lattice fitting is designed to calculate the deformation matrix and strain, from the detected disk positions. The method is applied to measure strain in a FinFET device at the spatial resolution of 1 nm. The effect of sample orientation, thickness, and strain field distribution on the strain measurement accuracy are examined based on the multislice simulations. The strain measurement precision is estimated by a calibration experiment on an unstrained region of the sample, as well as analytically from the diffraction patterns directly. Different experimental conditions are explored to provide a guideline for the optimal strain measurement strategy: signal-to-noise ratio of the diffraction pattern should be larger than 100 and camera length should be as large as there are enough diffraction disks to calculate the deformation matrix. Finally, we pointed out the difference in diffraction from the uniformly strained and non-uniformly strained regions. Together, our results show that SEND is a powerful technique to measure strain from crystalline materials at nanoscale, but the proper analysis is critical to achieve both high spatial resolution and high strain measurement precision.

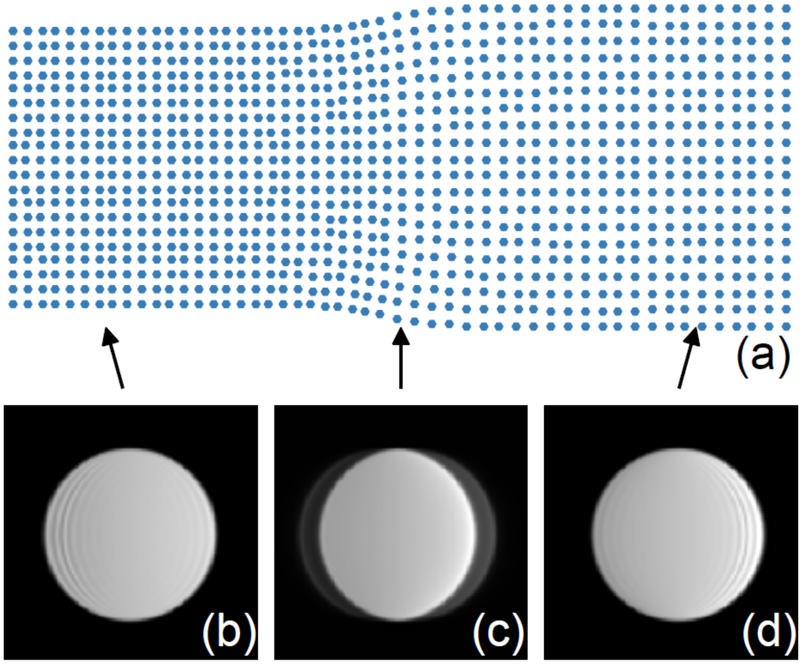

Fig. 3.13. Interference effect on the diffraction disk shape with an abrupt strained interface. (a) The cross-section of the strained silicon model used for simulation, where the lattice constants differ by 3% for the left and right side of the model. The strained lattice is allowed to relax and the resulted lattice distortion is exaggerated in the figure for a better view. (b-d) The simulated (-2-20) diffraction disks at small lattice spacing region, interface, and large lattice spacing region, respectively. The center disk of the diffraction pattern is on the right side to the displayed disks.

3.6. References

[1] T. Ghani, M. Armstrong, C. Auth, M. Bost, P. Charvat, G. Glass, T. Hoffmann, K. Johnson, C. Kenyon, J. Klaus, B. McIntyre, K. Mistry, A. Murthy, J. Sandford, M. Silberstein, S. Sivakumar, P. Smith, K. Zawadzki, S. Thompson, M. Bohr, A 90nm high volume manufacturing logic technology featuring novel 45nm gate length strained silicon CMOS transistors, 2003 Ieee International Electron Devices Meeting, Technical Digest, (2003) 978-980.

[2] S.E. Thompson, M. Armstrong, C. Auth, M. Alavi, M. Buehler, R. Chau, S. Cea, T. Ghani, G. Glass, T. Hoffman, C.H. Jan, C. Kenyon, J. Klaus, K. Kuhn, Z.Y. Ma, B. Mcintyre, K. Mistry, A. Murthy, B. Obradovic, R. Nagisetty, P. Nguyen, S. Sivakumar, R. Shaheed, L. Shiften, B. Tufts, S. Tyagi, M. Bohr, Y. El-Mansy, A 90-nm logic technology featuring strained-silicon, Ieee T Electron Dev, 51 (2004) 1790-1797.

[3] P.B. Hirsch, Electron microscopy of thin crystals, R. E. Krieger Pub. Co., Huntington, N.Y., 1977.

[4] M.J. Hytch, E. Snoeck, R. Kilaas, Quantitative measurement of displacement and strain fields from HREM micrographs, Ultramicroscopy, 74 (1998) 131-146.

[5] J.L. Rouviere, E. Sarigiannidou, Theoretical discussions on the geometrical phase analysis, Ultramicroscopy, 106 (2005) 1-17.

[6] S. Kim, S. Lee, Y. Oshima, Y. Kondo, E. Okunishi, N. Endo, J. Jung, G. Byun, S. Lee, K. Lee, Scanning moire fringe imaging for quantitative strain mapping in semiconductor devices, Appl Phys Lett, 102 (2013).

[7] F.H. Baumann, High precision two-dimensional strain mapping in semiconductor devices using nanobeam electron diffraction in the transmission electron microscope, Appl Phys Lett, 104 (2014).

[8] M.J. Hytch, A.M. Minor, Observing and measuring strain in nanostructures and devices with transmission electron microscopy, Mrs Bull, 39 (2014) 138-146.

[9] A.D. Krawitz, T.M. Holden, The Measurement of Residual-Stresses Using Neutron-Diffraction, Mrs Bull, 15 (1990) 57-64.

[10] B.E. Warren, X-ray diffraction, Dover ed., Dover Publications, New York, 1990.

[11] J. Keckes, M. Bartosik, R. Daniel, C. Mitterer, G. Maier, W. Ecker, J. Vila-Comamala, C. David, S. Schoeder, M. Burghammer, X-ray nanodiffraction reveals strain and microstructure evolution in nanocrystalline thin films, Scripta Mater, 67 (2012) 748-751.

[12] V. Senez, A. Armigliato, I. De Wolf, G. Carnevale, R. Balboni, S. Frabboni, A. Benedetti, Strain determination in silicon microstructures by combined convergent beam electron diffraction, process simulation, and micro-Raman spectroscopy, J Appl Phys, 94 (2003) 5574-5583.

[13] L. Jones, S. Wenner, M. Nord, P.H. Ninive, O.M. Lovvik, R. Holmestad, P.D. Nellist, Optimising multi-frame ADF-STEM for high-precision atomic-resolution strain mapping, Ultramicroscopy, 179 (2017) 57-62.

[14] J.M. Zuo, A.B. Shah, H. Kim, Y.F. Meng, W.P. Gao, J.L. Rouviere, Lattice and strain analysis of atomic resolution Z-contrast images based on template matching, Ultramicroscopy, 136 (2014) 50-60.

[15] A.B. Yankovich, B. Berkels, W. Dahmen, P. Binev, S.I. Sanchez, S.A. Bradley, A. Li, I. Szlufarska, P.M. Voyles, Picometre-precision analysis of scanning transmission electron microscopy images of platinum nanocatalysts, Nat Commun, 5 (2014).

[16] J.M. Zuo, Automated Lattice-Parameter Measurement from Holz Lines and Their Use for the Measurement of Oxygen-Content in Yba2cu3o7-Delta from Nanometer-Sized Region, Ultramicroscopy, 41 (1992) 211-223.

[17] J.M. Zuo, M. Kim, R. Holmestad, A new approach to lattice parameter measurements using dynamic electron diffraction and pattern matching, J Electron Microsc, 47 (1998) 121-127.

[18] A. Beche, J.L. Rouviere, L. Clement, J.M. Hartmann, Improved precision in strain measurement using nanobeam electron diffraction, Appl Phys Lett, 95 (2009).

[19] F. Uesugi, A. Hokazono, S. Takeno, Evaluation of two-dimensional strain distribution by STEM/NBD, Ultramicroscopy, 111 (2011) 995-998.

[20] K. Muller, A. Rosenauer, M. Schowalter, J. Zweck, R. Fritz, K. Volz, Strain Measurement in Semiconductor Heterostructures by Scanning Transmission Electron Microscopy, Microsc Microanal, 18 (2012) 995-1009.

[21] V.B. Ozdol, C. Gammer, X.G. Jin, P. Ercius, C. Ophus, J. Ciston, A.M. Minor, Strain mapping at nanometer resolution using advanced nano-beam electron diffraction, Appl Phys Lett, 106 (2015).

[22] D. Cooper, T. Denneulin, N. Bernier, A. Beche, J.L. Rouviere, Strain mapping of semiconductor specimens with nm-scale resolution in a transmission electron microscope, Micron, 80 (2016) 145-165.

[23] J.M. Zuo, J.C.H. Spence, Advanced Transmission Electron Microscopy : Imaging and Diffraction in Nanoscience, in, Springer New York New York, NY, 2017.

[24] J.M. Cowley, Electron nanodiffraction: Progress and prospects, J Electron Microsc, 45 (1996) 3-10.

[25] J. Tao, D. Niebieskikwiat, M. Varela, W. Luo, M.A. Schofield, Y. Zhu, M.B. Salamon, J.M. Zuo, S.T. Pantelides, S.J. Pennycook, Direct Imaging of Nanoscale Phase Separation in La0.55Ca0.45MnO3: Relationship to Colossal Magnetoresistance, Phys Rev Lett, 103 (2009).

[26] J.-M. Zuo, J. Tao, Scanning electron nanodiffraction and diffraction imaging, in: Scanning Transmission Electron Microscopy, Springer, 2011, pp. 393-427.

[27] P.A. Midgley, A.S. Eggeman, Precession electron diffraction - a topical review, Iucrj, 2 (2015) 126-136.

[28] K.H. Kim, H. Xing, J.M. Zuo, P. Zhang, H.F. Wang, TEM based high resolution and low-dose scanning electron nanodiffraction technique for nanostructure imaging and analysis, Micron, 71 (2015) 39-45.

[29] J.L. Rouviere, A. Beche, Y. Martin, T. Denneulin, D. Cooper, Improved strain precision with high spatial resolution using nanobeam precession electron diffraction, Appl Phys Lett, 103 (2013).

[30] C. Mahr, K. Muller-Caspary, T. Grieb, M. Schowalter, T. Mehrtens, F.F. Krause, D. Zillmann, A. Rosenauer, Theoretical study of precision and accuracy of strain analysis by nano-beam electron diffraction, Ultramicroscopy, 158 (2015) 38-48.

[31] T.C. Pekin, C. Gammer, J. Ciston, A.M. Minor, C. Ophus, Optimizing disk registration algorithms for nanobeam electron diffraction strain mapping, Ultramicroscopy, 176 (2017) 170-176.

[32] R. Yuan, Y. Meng, J. Zhang, J.-M. Zuo, Accurate Diffraction Peak Identification for Scanning Electron Nanodiffraction Based on Automated Image Processing and Feature Detection, Microsc Microanal, 23 (2017) 180-181.

[33] H.K. Yuen, J. Princen, J. Illingworth, J. Kittler, Comparative-Study of Hough Transform Methods for Circle Finding, Image Vision Comput, 8 (1990) 71-77.

[34] T.J. Atherton, D.J. Kerbyson, Size invariant circle detection, Image Vision Comput, 17 (1999) 795-803.

[35] J.T. McKeown, J.C.H. Spence, The kinematic convergent-beam electron diffraction method for nanocrystal structure determination, J Appl Phys, 106 (2009).

[36] J.C.H. Spence, J.M. Zuo, Electron microdiffraction, Plenum Press, New York, 1992.

[37] J.M. Gibson, M.M.J. Treacy, The Effect of Elastic Relaxation on the Local-Structure of Lattice-Modulated Thin-Films, Ultramicroscopy, 14 (1984) 345-349.

CHAPTER 4

PRECISION ORIENTATION AND LATTICE STRAIN MAPPING USING ARTIFICIAL NEURAL NETWORKS

In this chapter, techniques for training artificial neural networks (ANNs) and convolutional neural networks (CNNs) using simulated dynamical electron diffraction patterns are described. The premise is based on the following facts. First, given a suitable crystal structure model and scattering potential, electron diffraction patterns can be simulated accurately using dynamical diffraction theory. Secondly, using simulated diffraction patterns as input, ANNs can be trained for the determination of crystal structural properties, such as crystal orientation and local strain. Further, by applying the trained ANNs to four-dimensional diffraction datasets (4D-DD) collected using the scanning electron nanodiffraction (SEND) or 4D scanning transmission electron microscopy (4D-STEM) techniques, the crystal structural properties can be mapped at high spatial resolution. Here, we demonstrate the ANN-enabled possibilities for the analysis of crystal orientation and strain at high precision and benchmark the performance of ANNs and CNNs by comparing with previous methods. A factor of thirty improvement in angular resolution at 0.009° (0.16 mrad) for orientation mapping, sensitivity at 0.04% or less for strain mapping, and improvements in computational performance are demonstrated.

4.1. Introduction

Real crystals contain various defects. Colin Humphreys, whose career we are celebrating here together with those of John Spence and Knut Urban, famously stated "Crystals are like people: it is the defects in them which tend to make them interesting" [1]. Examples of technological importance are many, such as, dopant atoms are used to control the electronic properties of semiconductors, dislocations underly crystal plasticity, and vacancy defects give rise to ionic conductivity. Real crystals are traditionally imaged using the so-called diffraction contrast in transmission electron microscopy (TEM) [2]. With the development of high-resolution electron microscopy (HREM), to which John Spence and Knut Urban have dedicated a large part of their research careers, the interruption of crystal lattice by dislocations or stacking faults can be observed directly [3, 4]. Impurity atoms and atomic disorder, under favorable conditions such as very thin crystals, can also be imaged [5-7]. Together, diffraction contrast imaging and HREM have contributed to much of our experimental knowledge about defects. However, unlike X-ray diffraction, quantitative analysis of real crystals has always been a challenge for TEM. Basic crystal information, such as the thickness and orientation of a crystalline sample, is only obtained under favorable conditions such as single crystal diffraction using convergent beam electron diffraction [8] and ultra-thin samples using quantitative HREM [9]. Here, we explore the possibilities offered by recent progress of artificial neural networks (ANNs) for precision diffraction analysis through the design and benchmark of ANNs for orientation and strain mapping applications.

ANNs are statistical learning algorithms that are modeled loosely after how human brain recognizes patterns. An ANN is typically organized in hierarchical layers, patterns are presented to the network via the input layer, which communicates to one or more 'hidden layers'. The hidden layers are then linked to an output layer where the answer is presented. Each layer in an ANN is made up of multiple processing elements, also called nodes or neurons, which are interconnected with nodes in the neighboring layers. The connection between two different nodes is assigned a numerical value, called weight. The output from one layer is used as input to the next layer. By systematically tuning the weights through an optimization process, the network can accurately approximate an arbitrary function. Once an ANN is structured for a targeted application, it must be trained using machine learning. In the so-called supervised learning, a set of labeled data containing both input and output (label) are presented to an ANN. The network is trained by comparing the output of the ANN against the desired output and updated by back propagation, in which the system adjusts the weights. This process is then repeated to optimize the weights. One of the major breakthroughs in the field of machine learning is the invention of convolutional neural networks (CNNs), which are ANNs containing multiple convolutional layers in addition to fully connected layers as in traditional ANNs [10]. CNNs are capable of deep learning to progressively extract higher level features from the raw input, for the recognition of complex patterns.

The abilities of machine learning, including deep learning, using ANNs present exciting opportunities for the analysis automation and augmentation of electron microscopy data [11-13]. In computer vision, deep learning has been used to solve difficult problems, such as classification, segmentation and detection [14]. In the field of electron microscopy, deep learning has been applied to, or proposed for, crystal symmetry determination in electron backscatter diffraction (EBSD) [15], the crystallographic analysis of electron image and diffraction data [12], resolution enhancement in scanning electron microscopy (SEM) images [16], defect analysis using simulated electron images [17], single atom detection [11, 13], and matching of experimental and simulated position averaged convergent-beam electron diffraction (PACBED) pattern for the determination of crystal thickness and tilt [18]. On the other hand, unsupervised machine learning methods, for example non-negative matrix factorization and clustering, have also been demonstrated their usefulness in electron diffraction through automatic learning of microstructural features contained in 4D data without the need of model training [19, 20].

This chapter focuses on machine learning techniques for precision electron diffraction pattern analysis. The targeted electron diffraction patterns are electron nanodiffraction patterns obtained using a small focused beam. The motivation is to train ANNs for regression analysis based on the information of individual diffraction disks, their intensities and positions, instead of the whole diffraction patterns as done in the case of position averaged convergent beam electron diffraction (PACBED) [18]. As the size of input data reduces, the structure of ANNs can be simplified and the number of parameters to be optimized can be reduced, which provides significant benefits regarding the computational requirements and the reduced complexity of ANNs. For the training, we used the simulated dynamic electron nanodiffraction patterns. Experimental diffraction patterns are recorded from a sample region using the SEND technique [21], which is also known as 4D-STEM when it is performed in a STEM [22]. These techniques collect a 4D diffraction dataset (4D-DD) with two reciprocal space coordinates $\left(k_x, k_y\right)$ and two real space coordinates $\left(x, y\right)$. Automated analysis of 4D-DD is a central part of electron diffraction imaging. Here, we introduce the design, testing and benchmarking of ANNs for two applications of SEND. The first is precision crystal orientation mapping using a trained ANN, where we determine small changes in crystal orientation within a crystalline grain. In the second example, a CNN is trained to measure the position of electron diffraction disks to map crystal strain fields. For testing and benchmarking, the results obtained with trained neural networks are compared with the established correlation analysis technique [23, 24] for orientation mapping and the circular Hough transform (CHT) method [25] for strain mapping. To demonstrate the application potentials of trained neural networks, we apply our methods to image grain subdivision inthe nuclear fuel material of UO_2 after irradiation and a fin field effect transistor (FinFET) device. Using these cases, we demonstrate the steps required to take the full advantage of neural networks for electron diffraction.

4.2. Methods

4.2.1. Scanning electron nanodiffraction

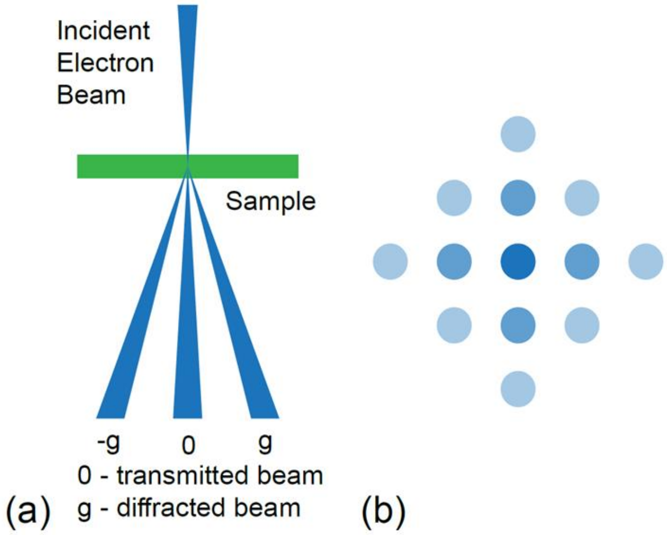

Fig. 4.1. Electron nanodiffraction using a small focused beam as illustrated by the schematic diagrams of (a) diffraction geometry and (b) diffraction pattern.

The types of electron diffraction patterns we analyze here are electron nanodiffraction patterns collected using the scanning electron nanodiffraction (SEND) technique [21, 26]. Here, we provide a brief summary on the key points of this technique.

Electron nanodiffraction patterns are recorded using a focused electron probe at a thin sample (Fig. 4.1). The beam convergence angle is in a few mrads, which yields small diffraction disks in the recorded patterns. The electron probe size, in the absence of lens aberrations, is diffraction limited according to $d_{FWHM} = 0.52\frac{\lambda}{\theta}$ for the full-width half maximum (FWHM) probe size. At θ = 1 mrad and λ = 1.9 pm for the 300 kV electrons, and d_{FWHM} = 1 nm. Sub-nm probes can be obtained by increasing θ to a few mrad, in which case larger diffraction disks are recorded as in convergent beam electron diffraction (CBED).

The information recorded in a diffraction pattern can be quantified and categorized based on 1) diffraction geometry, in the form of Bragg-diffracted beams whose position and arrangements are related to the crystal unit cell structure and crystal orientation, and 2) diffraction intensity, which is related to the crystal structure, electron beam energy, sample thickness and sample orientation. Nanodiffraction patterns from a thin crystal show very little feature within each diffracted disk. This leads to the possibility of using the average, or integrated, disk intensity for structural analysis [27]. As the convergence angle increases, more complex diffraction patterns are recorded in thicker crystals due to the larger angular range and deviations from the Bragg diffraction condition [28]. In the applications here, we use dynamical diffraction for intensity prediction to improve the measurement accuracy.

The spatial resolution of electron nanodiffraction is ultimately limited by the electron probe size d_{FWHM} and the cone diameter under the column approximation. The diameter of the cone d_{AB} in a thin sample is defined approximately as

$$d_{AB} = 2\alpha t, \tag{4.1}$$

where α is the convergence semi-angle and t is the sample thickness. The radius of the first Fresnel zone ρ_1 used to represent the diffraction column is calculated using

$$\rho_1 = \sqrt{\lambda t}, \tag{4.2}$$

where λ is the electron beam wavelength. At 300kV, λ = 1.9 pm. If the convergence semi-angle is 1 mrad and sample thickness is 80 nm, d_{AB} is 0.2 nm and ρ_1 is 0.4 nm.

4.2.2. TEM samples

To demonstrate the applicability of our methodology as well as to test the method's reliability, we selected following samples. A thin single crystal sample of GaSb with the bending contour contrast, an irradiated polycrystalline UO_2 sample with grain subdivision and associated small angle boundaries, and a FinFET transistor device where SiGe is introduced to generate strain fields [25]. The UO_2 sample was prepared from a spent light water fuel from Belgium Reactor 3 (BR3) with an average burn-up of 4.5 at% [29]. The GaSb was mechanically thinned and then polished using ion beam milling. Both the UO_2 and FinFET samples were prepared by the focused ion beam (FIB) methods.

4.2.3. Experimental diffraction data collection

We acquired electron nanodiffraction patterns using a Themis Z S/TEM (Thermo Scientific, Waltham, USA), installed at University of Illinois. The microscope was operated in the μProbe STEM mode with the acceleration voltage of 300 kV. The electron probe focused on the sample had a semi-convergence angle of 1.2 mrad, and the probe size of 1.0 nm in FWHM. For precision crystal orientation measurement of GaSb, camera length was set at 185 mm, where about 40 diffraction peaks adjacent to the center beam in the $[1\bar{1}0]$ zone axis were included in the recorded patterns. For strain mapping in the FinFET device, camera length was set at 360 mm so that only 8 diffraction peaks adjacent to the center beam were included. Diffraction patterns were recorded using a CMOS camera (Ceta, Thermo Scientific) at the resolution of 1024×1024 pixels and 0.1 s exposure time per diffraction pattern. The 4D-DD acquisition was automated by a control software provided by Thermo Scientific. During the scan, a STEM image, containing the sample region, was also acquired using the high-angle annular dark-field (HAADF) detector after each row scan for sample drift correction. The 4D-DD on irradiated UO_2 was collected using a Talos F200X S/TEM (Thermo Scientific, Waltham, USA), installed at Idaho National Laboratory, in μProbe STEM mode at 200 kV. The probe semi-convergence angle was 0.9 mrad and the probe size was 1.9 nm in FWHM. The camera length of 98 mm was used to obtain a large number of diffraction peaks adjacent to the center beam along the [112] zone axis direction. The detector setting in this case was same as the one used for GaSb.

4.2.4. Simulation of electron diffraction patterns

To build the diffraction pattern libraries for ANN training, electron nanodiffraction patterns were simulated using the Bloch wave method. The Bloch software was used for this purpose [8]. Three sets of diffraction library were built. The first one is for crystal orientation determination, where diffraction patterns of single crystal GaSb were simulated in a tilt series up to 0.5 degree tilt from the $[1\bar{1}0]$ zone axis at a step size of 0.02 degree. The crystal tilt is defined by two tilt angles $(tilt_x, tilt_y)$, which refer to the incident beam angle to a selected zone axis in degrees. They are used to calculate the tangential component of the incident wave vector

$$\overrightarrow{k_t} = \frac{tilt_x}{\lambda} \cdot \frac{\pi}{180} \vec{g} + \frac{tilt_y}{\lambda} \cdot \frac{\pi}{180} \vec{h}, \tag{4.3}$$

where λ is the electron beam wavelength, $\vec{g}$ and $\vec{h}$ are two orthogonal unit vectors in the reciprocal space. We have assumed the tilt angles are small as in our experimental cases. The tilt series calculations were repeated for the crystal thickness from 65 to 85 nm at a step size of 5 nm. Both the tilt and thickness ranges were chosen to cover the estimated tilt and thickness variations in the GaSb sample. In total, 13,005 diffraction patterns were simulated.

Another simulation library was built for the orientation determination of UO_2. Diffraction patterns of single crystal UO_2 were simulated in a tilt series up to 2 degrees tilt from the [112] zone axis at a step size of 0.1 degree. The tilt series was repeated for the crystal thickness from 50 to 90 nm at a step size of 10 nm with a total of 8,405 diffraction patterns.

The third library was calculated for the d-spacing determination in a FinFET device. Diffraction patterns of single crystal Si with the thickness of 10, 15, and 20 nm were simulated in a tilt series with up to 0.6 degree tilt along the [110] and [001] directions from the $[1\bar{1}0]$ zone axis at a step size of 0.3 degree. The thickness was selected based on the estimated thickness of the crystalline SiGe in the FinFET device. The camera length was set so that the radius of the diffraction disks is 45 pixels, same as the SEND experiment. A total of 43 sub-images of 121-by-121 pixels with each containing a single diffraction disk were cropped out from each simulated diffraction pattern. Among all the simulated diffraction disks, a library of 10,000 disk images were randomly selected to train the convolutional neural network. Random disk shift was applied to each disk image. We also added random noise to the disk images using the additive white Gaussian noise (AWGN) method with a varying signal-to-noise ratio (SNR) of 15~30 dB to mimic the diffuse scattering and detector noise in the experimental patterns. Examples are shown in Fig. 4.2.

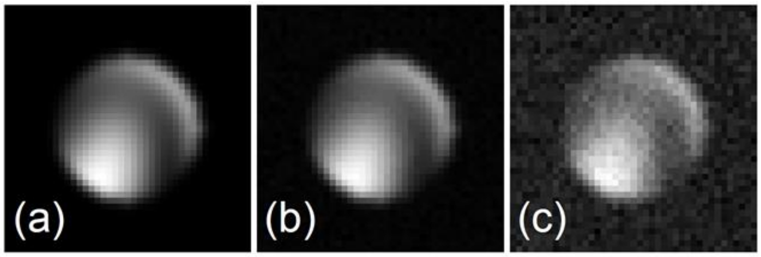

Fig. 4.2. Gaussian noise added to mimic experimental diffraction patterns. Simulated diffraction disks with (a) no noise, and with noise level of (b) 30 dB and (c) 15 dB signal-to-noise ratio (SNR).

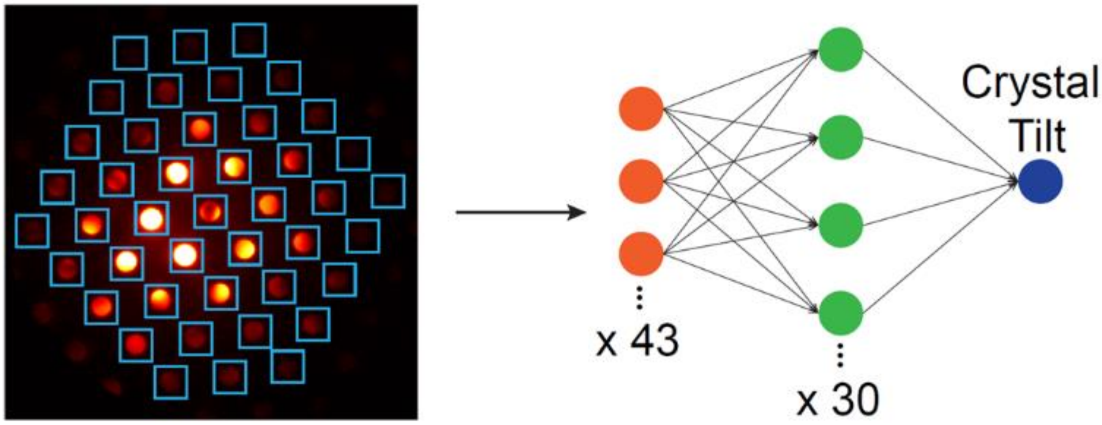

Fig. 4.3. The design of an ANN for precision crystal orientation determination based on integrated diffraction intensities. In the diffraction pattern example here, 43 blue boxes centered on the diffraction disks are used to calculate the integrated diffraction intensity as input to the neural network.

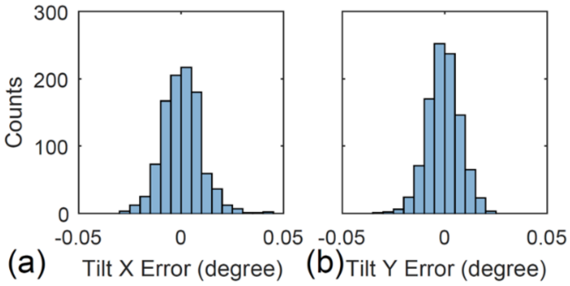

Fig. 4.4. Theoretical accuracy of orientation determination using ANN tested by simulated diffraction patterns. Histograms of measurement error in (a) tilt X and (b) tilt Y.

4.2.5. Training artificial neural networks for precision crystal orientation mapping

An ANN for regression was built for GaSb precision orientation mapping using 4D-DD. The simulated diffraction patterns are 1024×1024 pixels in size. For the training data, we integrated the diffraction intensities of 43 reflections as marked with blue boxes in Fig. 4.3. The blue boxes sit on a 2D grid, which were adjusted manually to make sure all diffraction disks reside close to the centers of corresponding boxes. In this way, the input data is greatly reduced from a 1024×1024 image to 43 integrated intensities. To mimic the variations in experimental diffraction intensities, we also added the Gaussian noise to the integrated intensities with a varying SNR of 15~30 dB. For the ANN, we used a simple three-layer model, which contains an input layer of 43 integrated intensities, 30 neurons in the hidden layer using the Sigmoid function as activation function, as shown in Fig. 4.3. The output layer determines the crystal tilt angle along X||[001] direction in the $[1\bar{1}0]$ zone axis pattern without nonlinear activation. Tilt angle along Y||[110] is determined by another ANN with the same structure as tilt X. The ANNs were trained with the Levenberg–Marquardt backpropagation algorithm [30] using the 13,005 simulated diffraction patterns of GaSb with different orientations near $[1\bar{1}0]$ and thicknesses, as described in Section 4.2.4. The training dataset contains a range of different thicknesses to help the ANNs to minimize errors in orientation determination due to sample thickness variations. Both input (disk intensity) and output (tilt angle) were normalized to 0~1 for better training performance.

To evaluate the accuracy of orientation determination using the trained ANNs, we simulated another 1,000 diffraction patterns as test data with random crystal tilts up to 0.5 degree from the $[1\bar{1}0]$ axis and random thicknesses from 65 to 85 nm. The same level of noise was applied to the test data and the training data. The difference between the simulated test patterns and the training library for the ANN is that the tilt angles and thicknesses in the test patterns are no longer on grids with the steps of 0.02 degree in tilt and 5 nm in thickness. The trained ANNs are applied to the test data to measure the orientation. The deviation in tilt angles from their true values are defined as error, the error distribution is plotted in Fig. 4.4. The accuracy of this method can be estimated by the standard deviations of the error, which are 0.0092 degree (0.16 mrad) in tilt X and 0.0078 degree (0.14 mrad) in tilt Y, respectively.

To test the performance of ANNs on real experimental data, we chose two diffraction patterns, A and B from the GaSb sample, which are separated from each other in the 4D-DD. The crystal orientation was first determined by the trained ANNs. For pattern A (Fig. 4.5a), the tilt angles from $[1\bar{1}0]$ axis are -0.2010° and -0.0537° along X and Y, respectively. The tilt angles of pattern B (Fig. 4.5d) are determined to be -0.2724 ° and 0.0947° along X and Y, respectively. Then, we simulated diffraction patterns with these determined tilt angles, and compared them with the experimental patterns with the crystal thickness of 80 nm (which gives the best match). The results are displayed in Fig. 4.5. The good matching in both Fig. 4.5a, b and Fig. 4.5d, e indicates the high accuracy of the trained ANNs, even though the intensity variations in the diffracted disks were not taken into account when the integrated disk intensities were used for the ANN training. Quantitative comparison of the integrated intensities from the experimental and simulation patterns is made in Fig. 4.5c and f, where the intensities of 15 strongest diffraction disks, normalized by the highest intensity, are plotted. The difference between experiment and simulation is quantified by the R-factor,

$$R = \frac{\sum |I_{exp} - I_{sim}|}{\sum I_{exp}}, \tag{4.4}$$

which is *R* = 26% for Fig. 4.5c and 19% for Fig. 4.5f, respectively. This shows that the above method is robust even though the experimental integrated intensities do not match the simulation exactly.

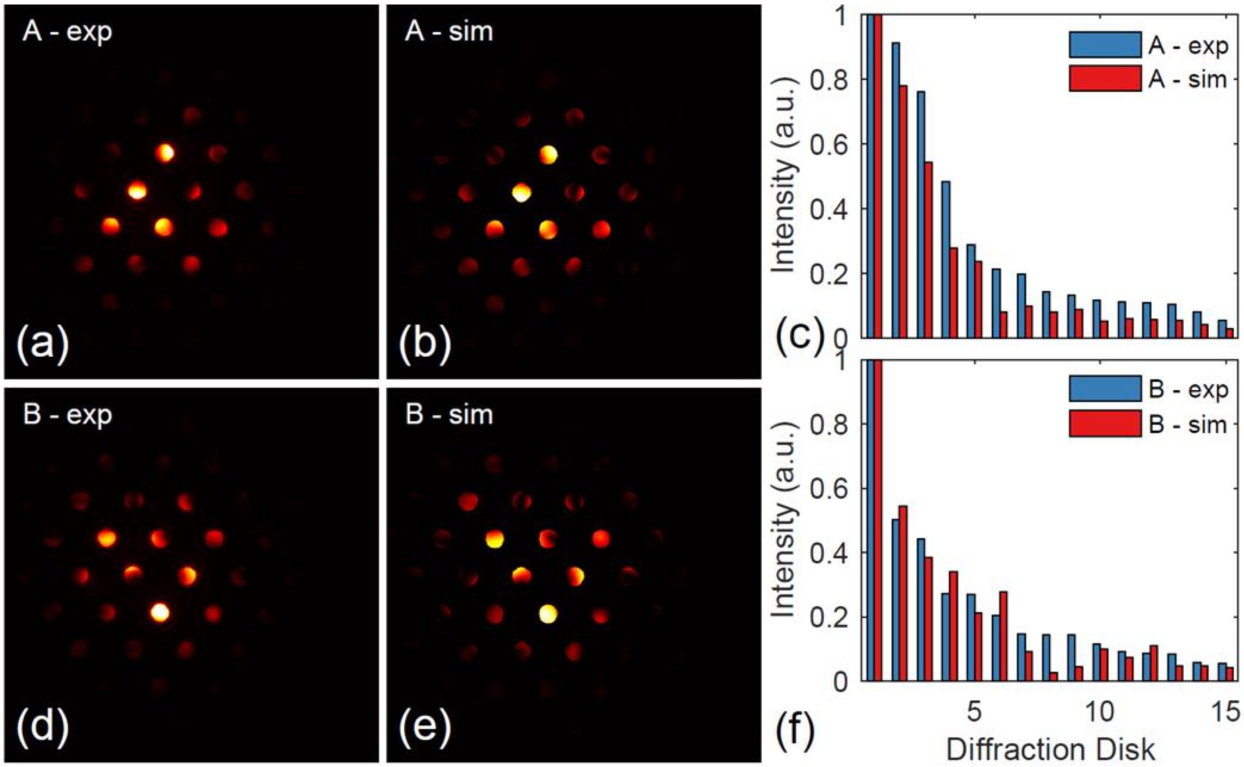

Fig. 4.5. Comparison between experimental GaSb diffraction patterns and simulated diffraction patterns with crystal orientation determined by the ANNs. (a)(d) Experimental patterns, (b)(e) best matching simulated patterns as identified by the ANNs, and (c)(f) integrated intensity of 15 brightest disks sorted according to the intensity value for experimental and best matching patterns of A and B, respectively.

The ANNs for precision orientation determination of the irradiate UO_2 sample were designed using the similar approach as the ones designed for GaSb, except that in this case 35 integrated diffraction intensities were selected from patterns near the [112] zone axis. As the range of orientations we want to cover is much larger than the GaSb case, the number of hidden layers was increased from one to three, which improved the accuracy of the regression from 0.45 degree in $tilt_x$ and 0.43 degree in $tilt_y$ to 0.29 degree in $tilt_x$ and 0.24 degree in $tilt_y$. These estimations were based on 1,000 simulated diffraction patterns of UO_2 of random orientation within 2 degrees tilt from the [112] zone axis and random thickness between 50 and 90 nm.

4.2.6. Training convolutional neural networks for strain mapping

The principle of strain mapping is based on a determination of local d-spacing using electron nanodiffraction. The d-spacing is measured from the disk positions in the recorded diffraction patterns and by applying Bragg's law [25]. Critical to the whole process is to measure the positions of diffraction disks. This task is nontrivial due to the uneven intensity distribution that is typically observed in recorded diffraction disks, which is caused by dynamical diffraction.

The CNN model shown in Fig. 4.6 was built in TensorFlow. The input layer takes in the disk images of 121×121 pixels in this case, followed by two sets of 3×3×8 convolution layer with ReLU activation and 2×2 max-pooling layer combination, which help to extract high-level features from the input images and reduce the size. Then a fully connected layer of 128 neurons with Sigmoid activation is used to calculate the output of disk position X from the center of the image. The simulation library of 10,000 randomly shifted diffraction disks was used as training data. Adam [31] was used as the optimizer and the mean squared error was used as loss function.

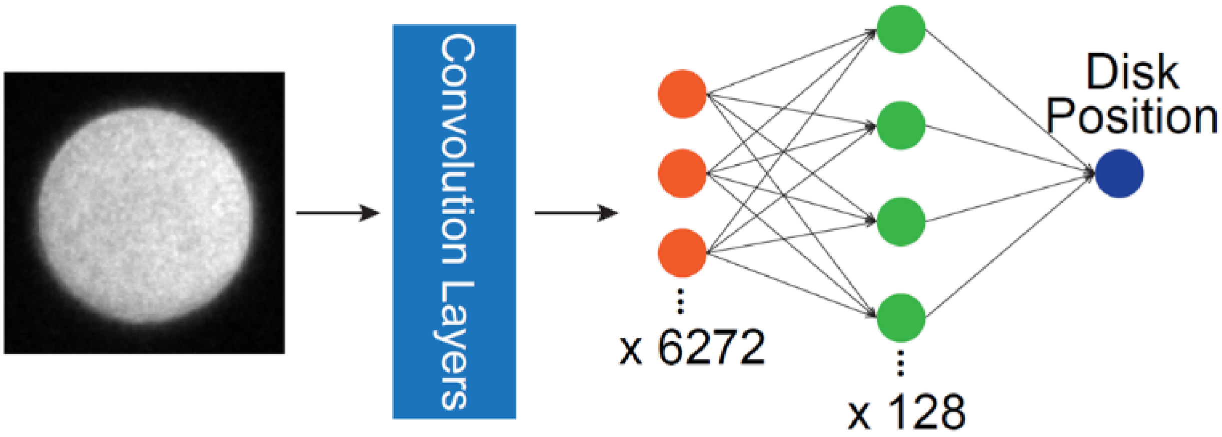

Fig. 4.6. Convolutional neural networks for diffraction disk position determination. The input is a 121×121-pixel image containing a single diffraction disk.

Although the disk position we try to measure is two-dimensional, displacements in horizontal and vertical directions are independent to each other. In order to measure the disk position in both directions, we can simply apply the ANN to each disk image twice, once to the original image, the other to the image transposed. Considering the mirror symmetry associated with determination of disk position along one direction, the disk image is also flipped upside down for the second measurement of the horizontal displacement and left to right for the second measurement of the vertical displacement. Two measurements using the mirrored images are averaged to reduce the error.

The accuracy of the trained CNN for disk position determination was estimated by applying the trained CNN to a new batch of 1,000 simulated diffraction disks randomly selected from the simulation library. The same level of random displacements and noise were added to the new batch as the training data. The error distribution is displayed in Fig. 4.7. The standard deviations of the error are calculated to be 0.070 and 0.093 in pixel in horizontal and vertical directions, respectively.

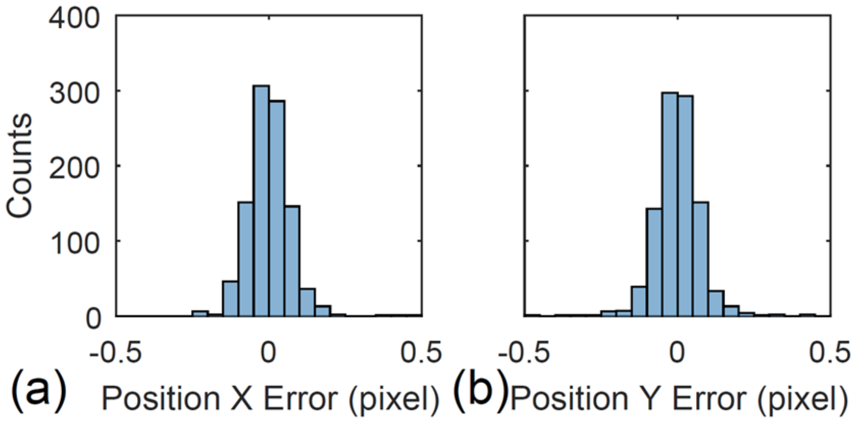

Fig. 4.7. Theoretical accuracy of disk position determination using CNN tested by simulated diffraction disks. Histograms of errors in the determined disk positions along (a) horizontal and (b) vertical directions.

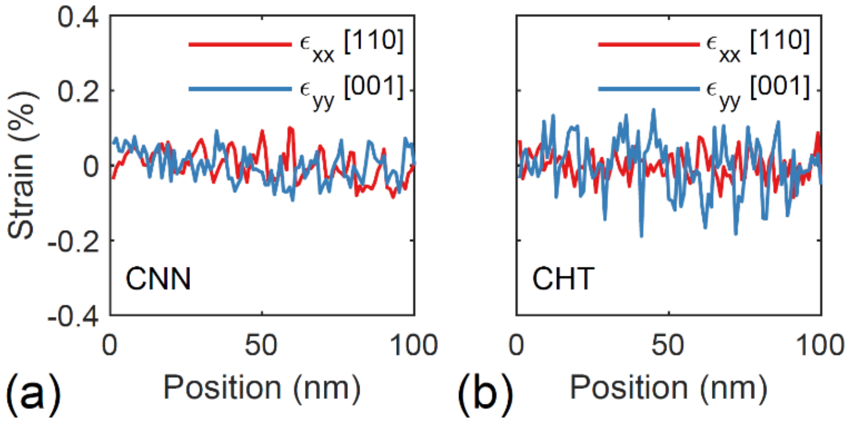

Fig. 4.8. Strain profiles from a SEND scan on a flat Si sample. Strain is measured by detecting diffraction disk positions using (a) the trained CNN, and (b) the CHT method.

Once the disk positions are determined, we follow the methods described in Ref. [25] to obtain strain. The precision of strain measurement using the trained CNN as a disk detection method was evaluated using a calibration SEND scan on a flat Si sample. The strain profiles calculated by CNN method are plotted in Fig. 4.8 along with those calculated by the CHT method

[25] using the same dataset. The standard deviation of the strain in the calibration scan is taken as the upper limit of strain measurement precision, which is 0.041% along the [110] direction and 0.042% along the [001] direction for CNN results, and 0.036% along [110] and 0.076% along [001] for CHT results, respectively. The improvement of precision in strain along [001] shows the advantage of CNN method that it takes into account of the intensity of ±(400) diffraction disks, which because of its large scattering angle fluctuates from one pattern to another. The comparable precision along [110] is attributed to the robustness of both methods and the residual strain in the sample.

4.3. Applications

4.3.1. Precision orientation mapping of a GaSb thin sample

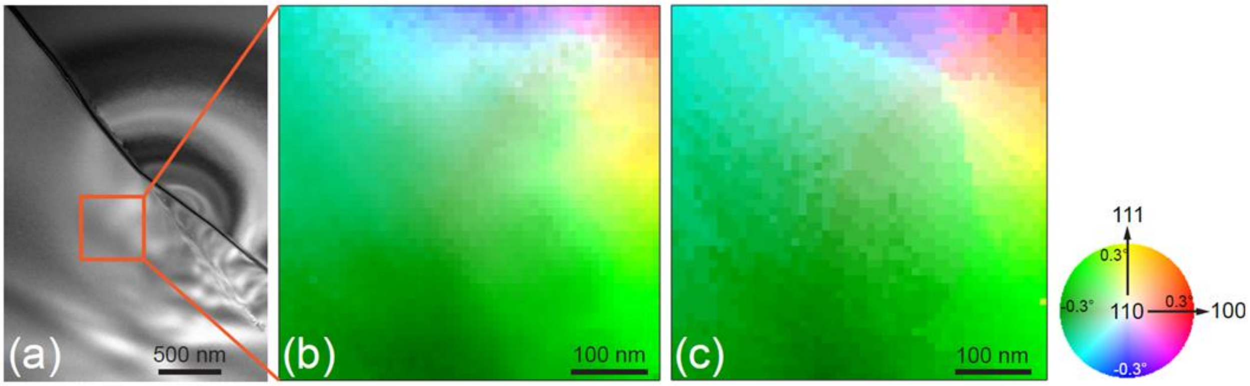

Fig. 4.9. Precision orientation mapping of a thin GaSb sample. (a) Annular dark-field image (ADF) showing diffraction contrast near a crack in the sample. Orange box marks the area of the 4D-DD was collected. (b) Orientation maps are calculated from the 4D-DD using (b) the ANN method and (c) the pattern matching method.

To demonstrate the sensitivity of precision orientation mapping using trained ANNs, we first applied the method to a hand polished GaSb thin sample in which bending is observed near a defect. Fig. 4.9a shows an image acquired using the same optics as SEND by an annular dark-field (ADF) detector with collection angles of 31~185 mrad. Dramatic diffraction contrast is seen in the ADF image, which can be attributed to crystal bending (local orientation variation) and thickness variation. A 4D-DD is acquired over a region of 500×500 nm^2, with a step size of 10 nm. Each electron nanodiffraction pattern in the dataset is reduced to 43 integrated disk intensities as the input for the ANNs trained for crystal orientation determination as described in Section 4.2.5. After applying the ANNs to each pattern in the 4D-DD, a 2D orientation map is obtained and displayed in Fig. 4.9b. The gradual change in the orientation map indicates continuous bending in the region close to defect within the angular range of ±0.3°. The angular resolution demonstrated here is consistent with the simulation estimation of 0.0092°. This is a significant improvement over the angular sensitivity of ~0.3 to 0.8° reported using the template matching method based on kinematical simulation [23, 24].

To compare, we applied the pattern matching method to the same dataset. In this method, each experimental diffraction pattern in the 4D-DD is compared with the library of simulated GaSb diffraction patterns to find the best match. First, both of the experimental and simulation diffraction patterns are reduced to a list of integrated intensities following the same procedures we used in the ANN method. Next, the Pearson correlation coefficient between the experimental intensity list and the simulated intensity list is calculated.

$$PCC(x,y) = \frac{\sum_i (x_i-\bar{x})(y_i-\bar{y})}{\sqrt{\sum_i (x_i-\bar{x})^2 \sum_i (y_i-\bar{y})^2}}, \tag{4.5}$$

where x and y represent experimental and simulated intensities, respectively. While PCC produces similar results as normalized cross-correlation (NCC), it is reported that PCC can be less sensitive to variations in background intensity [32]. This is repeated for each diffraction pattern in the library. The best match is selected based on the largest correlation value. The orientation map is obtained by plotting the best match for each experimental pattern in the 4D-DD (Fig. 4.9c).

The orientation maps obtained using the two different methods show the same trend but differ in some of the details. One obvious difference is the smoothness of the maps. While the pattern matching results are in the discrete steps of 0.02° with the step size determined by the simulation, the ANN method is able to produce interpolated results, due to the multivariate regression nature of the trained neural network.

4.3.2. Precision orientation mapping of grain subdivision in irradiated UO_2

Grain subdivision is a phenomenon that occurs when the quantity of defects is increased, for example, in cold rolled metals [33] or in nuclear fuel [34, 35]. Subdivision is observed when a grain is divided into many sub grains of smaller size. The size and orientation of sub grains correlate with the amounts of defects and the type of defects. Radiation-induced grain subdivision in UO_2 is observed at the rim region of the fuel pellets with high burn-up [35]. The new structure, called high burn-up structure (HBS) or rim structure, is typically composed of sub-micron grains with respect to ~10 μm for the original grains. The main formation mechanism of HBS is still debated and generally considered as either irradiation-induced grain polygonization or grain recrystallization/growth process, featured with the formation of low-angle grain boundaries (LAGBs) and high-angle grain boundaries (HAGBs), respectively [36] Grain orientation or grain boundary nature is often characterized by EBSD and transmission kikuchi diffraction (tKD) in a

SEM. Each of these methods offers its unique advantages for materials characterization. TEM offers the highest spatial resolution. Here we demonstrate that the precision can be improved for TEM based diffraction applications.

To demonstrate the potential of ANNs for fine grain orientation mapping, we studied grain subdivision in an irradiated UO_2 Sample. UO_2 is of interest as a nuclear fuel material. The ADF image in Fig. 4.10a gives an overview of the sample being investigated. In the thin lamella prepared by FIB, there are three major crystalline grains where the grain boundaries are outlined by yellow lines in Fig. 4.10a. After irradiation, complex diffraction contrast appears near the grain boundaries indicating changes in the diffraction condition. A 4D-DD is acquired over a region of 2.5×2.5 μm^2, with step size of 25 nm, as marked in Fig. 4.10a. By averaging over all 10,000 diffraction patterns in the 4D-DD, a virtual selected area electron diffraction (SAED) pattern is obtained and shown in Fig. 4.10b. The SAED shows that the majority of this grain is in [112] zone axis, while the elongation of the diffraction spots indicates a mosaic spread within the crystalline grain, while the uneven contrast in the ADF image indicates the possibility of grain subdivision. By taking a close-up look at two diffraction patterns (Fig. 4.10c, e) taken from position A and B marked in Fig. 4.10a, a clear difference in crystal orientation is seen. However, the amount of change indicated by the diffraction patterns is small and around the [112] zone axis. To determine the change in crystal orientation, we applied the trained ANNs for UO_2 as described in Section 4.2.5 to these two patterns. The tilt angles of pattern A (Fig. 4.10c) from [112] axis are determined to be -0.4155° along X||[110] direction and -0.4385° along Y||[111] direction. The tilt angles of pattern B (Fig. 4.10e) are 0.1081° along X and 1.5119° along Y. The theoretical diffraction patterns of UO_2 with these orientations and thickness of 60 nm are simulated under the same condition as the experiment (Fig. 4.10d, f). The close match between experimental patterns and simulated ones for both A and B shows the accuracy of the ANN method.

Then we applied the ANNs to all patterns in the SEND dataset to generate a 2D orientation map as shown in Fig. 4.11b. Except the gray areas which are from vacuum or different grains with orientation far away from [112] zone, most of sub grains within the scanned area are orientated within 1° from [112]. The map clearly shows the spatial distribution and the size of small grains after subdivision sharing LAGBs with each other. As a comparison, Fig. 4.11a shows a virtual ADF image generated by integrating all diffracted beams in each pattern of the SEND dataset. While the diffraction contrast in virtual ADF image provides qualitative information about grain subdivision, our orientation map calculated by the ANN method produces quantitative information with high precision.

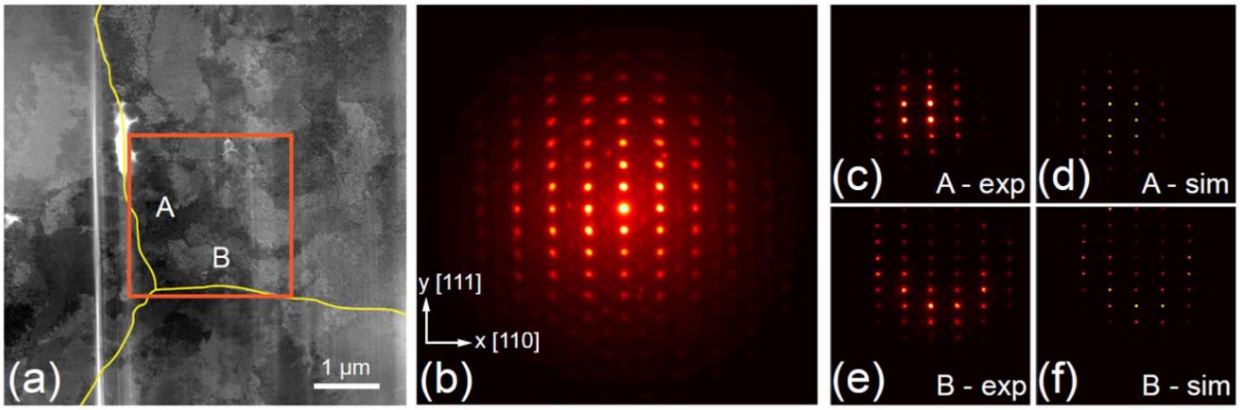

Fig. 4.10. Grain subdivision in irradiated UO_2. (a) Annular dark-field image of the sample region investigated by SEND. The yellow lines mark the original grain boundaries in the sample. Orange box denotes the area of 4D-DD acquisition. (b) Virtual selected area diffraction pattern generated from the 4D-DD showing a mosaic diffraction pattern due to grain subdivision. (c)(e) Selected experimental and (d)(f) simulated diffraction patterns with the orientation determined by the trained ANNs.

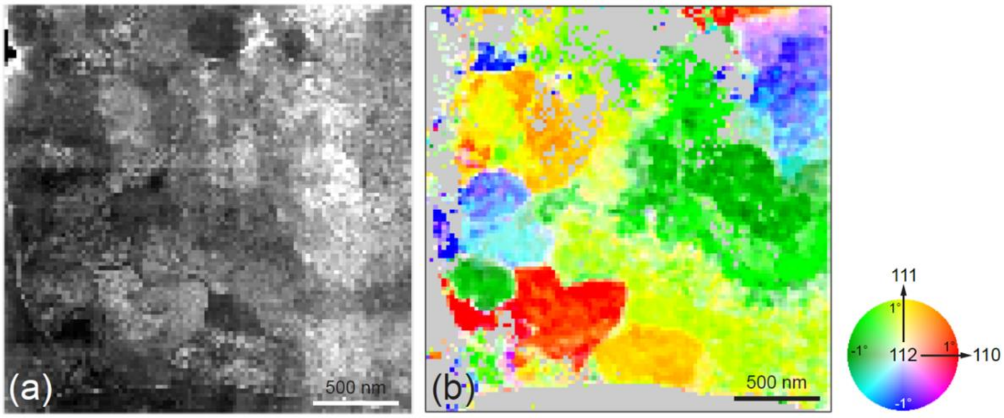

Fig. 4.11. Precision orientation mapping of grain subdivision in irradiated UO_2. (a) Virtual annular dark-field image generated from the SEND dataset showing diffraction contrast of multiple sub grains. (b) High-resolution quantitative orientation mapping obtained by ANN method. The gray color in the map indicates regions far away from [112] zone axis.

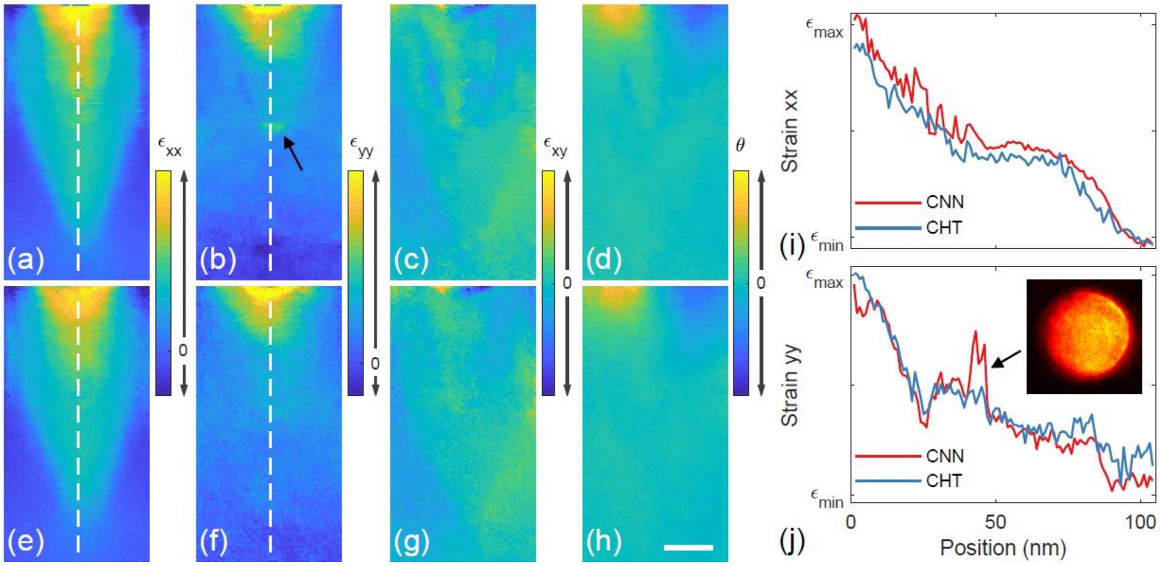

Fig. 4.12. Strain mapping of a Si-based FinFET device. (a-d) Strain maps calculated using CNNs for diffraction disk detection. (e-h) Strain maps calculated using CHT for diffraction disk detection. The scale bar is 20 nm. (i)(j) Strain profiles taken from white dashed lines in (a)(e) and (b)(f), respectively. The color scale indicates the strain values from low (blue) to high (yellow). The inset of (j) displays a distorted diffraction disk taken from the position marked by the black arrow in (b).

4.3.3. Lattice strain mapping of a Si-based FinFET device

To demonstrate the capability of local d-spacing determination using CNNs, the method is applied to a SEND dataset acquired on a sample of Si-based FinFET device of Intel 14 nm technology. The details of the sample and data acquisition are described elsewhere [25]. The SEND map has a size of 60×120 pixel, with pixel (step) size of 1 nm. Each diffraction pattern contains 8 lowest-order diffracted beams in addition to the center beam. 9 sub-images with size of 121×121 pixels containing individual diffraction disks were cropped out from the original diffraction pattern. The trained CNN model described in Section 4.2.6 was applied to each sub-image to determine the position of the diffraction disk in both horizontal and vertical directions. The measured disk positions were then used to fit a 2D reciprocal lattice. The strain was calculated based on the averaged reference taken from a flat region near the bottom of the scanned area, following the same procedure in our previous paper [25].

All four components of the 2D strain tensor were calculated and displayed in Fig. 4.12a-d, along with the stain maps calculated using the CHT method for disk detection from the same dataset in Fig. 4.12e-h. Overall distribution of the strain fields measured by two methods are very close to each other. Line profiles taken from the 2D maps as marked by white dashed lines in Fig. 4.12a, b, e, and f are displayed in Fig. 4.12i and j for direct comparison. Strain maps of CNN method appear smoother than those of CHT method, especially in ϵ_{yy}. This improvement is consistent with our estimation of strain measurement precision based on a calibration scan shown in Fig. 4.8. The most significant deviation between the two results can be seen in Fig. 4.12j near 45 nm region, marked by black arrows in Fig. 4.12b and j, where CNN result contains a sudden peak while CHT result is relatively flat. A closer look at the diffraction patterns at that region reveals that the peak in CNN result comes from the presence of additional diffuse diffraction disk

(Fig. 4.12j inset) due to the diffraction at the interface of two SiGe structures of different thickness. When training the CNN model for disk position detection, we only used diffraction patterns simulated with single crystal Si model without considering diffuse scattering. We believe that by training the CNN using simulation from a more complicated and realistic atomic model will help to improve this method.

4.4. Discussions

The above results demonstrated two ANNs based approaches toward data mining of 4D electron diffraction datasets. Such datasets collected by SEND or 4D-STEM techniques provide spatially diffraction information that have revolutionized the characterization of materials microstructure, from the determination of nanodomains in ferroelectrics [37, 38] and molecular frameworks [39] to molecular crystal orientation mapping [22] and to the determination of nanoprecipitates in Al alloys [19]. In all of these applications, efficient and robust data mining techniques play a critical role. Thus, the capability of deep learning and recognizing complex patterns provided by ANNs have the potential to transform how we analyze electron diffraction data, including large 4D-DDs.

How to train ANNs for diffraction data, however, is less explored compared with other areas of electron microscopy. Here we focused on orientation and strain mapping using 4D-DD. In both cases, conventional techniques exist. Strain mapping based on disk position determination using the center of mass or CHT techniques does not require pre-computation, while training ANNs for strain mapping described here is based on simulated diffraction patterns. The advantage of using simulation is that the dynamical effects are taken into consideration. ANNs analysis uses the full intensity and diffraction geometry information, this improves the robustness of the method, and improves the precision in some cases as we demonstrated here.

For precision orientation mapping, both the commonly used pattern matching method and our ANN method require a precalculated database to perform the matching or training, as described in Section 4.2.5. Here, ANNs hold the advantage in improving the angular resolution by regression through interpolation in high dimensional space capability of ANNs.

A critical factor in training ANNs is to add appropriate noise to the training data. In orientation analysis because of the error that could be introduced by inelastic background for example, we found adding the noise at 15-30 dB level greatly improves the performance of trained ANNs. For strain mapping, the noise is directly added to the image as illustrated in Fig. 4.2. Here the noise mainly comes from the detector. Adding noise enables the trained ANNs to deal with real experimental data.

The simulation of training datasets and the training of ANNs do take significant amount of time, however, the computational time for applying ANN to the experimental patterns is not related to the size of the simulation library once the ANNs are trained. While for the pattern matching method, computational time is proportional to the simulation library size as each experimental pattern has to be compared with all simulated patterns. Thus, for large 4D-DDs, ANNs can significantly reduce the amount of processing time.

The example of GaSb precision orientation mapping described in Section 4.3.1 used Matlab with a 3.3GHz CPU. It takes 0.02 s to process 2,500 diffraction patterns in the SEND dataset using the ANN method, while it takes 500 s to finish pattern matching between 2,500 experimental patterns and 13,005 simulated patterns. In this case, the computational time for simulation library was the same for both methods, due to the fact that they shared the same library.

To fully take advantage of the high precision provided by the dynamical diffraction simulation, a new library needs to be generated every time when a different material, sample thickness or zone axis is used in an experiment. When the extra sensitivity is not needed, one can also use the kinematically simulated diffraction patterns as the training data for a broader range of sample thicknesses.

For strain mapping, the total processing time is improved by a factor of 4 using CNNs compared with CHT method. The strain precision is also improved as can be seen in Fig. 4.8 and Fig. 4.12. One drawback here is the amount of computational time for pre-computation, but once ANNs are trained, the same network can be applied repeatedly to datasets acquired with similar experimental conditions. We note that by training the ANNs with the dynamically simulated diffraction disks, they can automatically learn to focus on circular edges similar to the human designed CHT method. Therefore, if a large enough training dataset is built to take into account variations in the diffraction disks, it is possible to train a single set of CNNs capable of measuring strain from different datasets of different samples.

In choosing the right neural networks for our applications, we have kept the network design as simple as possible. This approach is based on the consideration that diffraction data are highly structured and thus the diversity of images is significantly lower than for example, random taken images from a heterogeneous TEM sample. We have used ANNs and CNNs here for our applications, Once the type of NNs is selected, the detailed choices for the NNs are the number of layers, number of neurons in each layer. In the convolutional NNs, the convolution is performed using eight 3×3 filters repeated two times and with 2×2 max pooling in between. The filter size can be increased here as well. Compared to image recognition where a large number of neurons are required, the number of neurons for diffraction analysis is modest. For example, in the CNN used for strain analysis, the total number of neurons is 800k and the training time on a desktop computer without GPU is only about 30 mins, which provides a real advantage for applications. For ANNs, one-hidden-layer structure with 30 neurons has 1,300 parameters. The training takes about 10 minutes using a desktop PC. Thus, the modest computational requirement for diffraction pattern analysis is another benefit for electron diffraction.

For future developments, we note the rapid developments in electron detector technology with faster frame acquisition, large dynamical range and improvement in detective quantum efficiency (DQE) using direct electron detection [40]. All of these improve the diffraction quality in term of signal noise ratio, as well as the type of diffraction patterns that can be collected, and crystals that can be studied. Thus, we expect the improvement in measurement precision and computational time using machine learning will play key enabling role for 4D-DD analysis.

4.5. Conclusions

We have provided two examples of machine learning assisted electron diffraction pattern analysis, and how such analysis is incorporated with scanning electron nanodiffraction. The first example is a simple artificial neural network designed to determine crystal orientation based on the integrated diffraction disk intensities instead of the whole pattern. We demonstrated that it is possible to achieve faster and more accurate determination of small orientation change in a GaSb thin sample compared with the traditional correlation-based pattern matching. The method is applied to characterize the misorientation of grain subdivision in a sample of irradiated UO_2. The results clearly show the spatial distribution of multiple small grains sharing low-angle grain boundaries less than 2° with each other. The second example is a convolutional neural network designed to measure diffraction disk position from the pattern. Since this method works on small sub-images, the network structure can be simplified to expedite both model training and processing of the experimental data. The application of the trained convolutional neural network to the measurement of strain fields in a FinFET device shows comparable results as previously calculated by the circular Hough transform method and has better precision in some cases. The training of all these neural networks is possible with accurate electron diffraction simulation using dynamical diffraction theory. Together, supervised machine learning based automated analysis of large 4D diffraction datasets can provide rich information about nanoscale crystalline materials with both high spatial resolution and high precision.

4.6. References

[1] C.J. Humphreys, STEM imaging of crystals and defects, in: J.J. Hren, J.I. Goldstein, D.C. Joy (Eds.) Introduction to analytical electron microscopy, Plenum, New York, 1979, pp. 305-332.

[2] J.M. Zuo, J.C.H. Spence, Advanced Transmission Electron Microscopy, Imaging and Diffraction in Nanoscience, Springer, New York, 2017.

[3] J.C.H. Spence, Chapter 77 Experimental studies of dislocation core defects, Dislocations in Solids, 13 (2007) 419-452.

[4] K. Urban, L. Houben, C.-L. Jia, M. Lentzen, S.-B. Mi, A. Thust, K. Tillmann, Chapter 11 Atomic-Resolution Aberration-Corrected Transmission Electron Microscopy, in: W.H. Peter (Ed.) Advances in Imaging and Electron Physics, Elsevier, 2008, pp. 439-480.

[5] S.-H. Kim, J. Lim, R. Sahu, O. Kasian, L.T. Stephenson, C. Scheu, B. Gault, Direct Imaging of Dopant and Impurity Distributions in 2D MoS2, Advanced Materials, 32 (2020) 1907235.

[6] M. Xu, A. Li, M. Gao, W. Zhou, Single-atom electron microscopy for energy-related nanomaterials, Journal of Materials Chemistry A, 8 (2020) 16142-16165.

[7] P.Y. Huang, S. Kurasch, J.S. Alden, A. Shekhawat, A.A. Alemi, P.L. McEuen, J.P. Sethna, U. Kaiser, D.A. Muller, Imaging Atomic Rearrangements in Two-Dimensional Silica Glass: Watching Silica’s Dance, Science, 342 (2013) 224.

[8] J.C.H. Spence, J.M. Zuo, Electron microdiffraction, Plenum Press, New York, 1992.

[9] K.W. Urban, Studying atomic structures by aberration-corrected transmission electron microscopy, Science, 321 (2008) 506-510.

[10] Y. LeCun, Y. Bengio, G. Hinton, Deep learning, Nature, 521 (2015) 436-444.

[11] M. Ziatdinov, O. Dyck, A. Maksov, X. Li, X. Sang, K. Xiao, R.R. Unocic, R. Vasudevan, S. Jesse, S.V. Kalinin, Deep learning of atomically resolved scanning transmission electron microscopy images: chemical identification and tracking local transformations, ACS Nano, 11 (2017) 12742-12752.

[12] J.A. Aguiar, M.L. Gong, R.R. Unocic, T. Tasdizen, B.D. Miller, Decoding crystallography from high-resolution electron imaging and diffraction datasets with deep learning, Science Advances, 5 (2019) eaaw1949.

[13] C.-H. Lee, A. Khan, D. Luo, T.P. Santos, C. Shi, B.E. Janicek, S. Kang, W. Zhu, N.A. Sobh, A. Schleife, B.K. Clark, P.Y. Huang, Deep Learning Enabled Strain Mapping of Single-Atom Defects in Two-Dimensional Transition Metal Dichalcogenides with Sub-Picometer Precision, Nano Letters, 20 (2020) 3369-3377.

[14] A. Voulodimos, N. Doulamis, A. Doulamis, E. Protopapadakis, Deep Learning for Computer Vision: A Brief Review, Computational Intelligence and Neuroscience, 2018 (2018) 7068349.

[15] K. Kaufmann, C.Y. Zhu, A.S. Rosengarten, D. Maryanovsky, T.J. Harrington, E. Marin, K.S. Vecchio, Crystal symmetry determination in electron diffraction using machine learning, Science, 367 (2020) 564-+.

[16] K. de Haan, Z.S. Ballard, Y. Rivenson, Y.C. Wu, A. Ozcan, Resolution enhancement in scanning electron microscopy using deep learning, Sci Rep-Uk, 9 (2019).

[17] O. Machek, T. Vystavêl, L. Strakos, P. Potocek, Training an artificial neural network using simulated specimen images, in, U.S. Patent Application, 2020.

[18] W. Xu, J.M. LeBeau, A deep convolutional neural network to analyze position averaged convergent beam electron diffraction patterns, Ultramicroscopy, 188 (2018) 59-69.

[19] J.K. Sunde, C.D. Marioara, A.T.J. van Helvoort, R. Holmestad, The evolution of precipitate crystal structures in an Al-Mg-Si(-Cu) alloy studied by a combined HAADF-STEM and SPED approach, Materials Characterization, 142 (2018) 458-469.

[20] B. Martineau, D.N. Johnstone, A.T.J. van Helvoort, P.A. Midgley, A.S. Eggeman, Unsupervised machine learning applied to scanning precession electron diffraction data, Adv Struct Chem Imag, 5 (2019).

[21] J.-M. Zuo, Electron Nanodiffraction, in: P.W. Hawkes, J.C.H. Spence (Eds.) Springer Handbook of Microscopy, Springer International Publishing, Cham, 2019, pp. 2-2.

[22] C. Ophus, Four-Dimensional Scanning Transmission Electron Microscopy (4D-STEM): From Scanning Nanodiffraction to Ptychography and Beyond, Microscopy and Microanalysis, 25 (2019) 563-582.

[23] E. Rauch, M. Véron, Improving angular resolution of the crystal orientation determined with spot diffraction patterns, Microscopy and Microanalysis, 16 (2010) 770-771.

[24] Y.F. Meng, J.M. Zuo, Improvements in electron diffraction pattern automatic indexing algorithms, Eur Phys J-Appl Phys, 80 (2017).

[25] R. Yuan, J. Zhang, J.-M. Zuo, Lattice strain mapping using circular Hough transform for electron diffraction disk detection, Ultramicroscopy, 207 (2019).

[26] J.-M. Zuo, J. Tao, Scanning electron nanodiffraction and diffraction imaging, in: Scanning Transmission Electron Microscopy, Springer, 2011, pp. 393-427.

[27] J.T. McKeown, J.C.H. Spence, The kinematic convergent-beam electron diffraction method for nanocrystal structure determination, J Appl Phys, 106 (2009).

[28] J.C.H. Spence, J.M. Zuo, Electron Microdiffraction, Plenum, New York, 1992.

[29] S. Herrmann, S. Li, M. Simpson, Electrolytic reduction of spent light water reactor fuel - Bench-scale experiment results, J Nucl Sci Technol, 44 (2007) 361-367.

[30] D.W. Marquardt, An Algorithm for Least-Squares Estimation of Nonlinear Parameters, J Soc Ind Appl Math, 11 (1963) 431-441.

[31] D.P. Kingma, J. Ba, Adam: A method for stochastic optimization, arXiv preprint arXiv:1412.6980, (2014).

[32] J.M. Zuo, A.B. Shah, H. Kim, Y.F. Meng, W.P. Gao, J.L. Rouviere, Lattice and strain analysis of atomic resolution Z-contrast images based on template matching, Ultramicroscopy, 136 (2014) 50-60.

[33] L. Delannay, O.V. Mishin, D.J. Jensen, P. Van Houtte, Quantitative analysis of grain subdivision in cold rolled aluminium, Acta Materialia, 49 (2001) 2441-2451.

[34] T. Yao, B. Gong, L. He, J. Harp, M. Tonks, J. Lian, Radiation-induced grain subdivision and bubble formation in U3Si2 at LWR temperature, Journal of Nuclear Materials, 498 (2018) 169-175.

[35] V.V. Rondinella, T. Wiss, The high burn-up structure in nuclear fuel, Mater Today, 13 (2010) 24-32.

[36] T.J. Gerczak, C.M. Parish, P.D. Edmondson, C.A. Baldwin, K.A. Terrani, Restructuring in high burnup UO2 studied using modern electron microscopy, Journal of Nuclear Materials, 509 (2018) 245-259.

[37] K.H. Kim, D.A. Payne, J.M. Zuo, Determination of 60 degrees polarization nanodomains in a relaxor-based ferroelectric single crystal, Applied Physics Letters, 107 (2015) 162902.

[38] Y.-T. Shao, J.-M. Zuo, Nanoscale symmetry fluctuations in ferroelectric barium titanate, BaTiO3, Acta Crystallographica Section B, 73 (2017) 708-714.

[39] D.N. Johnstone, F.C.N. Firth, C.P. Grey, P.A. Midgley, M.J. Cliffe, S.M. Collins, Direct Imaging of Correlated Defect Nanodomains in a Metal–Organic Framework, Journal of the American Chemical Society, 142 (2020) 13081-13089.

[40] G. McMullan, A.R. Faruqi, D. Clare, R. Henderson, Comparison of optimal performance at 300 keV of three direct electron detectors for use in low dose electron microscopy, Ultramicroscopy, 147 (2014) 156-163.

CHAPTER 5

IMAGING AND CHARACTERIZATION OF DEFECTS IN SILICON-GERMANIUM

In this Chapter, we focus on imaging and characterization of different types of defects in SiGe. Both Si and Ge have the diamond cubic structure with a 4% lattice mismatch between each other. When alloyed together, the lattice constant of SiGe can be tuned by the relative composition of Si and Ge, which provides a very useful route to better semiconductor devices through band engineering [1, 2]. SiGe is also a candidate for quantum qubits, which are the critical component for quantum computing [3, 4]. Due to the relatively large lattice mismatch, misfit dislocations and threading dislocations are inevitable in SiGe heterostructures. Extensive efforts have been made to control strain and reduce the threading dislocations using a combination of growth techniques and composition tuning. Here we investigate the defects in a compositionally graded SiGe heterostructure, in which there is a three layer step graded SiGe of 1.9 µm in thickness on top of the Si substrate, followed by a 2.65 µm relaxed SiGe layer and then a 17 nm strained Si nano layer. The detail of the sample is described elsewhere [5].

5.1. Microprobe STEM Imaging

High angle annular dark-field (HAADF) STEM imaging is one of popular techniques for the study of thin films. It works by collecting electrons scattered to high angle with a HAADF detector under the sample. The purpose of collecting only high angle scattering signals is that the coherent interference and diffraction contrast at low scattering angles can be reduced so that the contrast is mostly dependent on chemical composition of the material, giving rise to the so-called Z-contrast. When studying defects, however, the diffraction contrast at lower scattering angles is very useful. In 4D-STEM, virtual bright-field (VBF) or virtual annular dark-field (VADF) images can be generated by placing a virtual detector on the 4D-DDs acquired by SEND and integrate intensity within the detector. The image intensity at probe position $\vec{r}_p$ is

$$I(\vec{r}_p) = \int D(\vec{k}) I(\vec{k}, \vec{r}_p) d\vec{k}, \tag{5.1}$$

where $D(\vec{k})$ is the detector function, which equals 1 within the detector and 0 otherwise. $I(\vec{k}, \vec{r}_p)$ is the diffraction pattern taken at probe position $\vec{r}_p$. While VBF and VADF combined with SEND have been demonstrated useful to obtain diffraction contrast from the sample [6], the potential of using SEND for defect characterization is yet to be fully explored. A key step in SEND acquisition is to identify areas of interest. The SEND acquisition is slow, so it is important to get an overview of the scanning area before the long acquisition. The way to achieve this is to use the HAADF detector to acquire images under the same beam setting as in SEND. This is called microprobe STEM imaging as in the Thermo Fisher microscopes.

The collection angles have a large impact on the contrast observed in microprobe STEM. As shown in Fig. 5.1a, a typical Z-contrast HAADF image shows the composition variation in the sample. When convergence angle is decreased to 1.0 mrad, diffraction contrast becomes obvious in image which highlights the dislocations (Fig. 5.1b). When a different collection angle is chosen in Fig. 5.1c, additional different contrast shows up from strain fields near the defects, bend contour, and thickness fringes, which gives us more indicators about defects in the sample. We have found that microprobe STEM imaging under the conditions of beam convergence angle of 1 mrad and collection angle of 4-29 mrad can be very helpful in quickly locating the region of interest, providing the reference for sample drift correction during SEND acquisition, and double checking the sample condition and possible beam damage after the SEND experiment.

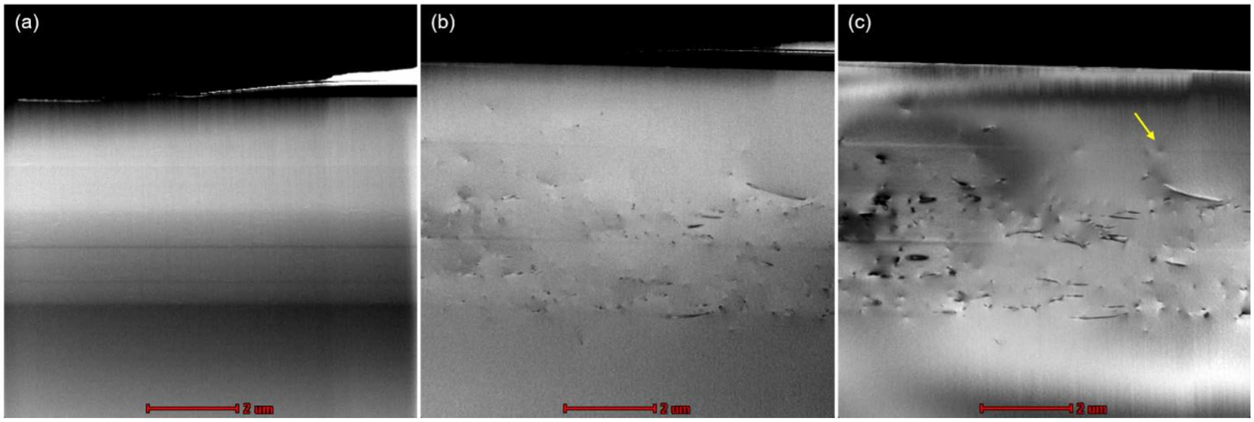

Fig. 5.1. ADF-STEM images of dislocations in a composition graded SiGe thin film with different imaging conditions. (a) Beam convergence angle: 25.1 mrad, collection angle: 79-200 mrad. (b) Convergence angle: 1.0 mrad, collection angle: 79-200 mrad. (c) Convergence angle: 1.0 mrad, collection angle: 4-29 mrad.

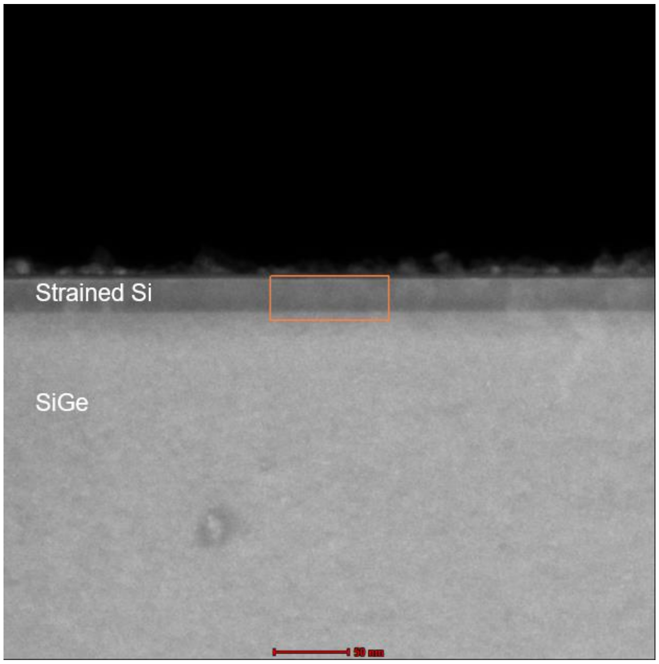

Fig. 5.2. Microprobe STEM imaging of the SiGe sample.

5.2. Lattice Strain Mapping

To characterize the complex strain fields in the composition graded SiGe thin-film, we collected multiple 4D-DDs. The first 4D-DD was acquired at the top strained Si layer where the Si lattice is biaxially strained with minimum number of dislocations. The scan area is marked by the orange box in Fig. 5.2. Fig. 5.3 shows the strain maps calculated from the 4D-DD by using the circular Hough transform method for diffraction disk detection. The reference for strain is taken from the Si substrate. Strain ϵ_{xx} || [110] is mostly uniform in the scan area, indicating that the Si layer is uniformly strained without the indication of dislocations in the scanned area. Strain ϵ_{yy} || [001] has an abrupt change at the interface between the strained Si layer and the SiGe layer due to the tetragonal distortion of epitaxial Si to accommodate the lattice parameter mismatch between the Si and SiGe substrate. The average strain in the strained Si layer is $\overline{\epsilon_{xx}} = 0.73 \pm 0.05\%$, and $\overline{\epsilon_{yy}} = -0.68 \pm 0.14\%$, with the previous reported value of $\overline{\epsilon_{xx}} = 0.90\%$ and $\overline{\epsilon_{yy}} = -0.54\%$ measured by X-ray diffraction reciprocal space mapping (XRD RSM) [5]. The reference used to calculate the strain was obtained from another scan in the Si substrate. The difference between the electron diffraction results and the reported XRD values could be due to the strain fluctuation in the strained Si layer and the possible error in strain relaxation from the cross-sectional TEM sample preparation.

Next, we focus on a misfit dislocation at the interface of two SiGe layers of different composition as indicated by the yellow arrow in Fig. 5.1c. To help with the interpretation of the SEND results, we also acquired an atomic resolution ADF-STEM image from the same region as shown in Fig. 5.5. The image reveals a stacking fault bounded by two 30° partial dislocations with Burgers vectors of $b_1 = 1/6[\bar{2}\bar{1}\bar{1}]$ and $b_2 = 1/6[211]$. A perfect dislocation b_3 with a Burgers vector of $1/2[\bar{1}0\bar{1}]$ is found near b_2. The b_2 and b_3 are separated by 3 atomic layers.

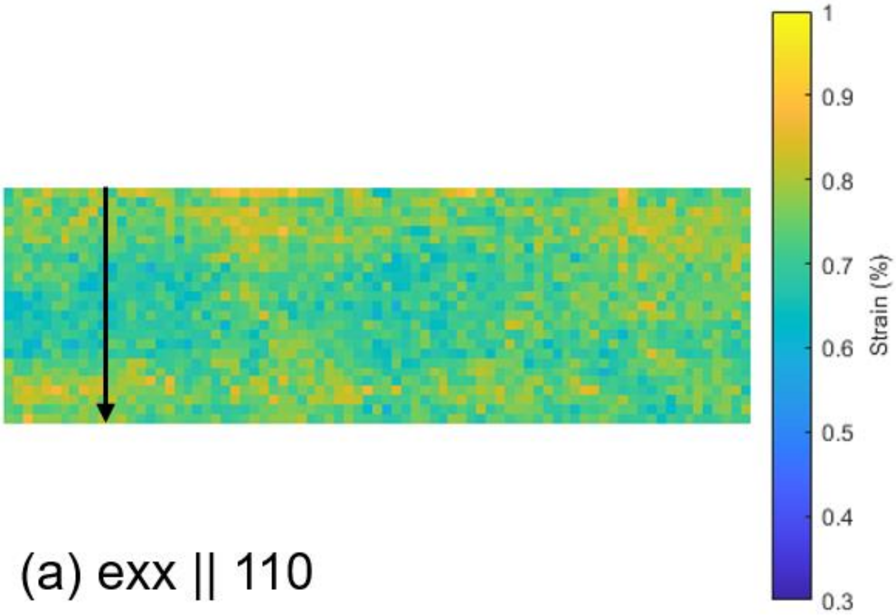

(a) exx || 110

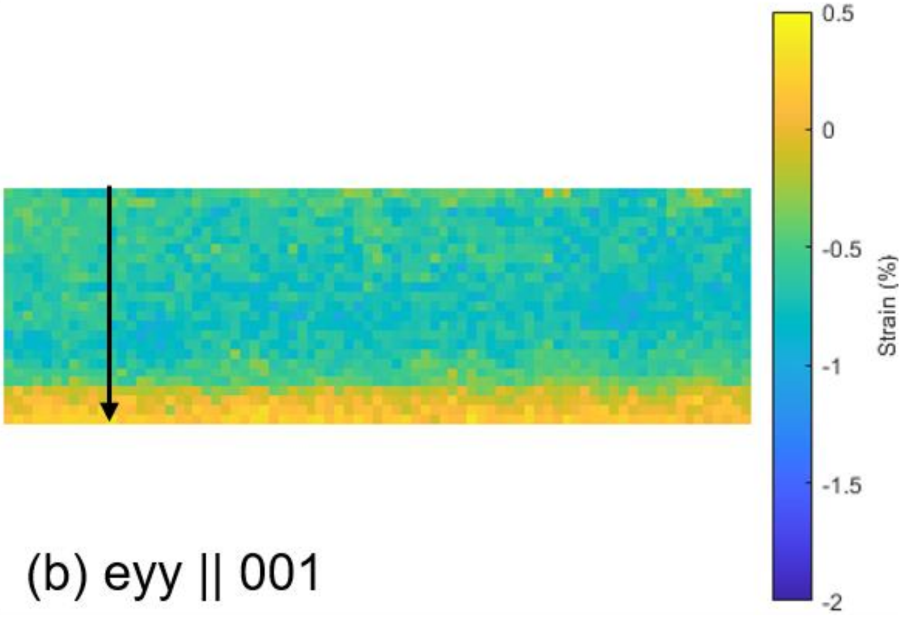

(b) eyy || 001

Fig. 5.3. Strain maps of the orange box in Fig. 5.2. (a) ϵ_{xx} and (b) ϵ_{yy} components of the strain.

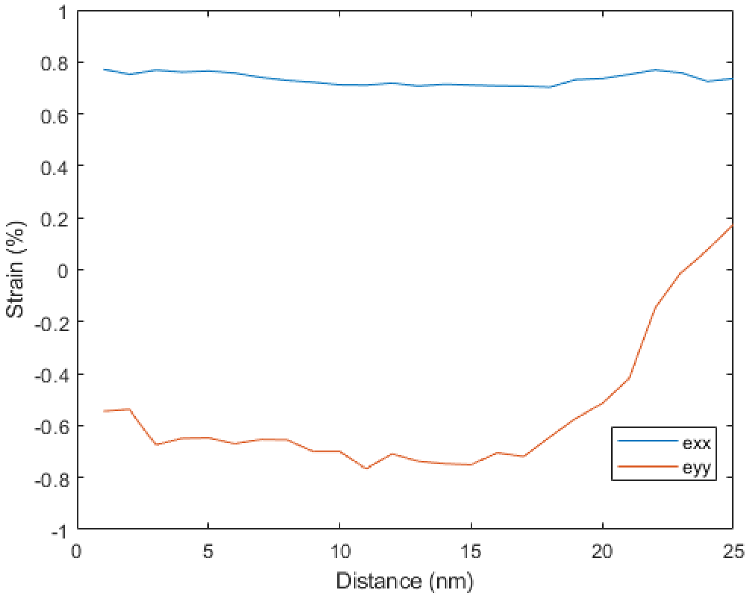

Fig. 5.4. Line profiles taken along the black arrows in Fig. 5.3.

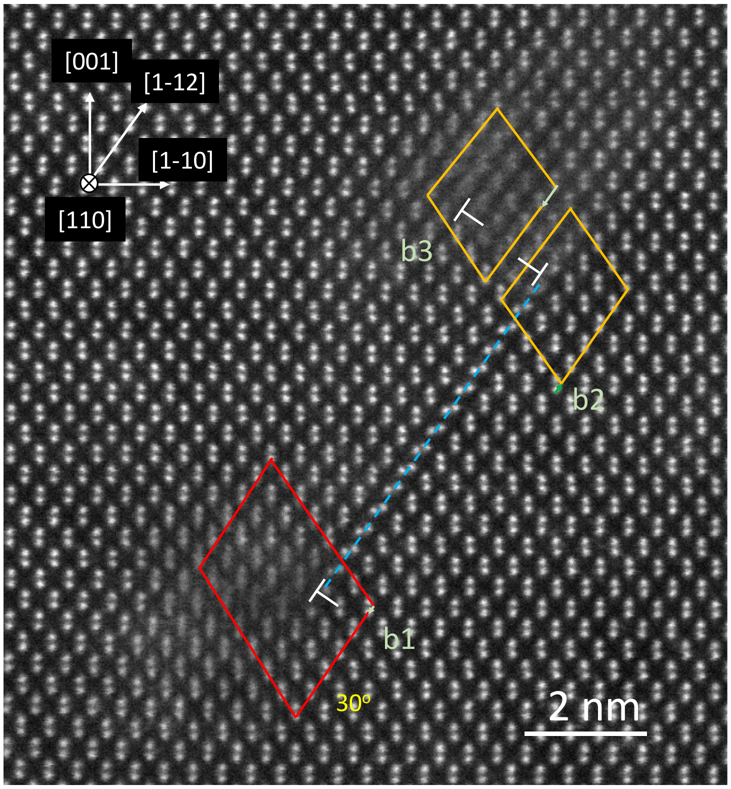

Fig. 5.5. Atomic resolution HAADF-STEM image of dislocations associated with a stacking fault.

A SEND experiment with a 40×40 scan was performed including the dislocation. The dislocation line is parallel to the electron beam. The step size is 1 nm with the probe size around 1.1 nm. Fig. 5.6a-d show strain maps along x ∥ [110] and y ∥ [001] calculated from the 4D-DD using the convolutional neural networks (CNN) for disk detection method introduced in Chapter 4. This technique is able to achieve both high accuracy and high precision. The measured strain fields feature dipole-like features in ϵ_{xx} and rotation components, while three-fold features in ϵ_{yy} and ϵ_{xy} are observed. To understand these features, the dislocation defect is modeled by three edge dislocations as denoted by b_1, b_2, and b_3 in Fig. 5.5. By superimposing the strain fields of the three dislocations calculated by elasticity theory [7] based on their Burgers vectors and applying a Gaussian blur to mimic the finite spatial resolution of SEND, we obtain the model strain maps in Fig. 5.6e-h. The close match between the experimental and model strain maps demonstrates the good precision, sensitivity, and resolution of our strain mapping technique near the dislocation cores. While atomic resolution STEM imaging can resolve structures close to the dislocation core, the relatively weak strain fields extended away from the core can only be resolved by methods with high enough precision as reported here.

Fig. 5.7 shows an estimation of the strain measurement errors based on the circular Hough transform introduced in Section 3.4.4. The error is estimated based on the uncertainty in peak fitting of the circular Hough transformed disk edges, which is higher when diffuse scattering blurs the disk edges. From Fig. 5.7, we can see large errors localized around the dislocation core where the lattice distortion is the most severe and diffuse scattering is the strongest. More quantitative analysis of the diffuse scattering in SEND datasets is done by Cepstral analysis in next section.

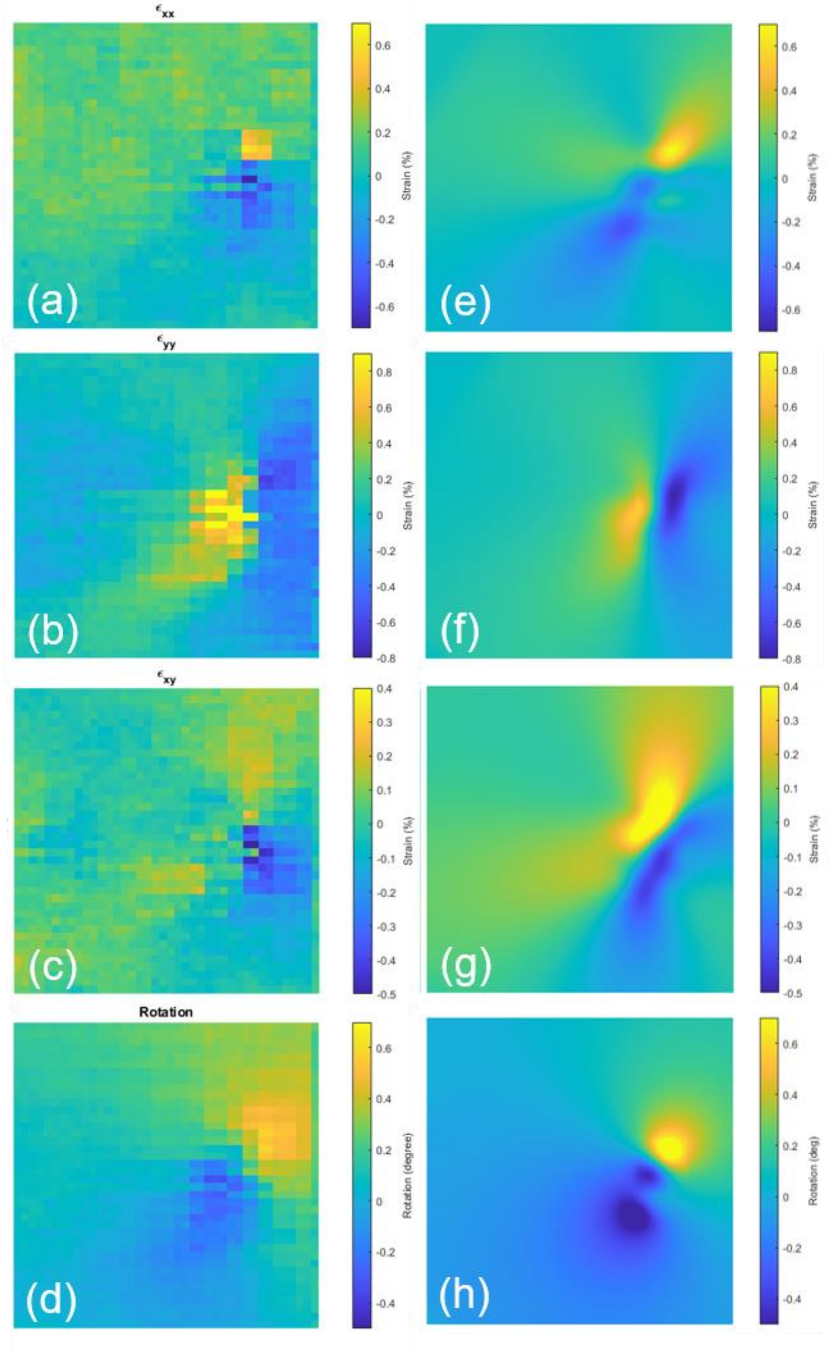

Fig. 5.6. Strain mapping of a complex defect in SiGe. (a-d) Strain maps ϵ_{xx}, ϵ_{yy}, ϵ_{xy}, and rotation calculated from the experimental 4D-DD. (e-h) Strain fields of dislocation cores calculated by elasticity theory. All images have the dimension of 40×40 nm^2.

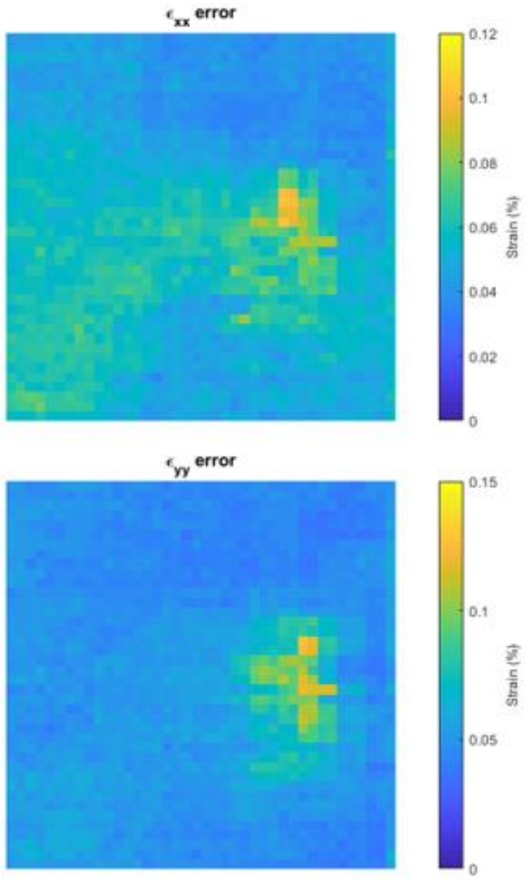

Fig. 5.7. Error maps of strain ϵ_{xx} and ϵ_{yy} estimated by error analysis of peak fitting in circular Hough transform.

5.3. Cepstral Analysis

5.3.1. Cepstral analysis of electron nanodiffraction patterns

Cepstral analysis is a sensitive signal processing technique for detecting weak harmonic signals, which was initially introduced for audio signal processing [8, 9]. When applied to electron diffraction patterns, cepstral analysis is capable of measuring small amount of lattice strains by reducing the crystal orientation induced diffraction artefacts [10]. For audio Cepstral processing, a time-dependent input signal is required, and a Fourier transform is performed to transform the temporal signal to frequency spectrum. Padgett et al. [10] recognized that by recording a diffraction pattern, the Fourier transform was performed by the objective lens directly, and thus, a Cepstral pattern, C_p, is obtained exactly and more efficiently using

$$C_p = \left|FT\{log[I(\vec{k})]\}\right|, \tag{5.2}$$

where $\vec{k}$ is the electron wave vector, I stands for diffraction intensity and FT for Fourier transform. Fig. 5.8a shows an example nanodiffraction pattern from a silicon sample along [110], and the calculated C_p (Fig. 5.8b). Since diffraction pattern is formed in the reciprocal space, the Cepstral peaks (Fig. 5.8b) detect the harmonic signals in the real space in the unit of distances (Å), with zero distance at the center of the Cepstral pattern. The Cepstral intensity decreases as the distances increase. The damping is caused by the electron probe shape, which limits the sample diffraction volume and thus the largest measurable interatomic distances. Fig. 5.8c and d explain the distances recorded in C_p. The smaller distance between two silicon atoms in a dumbbell is not resolved here, since the nanodiffraction pattern recorded here is dynamical. As a result of multiple scattering, the intensity of (002) is stronger than that of (004), while the weak (002) is needed for resolving the dumbbells. The dumbbells can be resolved for thin samples using kinematical CBED, for example [11].

To extend Cepstral analysis for electron diffuse scattering analysis, we take advantage of the averaged and local structural information captured in a 4D-DD, by calculating the difference between the Cepstral transforms of a local nanodiffraction pattern and the region averaged nanodiffraction pattern. In what follows, we show how the resulting difference Cepstrum (dC_p) approximately corresponds to the autocorrelation function, or Patterson function (PF) [12], of the distortive part of scattering potential in a thin sample. The dC_p is calculated according to

$$dC_p = \left|FT\left\{log\left[\frac{I(\vec{k})}{I_{avg}(\vec{k})}\right]\right\}\right| = \left|FT\{log[I(\vec{k})]\} - FT\{log[I_{avg}(\vec{k})]\}\right|, \tag{5.3}$$

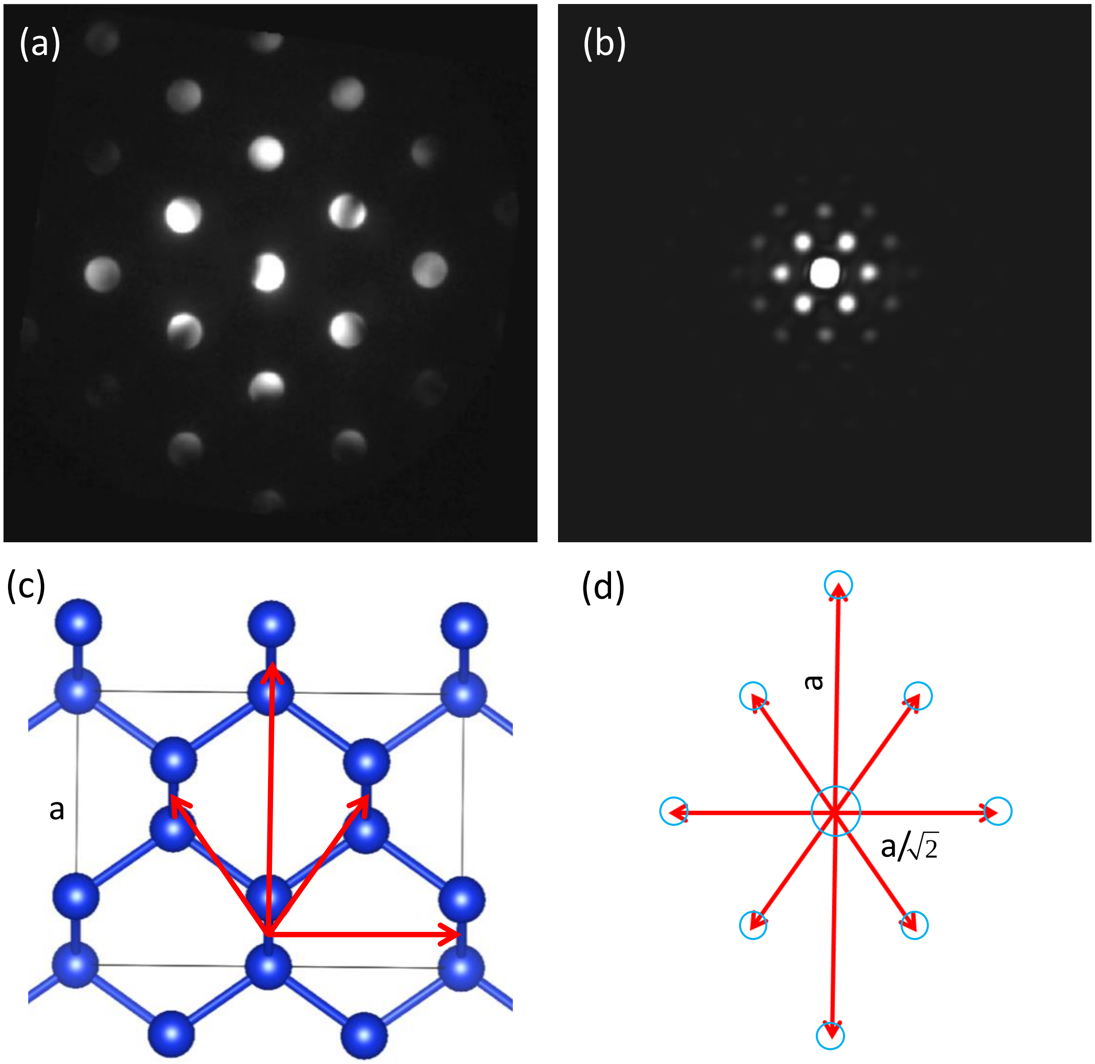

Fig. 5.8. Cepstral transform of electron nanodiffraction pattern. (a) Experimental diffraction pattern from a SiGe sample along [110], (b) Cepstral pattern from (a), (c) a model of silicon diamond structure projected along [110] with marked inter-dumbbell vectors, and (d) Inter-dumbbell vectors correspond to peaks in (b).

where $I_{avg}(\vec{k})$ represents intensity in the area averaged pattern, while $I(\vec{k})$ is the intensity in a single pattern from the 4D-DD. The interpretation of dC_p can be made based on the separation of the fluctuating part of the scattering potential (U_1) from the average scattering potential (U_{avg}). The scattering potential seen by a small coherent electron probe is a sum of these two:

$$U = U_{avg} + U_1, \tag{5.4}$$

where U_1 varies with the electron probe position. The U_{avg} represents an average over the region scanned by the electron probe, which for a randomly disordered crystal describes the periodic scattering potential. Diffraction by U gives the diffraction pattern $I(\vec{k})$, while diffraction by U_{avg} gives $I_{avg}(\vec{k})$. If we assume the fluctuations are random, then $\langle U_1 \rangle = 0$.

The distortive part of scattering potential is the origin of diffuse scattering, which is seen in between Bragg reflections. In electron diffraction, diffuse scattering is often observed using selected area electron diffraction [13, 14]. In a nanodiffraction pattern obtained using a coherent electron beam, the diffuse scattering is more like laser speckles, in a way similar to fluctuations recorded in amorphous materials [15]. The speckle pattern is averaged over the illuminated volume, which is proportional to the sample thickness. The diffraction pattern $I(\vec{k})$ thus has two parts under the approximations that electron diffuse scattering $I_D(\vec{k})$ is weak and the wave function associated with diffuse scattering has a random phase [16, 17]

$$I(\vec{k}) = I_{avg}(\vec{k}) + \bar{I}_{avg}(\vec{k}) * I_D(\vec{k}), \tag{5.5}$$

where $\bar{I}_{avg}(\vec{k})$ is the thickness averaged diffraction intensity. The convolution and thickness averaging reflect that there are many beams in $I_{avg}(\vec{k})$, each contributes to the total electron diffuse scattering throughout the entire sample thickness [16, 17]. Using

$$log\left[I\left(\vec{k}\right)\right] \approx \; log\left[I_{avg}\left(\vec{k}\right)\right] + \Lambda\left(\vec{k}\right) * I_D\left(\vec{k}\right), \tag{5.6}$$

where $\Lambda\left(\vec{k}\right) = \bar{I}_{avg}\left(\vec{k}\right)/I_{avg}\left(\vec{k}\right)$. FT of $\Lambda\left(\vec{k}\right) * I_D\left(\vec{k}\right)$ then gives

$$\left|FT\left[\Lambda\left(\vec{k}\right)\right]FT\left[I_D\left(\vec{k}\right)\right]\right| = \left|FT\left\{log\left[\frac{I\left(\vec{k}\right)}{I_{avg}\left(\vec{k}\right)}\right]\right\}\right| = dC_p. \tag{5.7}$$

Thus dC_p gives the Patterson function of the fluctuating scattering potential multiplied by a shape function. This shape function is approximately the FT of a top-hat function in a diffraction pattern where the transmitted beam is much stronger than the diffracted beams. We note that the dC_p differs from the Cepstral transform of the whole diffraction pattern, which does not give the Patterson function (for details, see Appendix of Ref. [10]).

The sensitivity of dC_p to the distortive part of potential is demonstrated in Fig. 5.9, where two examples are selected from a SiGe sample with Fig. 5.9a away from and Fig. 5.9c at a dislocation. The patterns are shown at the same intensity scale for comparison. Strong speckles are observed in Fig. 5.9c, while Fig. 5.9a is more like an electron diffraction pattern with diffuse scattering. The dC_p shown in Fig. 5.9b is weak with no strong harmonic signals. Compared with Fig. 5.9b, Fig. 5.9d shows strong harmonic peaks in the direction normal to the streaky speckles observed in Fig. 5.9c. Thus, both the intensity and harmonic peaks are sensitive to the amount and type of electron diffuse scattering.

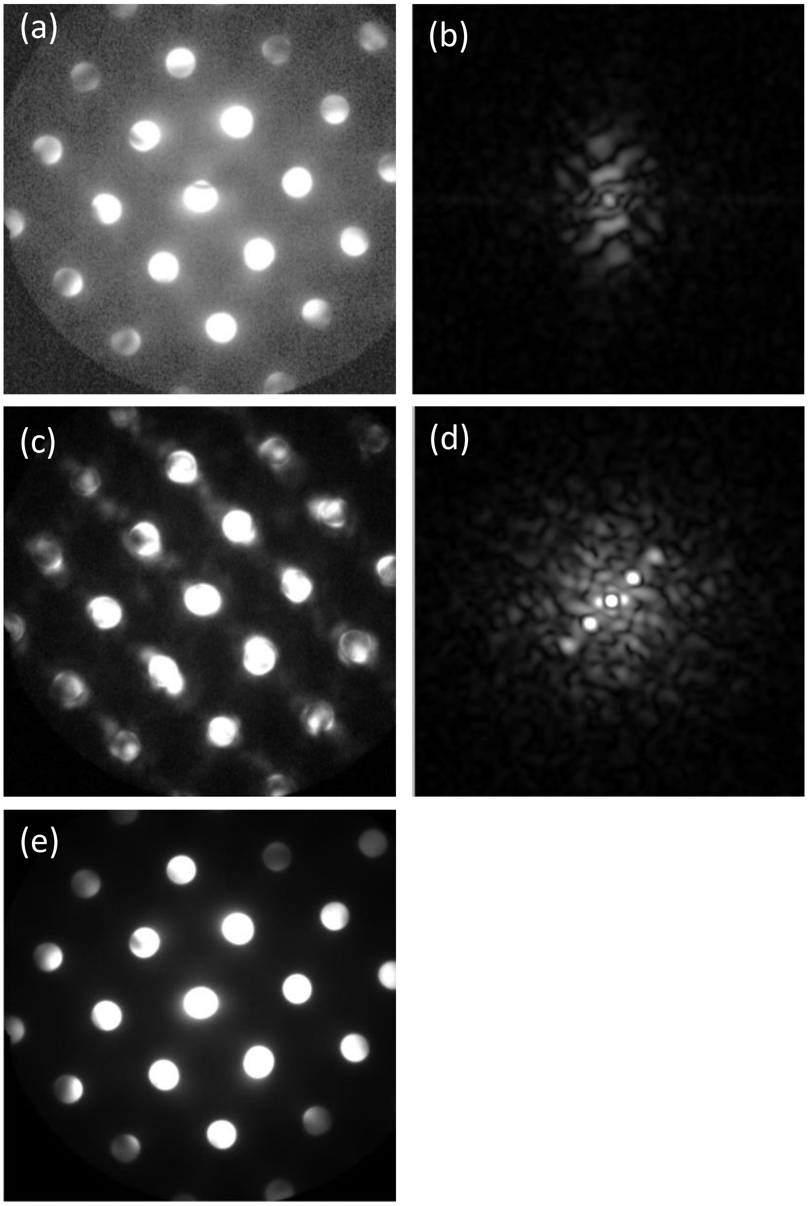

Fig. 5.9. Two examples of dC_p from a SiGe sample. (a) An electron nanodiffraction pattern taken away from dislocations along [110]. (b) dC_p of (a). (c) An electron nanodiffraction pattern at a dislocation core, (d) dC_p of (c). (e) The average pattern from a 40x40 4D-DD, which is used for the calculation of dC_p. For comparison, (a), (c) and (e) are displayed at the scale of 0-500 a.u. and (b) and (d) at the scale of 0-6500 a.u.

5.3.2. Cepstral STEM

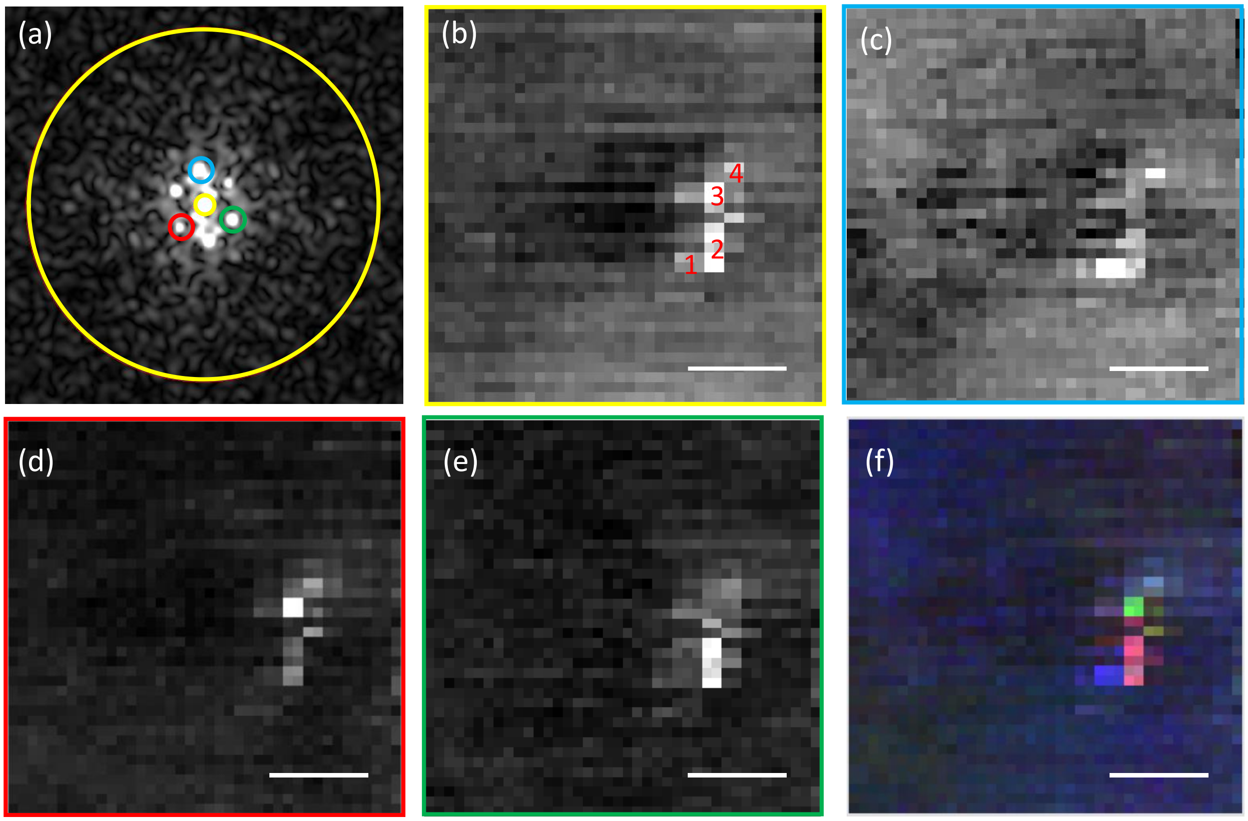

Fig. 5.10. Cepstral STEM imaging of a dislocation core. (a) 4D Cepstral data where intensity within the marked circles is integrated to form Cepstral ADF image of (b). (c) DF image formed with intensities within the blue circle, (d) and (e) within the red and green circles, respectively. (f) The RGB image formed using (c), (d) and (e). The 4D-DD was acquired from a SiGe sample with edge-on dislocations over the area of 40x40 nm^2. The scale bar is 10 nm.

The advantage of having 4D-DDs is that electron diffraction intensity can be analyzed and related to the structure of samples [18, 19] or the electric and magnetic fields for imaging [20, 21]. As the speed of detectors improves dramatically, 4D-DDs can be collected over larger areas than previously possible [22], which makes 4D-STEM more attractive than direct STEM imaging for some applications [23]. The examples of structural analysis include orientation [24, 25], domain [26] and strain mapping [18]. In all these cases, the diffraction signals from Bragg diffraction are analyzed in the reciprocal space and mapped in the real space. The Cepstral analysis method for strain mapping introduced by Padgett et al. [10] measures distances directly in the real space but again relies on Bragg diffraction. The idea of Cepstral STEM is thus to take advantage of electron diffuse scattering for imaging fluctuations in electron scattering potential.

Fig. 5.10 demonstrates an example of Cepstral STEM imaging of edge-on dislocations in a SiGe sample, which was grown on top of a silicon substrate. Because of the lattice mismatch strain, the sample contains both misfit and threading dislocations [5]. A 4D-DD was collected from a location with the edge-on misfit dislocations. The scan is over an area of 40x40 nm^2 with the step size of 1 nm. Fig. 5.10a represents a dC_p pattern obtained from the 4D-DD using the methods described in Fig. 5.9 and Eq. 5.7. A Cepstral ADF image (Fig. 5.10b) is obtained by integrating the dC_p intensity between two cutoff distances (the two marked circles in Fig. 5.10a). The same principle can also be used to form bright- or dark-field (BF and DF) images, using the zero-distance peak intensity or the intensity of a specific distance. Fig. 5.10c, d and e show three Cepstral DF images obtained by integrating three different Cepstral peaks marked in Fig. 5.10a. The contrast in Fig. 5.10b represents the magnitude of the distortive potential, which shows high contrast at the dislocation core region. Fig. 5.10c, d and e give different contrast, the strong contrast in each figure is associated with the regions where a particular Cepstral peak is strong. Putting them together, the composite image of Fig. 5.10f demonstrates the magnitude as well as the harmonics in the distortive potential at the dislocation core.

5.3.3. Cepstral STEM imaging of dislocation core in SiGe

Here we demonstrate the principle using Cepstral STEM for studying the core structure of the misfit dislocation observed in Fig. 5.5. Fig. 5.11 shows the distinctive dC_p patterns obtained from four areas of the dislocation core in SiGe, as marked in Fig. 5.10b. The areas are approximately located in the atomic resolution image of Fig. 5.5 and selected for comparison here. In Area 2, the dC_p peaks correspond to the inter-dumbbell distances along $[1\bar{1}2]$, where the change in the dumbbell direction in the stacking fault introduces a one-dimensional distortive potential in 2D projection. Interestingly, the dC_p pattern is insensitive to the relative shift between the two lattices across the stacking fault. This insensitivity can be attributed to the lack of interference signals in the recorded diffraction patterns, which presumably is weak for the non-overlapping diffraction disks in nanodiffraction. In Area 3, the dC_p peaks can be associated with the edge dislocation with the missing half plane along $[\bar{1}12]$ and distortions around the dislocation as marked by yellow and red lines, respectively. The dC_p pattern in Area 4 is characterized by the reduced second order peaks along $[\bar{1}12]$ and enhanced peaks along $[1\bar{1}0]$. The strong first order peaks indicate distortions that are not immediately obvious in the atomic resolution image as in Areas 2 and 3. In Area 1, two first order peaks are observed in the dC_p pattern along $[1\bar{1}0]$, which can be attributed to atomic distortions behind the smearing of dumbbell contrast along the line indicated by the arrow. These results indicate the sensitivity of Cepstral STEM to lattice distortion.

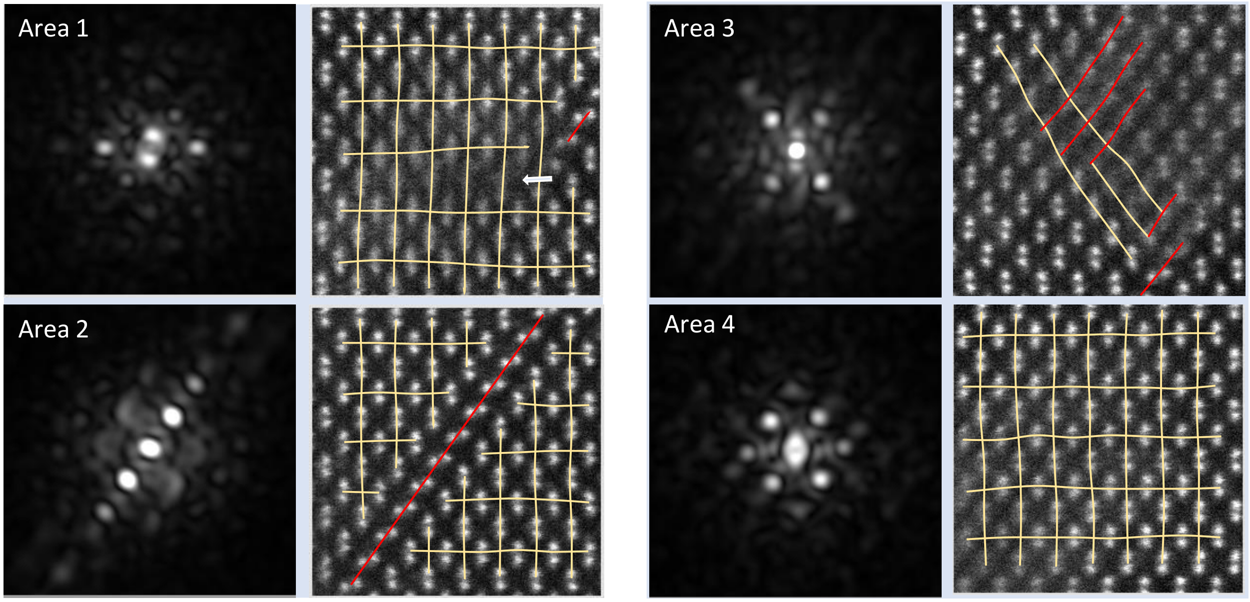

Fig. 5.11. Differential Cepstral patterns from 4 areas of dislocation core in SiGe and comparison with corresponding atomic resolution HAADF-STEM images taken from approximately the same areas.

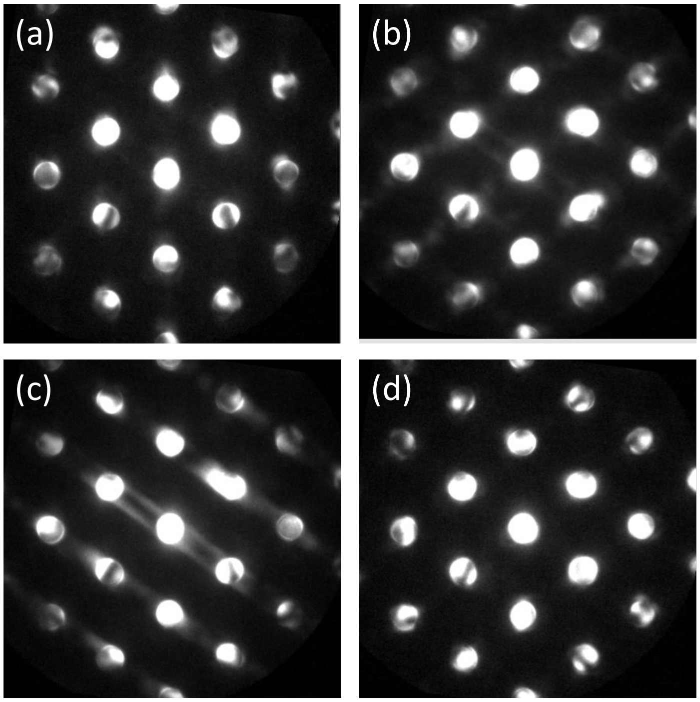

Fig. 5.12. Electron nanodiffraction patterns obtained from (a) Area 1, (b) Area 3, (c) Area 2 and (d) Area 4 of Fig. 5.10b.

A major utility of Cepstral STEM is to identify and extract electron nanodiffraction patterns from the severely distorted regions from the 4D-DD. Fig. 5.12 shows the diffraction patterns from four areas identified in Fig. 5.10b and Fig. 5.11, where strong diffraction streaks in Fig. 5.12 come from the stacking fault. Such diffraction patterns, in the future, can be combined with electron images to extract quantitative structural information about the dislocation core [27].

5.4. Defect Classification Using Deep Learning

The above results (Fig. 5.11 and Fig. 5.12) demonstrate that diffuse scattering is a strong indicator of local lattice distortion, as well as the type of distortion. Different types of defects create different diffuse scattering patterns, which can be captured by electron nanodiffraction. On the other hand, machine learning (ML) has been proven useful for pattern recognition [28]. For electron diffraction, ML is able to find complicated connections between information carried by Bragg diffraction and features in 4D-DDs (Chapter 4). In this section, we explore the possibility of using deep learning to automatically differentiate different types of defects based on diffuse scattering.

Toward the above goal, we first built a convolutional neural network (CNN) to learn from Cepstral STEM imaging and to determine if there is a defect based on the detected diffuse scattering in electron nanodiffraction patterns. The model is illustrated in Fig. 5.13. The input of the network is a 256×256-pixel diffraction pattern. There are 3 convolutional layers in the network to extract different levels of feature from a diffraction pattern. The number of layers was determined by the complexity of the network needed to differentiate diffuse scattering with high accuracy through a trial and error process. The output of the network is a prediction of the probability of the diffraction pattern having defects in the illuminated crystal volume.

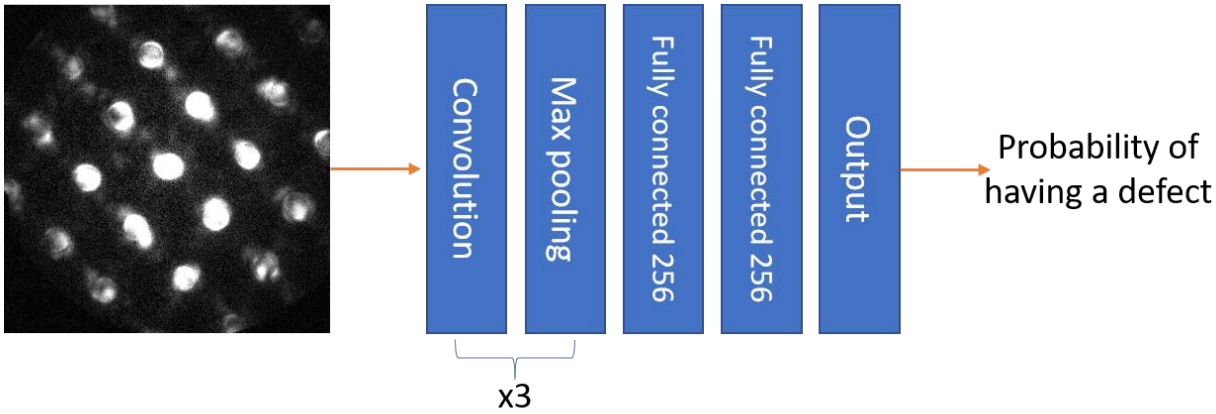

Fig. 5.13. Convolutional neural networks for defect detection from electron nanodiffraction. Input is a 256×256-pixel diffraction pattern. Output is the probability of having a defect.

To train this model, we acquired a line scan of SEND across the compositionally graded SiGe sample with 3000 diffraction patterns at a step size of 2 nm, which covers a large sample area with composition variation, strain, sample bending, as well as a number of obvious defects as can be seen in the microprobe STEM imaging in Fig. 5.14c. Cepstral ADF intensities for all diffraction patterns in the line scan are calculated following the procedures in Section 5.3 and plotted as a line profile in Fig. 5.14a with intensity value normalized to 0~1. As marked by red dashed lines in Fig. 5.14, sharp peaks in Cepstral ADF imaging as a result of strong diffuse scattering match with the locations where horizontal dislocations pass through the scanning line, while the relative intensity in Cepstral ADF imaging reflects relative crystallinity in the sample. Therefore, we simply define the normalized Cepstral ADF intensity as the probability of having defects in the illuminated crystal volume where the diffraction pattern is acquired and the label of the 3000 diffraction patterns used for CNN training.

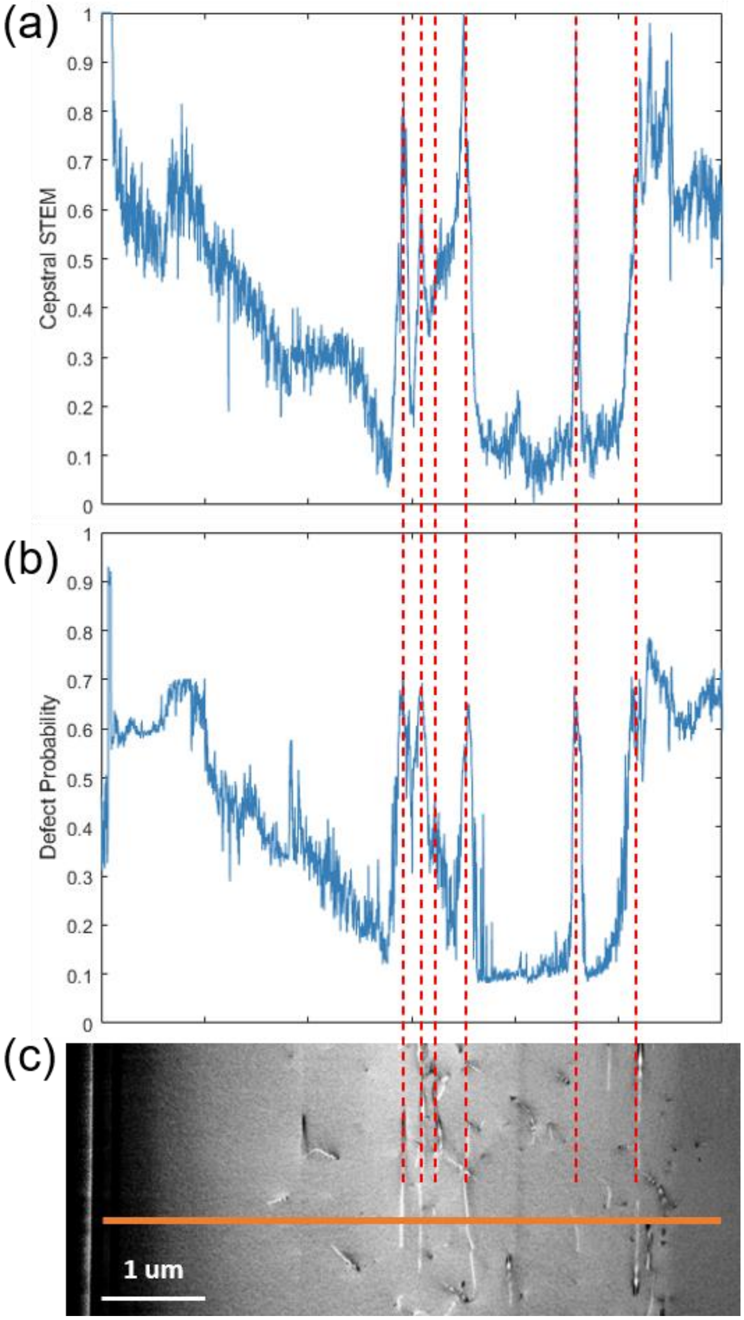

Fig. 5.14. Defect classification of a line scan SEND from the graded SiGe heterostructure. (a) Normalized Cepstral ADF intensities along the line scan. (b) Probability of having a defect predicted by the trained CNN. (c) Microprobe STEM imaging of the sample with the orange solid line marks the line scan position. Red dashed lines indicate positions of horizontal dislocations observed in the microprobe STEM image.

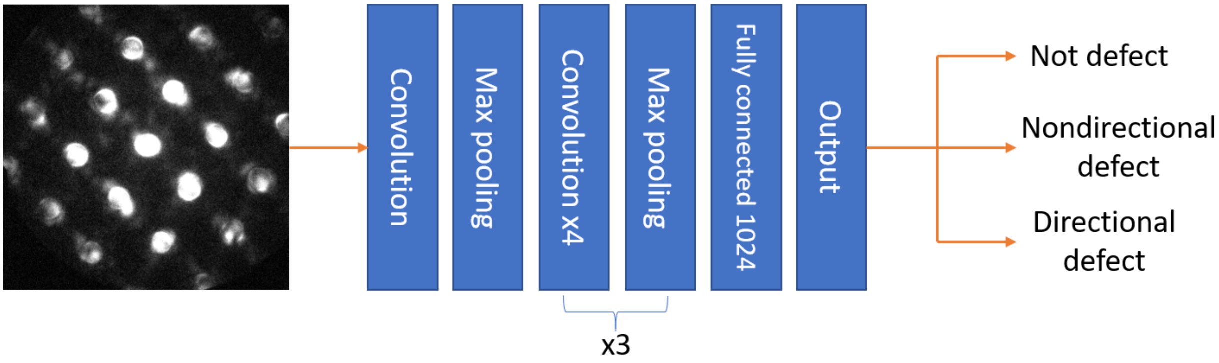

Fig. 5.15. Convolutional neural networks for defect type classification. Input is a 256×256-pixel diffraction pattern. Output is the probability of being one of the three types of defects.

The trained CNN is then applied to the same dataset used to calculate Cepstral ADF intensity. The predicted probability of having a defect is plotted in Fig. 5.14b. By comparing with the profile in Fig. 5.14a, we can see that the CNN successfully learned to mimic how Cepstral ADF works by focusing on diffuse scattering without pre-excluding Bragg diffraction as in the differential Cepstrum calculation (Section 5.3.1).

To extend the capability of defect classification with CNN, we next define three types of END patterns (Fig. 5.12). Fig. 5.12c (Area 2) exemplifies strong directional diffuse scattering which is the result of directional defects such as stacking fault as shown in Fig. 5.11. This type of diffraction pattern is classified as 'directional defect'. Diffuse scattering from Area 1 (Fig. 5.12a) does not show strong directional feature as the edge dislocation is observed edge-on, so in projection it seems nondirectional. We call this type of defect the 'nondirectional defect'. Finally, diffraction pattern with no obvious diffuse scattering (Fig. 5.12d) is classified as 'not defect'.

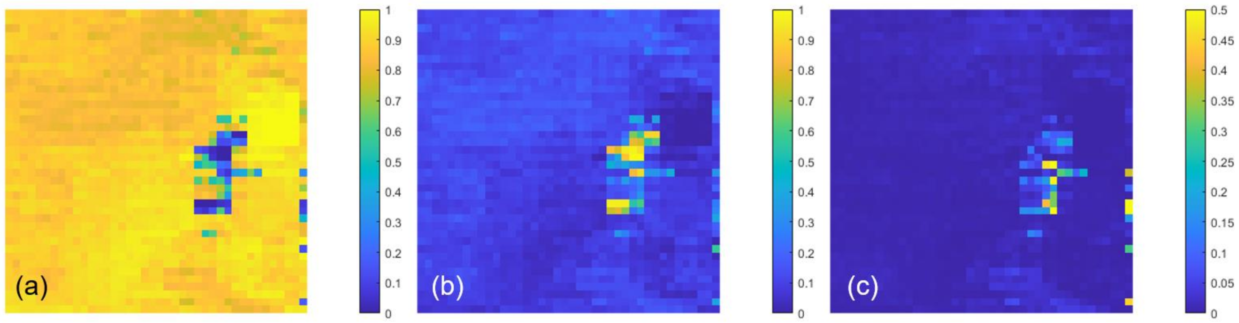

Fig. 5.16. Defect classification maps of dislocation cores and stacking fault in SiGe predicted by the trained CNN model. Probability of being (a) not defect, (b) nondirectional defects, or (c) directional defects.

To automatically classify END patterns into the three categories defined above, we expanded the CNN to include 13 convolutional layers as needed to detect different features in diffuse scattering for accurate classification (Fig. 5.15). Same as the previous network, the input is a 256×256-pixel diffraction pattern. The output of the network is now a prediction of the diffraction pattern as three possible types of defects, not defect, nondirectional defect, or directional defect, in probability. The training data for the CNN are selected from the 4D-DD taken from the complex defect in SiGe using the Cepstral STEM imaging in Fig. 5.10 as reference. 30 diffraction patterns are chosen for not defect, 18 for nondirectional defect, and 12 for directional defect. To avoid overfitting of the model, we selected another 4 patterns for not defect, 2 for nondirectional defect, and 2 for directional defect as test data. Data augmentation is applied to expand the limited number of the training patterns used. Random rotation and zoom are applied to each diffraction pattern to take into account of the effect of strain. Random shift and shear are applied to mimic the effects of misalignment of the microscope and lens distortion.

After training, the CNN model is applied to all 1600 diffraction patterns in the 4D-DD to generate defect classification maps in Fig. 5.16. When compared with the atomic resolution STEM image in Fig. 5.5 and Cepstral STEM images in Fig. 5.10, the trained CNN model successfully classified diffraction patterns from edge-on dislocations as nondirectional defects, diffraction patterns from the stacking fault as directional defects, and not defect elsewhere. The results mean that the CNN has automatically learned from the training data the features to differentiate these three types of diffuse scattering in a diffraction pattern.

5.5. Conclusions

In this chapter, we explored a number of different ways to study crystalline defects at nanoscale and used a compositionally graded SiGe thin film as an example. Microprobe STEM imaging was used as a very convenient technique to provide an overview of the sample and quickly locate defects for further investigation. Strain measurement techniques described in previous chapters have been applied to the SiGe sample to obtain strain maps from both uniformly strained regions and a highly distorted dislocation core region. By comparing with the theoretical model, we demonstrated that our CNN method for diffraction disk measurement helps to achieve high strain sensitivity to resolve long range strain fields around the dislocation cores that can not be easily observed by other techniques.

While Bragg diffraction reflects the average crystal lattice under the electron beam, diffuse scattering gives information about lattice distortion within the small volume of the sample being illuminated. By estimating the diffraction disk measurement error due to the disk edge blurring by diffuse scattering, we can qualitatively characterize the crystallinity distribution in the sample. For more quantitative analysis, we proposed Cepstral analysis to image severe lattice distortion based on diffuse scattering only by excluding the effect of Bragg diffraction during the calculation of differential Cepstrum. Combining the ideas of virtual annular dark-field imaging and Cepstrum, we demonstrated that Cepstral STEM imaging is very powerful to quantify crystallinity and visualize lattice distortions along certain directions by carefully setting up the virtual detectors. To automate and speed up this process for large 4D-DDs, we further developed deep learning based methods to analyze the diffraction patterns with minimal preprocessing of the data needed. By training with the data labeled with the help of Cepstral STEM, the CNNs can learn to focus on diffuse scattering to predict the probability of having a defect and classify the type of the defect. These methods provide fascinating new ways to analyze crystalline defects at nanoscale which may lead to new discoveries or better understanding of defects in crystals in the future.

5.6. References

[1] P.M. Mooney, Strain relaxation and dislocations in SiGe/Si structures, Mat Sci Eng R, 17 (1996) 105-146.

[2] M. Chu, Y.K. Sun, U. Aghoram, S.E. Thompson, Strain: A Solution for Higher Carrier Mobility in Nanoscale MOSFETs, Annu Rev Mater Res, 39 (2009) 203-229.

[3] M.A. Eriksson, M. Friesen, S.N. Coppersmith, R. Joynt, L.J. Klein, K. Slinker, C. Tahan, P.M. Mooney, J.O. Chu, S.J. Koester, Spin-based Quantum Dot Quantum Computing in Silicon, Quantum Inf Process, 3 (2004) 133-146.

[4] F.A. Zwanenburg, A.S. Dzurak, A. Morello, M.Y. Simmons, L.C.L. Hollenberg, G. Klimeck, S. Rogge, S.N. Coppersmith, M.A. Eriksson, Silicon quantum electronics, Rev Mod Phys, 85 (2013) 961-1019.

[5] X. Chen, D. Zuo, S. Kim, J. Mabon, M. Sardela, J. Wen, J.-M. Zuo, Large Area and Depth-Profiling Dislocation Imaging and Strain Analysis in Si/SiGe/Si Heterostructures, Microscopy and Microanalysis, 20 (2014) 1521-1527.

[6] K.H. Kim, H. Xing, J.M. Zuo, P. Zhang, H.F. Wang, TEM based high resolution and low-dose scanning electron nanodiffraction technique for nanostructure imaging and analysis, Micron, 71 (2015) 39-45.

[7] J.P. Hirth, J. Lothe, Theory of dislocations, 2nd ed., Krieger Pub. Co., Malabar, FL, 1992.

[8] A.M. Noll, Cepstrum Pitch Determination, The Journal of the Acoustical Society of America, 41 (1967) 293-309.

[9] A.V. Oppenheim, R.W. Schafer, From frequency to quefrency: a history of the cepstrum, IEEE Signal Processing Magazine, 21 (2004) 95-106.

[10] E. Padgett, M.E. Holtz, P. Cueva, Y.T. Shao, E. Langenberg, D.G. Schlom, D.A. Muller, The exit -wave power-cepstrum transform for scanning nanobeam electron diffraction: robust strain mapping at subnanometer resolution and subpicometer precision, Ultramicroscopy, 214 (2020).

[11] J.T. McKeown, J.C.H. Spence, The kinematic convergent-beam electron diffraction method for nanocrystal structure determination, Journal of Applied Physics, 106 (2009) 074309.

[12] A.L. Patterson, A Fourier Series Method for the Determination of the Components of Interatomic Distances in Crystals, Physical Review, 46 (1934) 372-376.

[13] J.M. Zuo, J. Pacaud, R. Hoier, J.C.H. Spence, Experimental measurement of electron diffuse scattering in magnetite using energy-filter and imaging plates, Micron, 31 (2000) 527-532.

[14] T.R. Welberry, Diffuse Scattering and Models of Disorder, Int. Union of Crystallography, Oxford University Press, 2010.

[15] P. Voyles, J. Hwang, Fluctuation Electron Microscopy, in: Characterization of Materials, John Wiley & Sons, Inc., 2002.

[16] J. Gjonnes, D. Watanabe, Dynamical diffuse scattering from magnesium oxide single crystals, Acta Crystallographica, 21 (1966) 297-302.

[17] J.M. Zuo, J.C.H. Spence, Advanced Transmission Electron Microscopy, Imaging and Diffraction in Nanoscience, Springer, New York, 2017.

[18] R. Yuan, J. Zhang, J.-M. Zuo, Lattice strain mapping using circular Hough transform for electron diffraction disk detection, Ultramicroscopy, 207 (2019) 112837.

[19] Y.T. Shao, J.M. Zuo, Lattice-Rotation Vortex at the Charged Monoclinic Domain Boundary in a Relaxor Ferroelectric Crystal, Physical Review Letters, 118 (2017) 157601.

[20] J.A. Hachtel, J.C. Idrobo, M. Chi, Sub-Ångstrom electric field measurements on a universal detector in a scanning transmission electron microscope, Advanced Structural and Chemical Imaging, 4 (2018) 10.

[21] W. Gao, C. Addiego, H. Wang, X. Yan, Y. Hou, D. Ji, C. Heikes, Y. Zhang, L. Li, H. Huyan, T. Blum, T. Aoki, Y. Nie, D.G. Schlom, R. Wu, X. Pan, Real-space charge-density imaging with sub-ångström resolution by four-dimensional electron microscopy, Nature, 575 (2019) 480-484.

[22] J. Tao, D. Niebieskikwiat, M. Varela, W. Luo, M.A. Schofield, Y. Zhu, M.B. Salamon, J.M. Zuo, S.T. Pantelides, S.J. Pennycook, Direct Imaging of Nanoscale Phase Separation in $La_{0.55}Ca_{0.45}MnO_3$: Relationship to Colossal Magnetoresistance, Physical Review Letters, 103 (2009) 097202.

[23] C. Ophus, Four-dimensional scanning transmission electron microscopy (4D-STEM): From scanning nanodiffraction to ptychography and beyond, Microscopy and Microanalysis, 25 (2019) 563-582.

[24] E. Rauch, M. Véron, Improving angular resolution of the crystal orientation determined with spot diffraction patterns, Microsc Microanal, 16 (2010) 770-771.

[25] O. Panova, C. Ophus, C.J. Takacs, K.C. Bustillo, L. Balhorn, A. Salleo, N. Balsara, A.M. Minor, Diffraction imaging of nanocrystalline structures in organic semiconductor molecular thin films, Nature Materials, 18 (2019) 860-865.

[26] D.N. Johnstone, F.C.N. Firth, C.P. Grey, P.A. Midgley, M.J. Cliffe, S.M. Collins, Direct Imaging of Correlated Defect Nanodomains in a Metal–Organic Framework, J Am Chem Soc, 142 (2020) 13081-13089.

[27] J.M. Zuo, J. Zhang, W.J. Huang, K. Ran, B. Jiang, Combining Real and Reciprocal Space Information for Aberration Free Coherent Electron Diffractive Imaging Ultramicroscopy, 111 (2011) 817-823.

[28] Y. LeCun, Y. Bengio, G. Hinton, Deep learning, Nature, 521 (2015) 436-444.

CHAPTER 6

CONCLUSIONS AND FUTURE PERSPECTIVES

6.1. Conclusions

In this thesis, we have outlined several novel approaches for quantitative analysis of crystal lattice and defects at nanoscale based on SEND and advanced data analysis of SEND datasets. These methods take advantage of the high spatial resolution of SEND and extract quantitative information from the geometry and intensity of Bragg diffraction and diffuse scattering in END patterns. More specifically:

1) We have developed a strategy for high resolution strain mapping based on SEND. The key to achieve high measurement precision in strained samples, while pushing for high spatial resolution using a convergent beam, is to develop an intensity insensitive method for diffraction disk detection. A method using circular Hough transform to detect the diffraction disks is proposed. A weighted 2D lattice fitting is designed to calculate the deformation matrix and strain, from the detected disk positions. The method is applied to measure strain in a FinFET device at the spatial resolution of 1 nm. The effect of sample orientation, thickness, and strain field distribution on the strain measurement accuracy are examined based on the multislice simulations. The strain measurement precision is estimated by a calibration experiment on an unstrained region of the sample, as well as analytically from the diffraction patterns directly. Different experimental conditions are explored to provide a guideline for the optimal strain measurement strategy: signal-to-noise ratio of the diffraction pattern should be larger than 100 and camera length should be as large as there are enough diffraction disks to calculate the deformation matrix. We also pointed out the difference in diffraction from the uniformly strained and non-uniformly strained regions.

2) We have provided two examples of machine learning assisted electron diffraction pattern analysis, and how such analysis is incorporated with SEND. The first example is a simple artificial neural network designed to determine crystal orientation based on the integrated diffraction disk intensities instead of the whole pattern. We demonstrated that it is possible to achieve faster and more accurate determination of small orientation change in a GaSb thin sample compared with the traditional correlation-based pattern matching. The method is applied to characterize the misorientation of grain subdivision in a sample of irradiated UO_2. The results clearly show the spatial distribution of multiple small grains sharing low-angle grain boundaries less than 2° with each other. The second example is a convolutional neural network designed to measure diffraction disk position from the pattern. Since this method works on small sub-images, the network structure can be simplified to expedite both model training and processing of the experimental data. The application of the trained convolutional neural network to the measurement of strain fields in a FinFET device shows comparable results as previously calculated by the circular Hough transform method and has better precision in some cases. The training of all these neural networks is possible with accurate electron diffraction simulation using dynamical diffraction theory.

3) We have applied different techniques to image and characterize different types of defects in SiGe. First, we used microprobe STEM imaging, which takes advantage of the diffraction contrast in END and fast acquisition speed of HAADF detector. By varying convergence angle and collection angle, microprobe STEM imaging can provide contrast from defects similar to DF diffraction contrast imaging, but with more flexibility as a method to overview the sample and quick navigate to the region of interest. Next, high precision strain mapping is carried out near a dislocation core. When compared with modelling using elasticity theory, we demonstrated that the

extended strain fields of a dislocation core can be precisely measured by our technique. To quantitatively analyze electron diffuse scattering, we introduced the technique of Cepstral STEM imaging. Severely distorted lattice can be imaged by calculating Cepstral difference between a local diffraction pattern and the average pattern in a 4D-DD. Based on the Cepstral STEM imaging results, we further showed that a convolution neural network can be trained to automatically differentiate directional or nondirectional defects by learning from the features in diffuse scattering.

In summary, our results show that 4D-DDs of SEND with non-overlapping diffraction disks contain rich structural information of materials. To achieve quantitative analysis of 4D-DDs, algorithms must be designed carefully to separate the effects of Bragg diffraction geometry, dynamical diffraction induced intensity, and diffuse scattering. With the help of accurate electron diffraction simulation using dynamical diffraction theory, we also demonstrated that supervised machine learning based automated analysis of large 4D-DDs has great potential to further push the limit of SEND applications.

6.2. Future Perspectives

6.2.1. Ultimate strain mapping techniques

In our study, the best precision of strain mapping is achieved on samples with high crystallinity. The best scenario is that the illuminated volume by the electron probe can be approximated by a single crystal. When the length scale of strain variation is comparable to the probe size, or abrupt change in crystal structures occurs at defects or interfaces, the Bragg diffraction becomes less well-defined [1, 2]. Edge methods for disk detection, like circular Hough transform, may produce noisy results or fail. Finding a better way to perform reliable strain measurement close to material interfaces is an important next step for SEND-based strain analysis.

The spatial resolution of SEND strain mapping is currently limited by the size of the electron probe, as only the average lattice information from Bragg diffraction is obtained. Using Cepstral analysis, we have shown that the severe lattice distortion can be related to diffuse scattering. Further increasing the strain mapping resolution may ultimately rely on diffuse scattering. When using a step size much smaller than the probe size in an oversampling scheme, ptychography has achieved super resolution for atomic resolution imaging [3]. But ptychography-based strain mapping has not yet been demonstrated in electron microscopy with strong dynamical diffraction from thick samples.

So far, the strain mapping techniques we talked about measure strain fields in a 2D projection. In a typical SEND setting, depth of focus is usually larger than the sample thickness. Thus, the recorded diffraction pattern contains averaged information along the thickness direction. To resolve the strain fields in 3D, diffraction tomography may be used [4]. This can be challenging as a successful reconstruction heavily relies on the conditions including minimal missing wedge, high precision in 2D strain measurement at different tilting angles, and good alignment between 2D maps at different angles.

6.2.2. Machine learning / deep learning assisted analysis of 4D-DDs

In this thesis, we demonstrated that machine learning can be used to predict precision orientation, diffraction disk position, and defect type from END patterns. They are all supervised learning methods, which rely on large number of accurately simulated diffraction pattern as training data. To achieve better performance with machine learning assisted analysis of 4D-DDs, a number of questions need to be addressed:

1) How to simulate diffraction patterns close enough to the experimental ones so that the neural networks are not just learning the features from those overidealized patterns?

2) How to simulate a humongous number of diffraction patterns efficiently to meet the requirements of the training data?

3) What is the best configuration of the neural networks for 4D-DDs? This cannot be directly copied from the popular models used in computer vision as real-life pictures are completely different from electron diffraction patterns.

Beyond supervised learning which is designed to focus on certain cases included in the training data, unsupervised learning may also have some advantages in effective reduction of the ever increasing size of 4D-DDs [5].

Finally, quantitative CBED has been shown to fully utilize the intensity information in diffraction to reconstruct structure factors [6, 7]. Machine learning may provide a more efficient way to refine a large number of parameters.

6.2.3. Phase mapping from electron diffraction with multiple scattering

In this thesis, we only utilized the modulus of the scattered wave from the sample, which is what recorded in a diffraction pattern, while the phase information is lost. It was shown that under certain conditions, phase retrieval is possible with electron diffraction [8, 9]. When using 4D-STEM, ptychography has been demonstrated to reconstruct phase maps from 2D materials based on the kinematical diffraction assumption [3]. With a thick sample, however, multiple scattering is inevitable, which prohibits the direct usage of ptychographic reconstruction algorithms. Multislice ptychography has been proposed to overcome this issue by separating a thick sample into a number of thin slices and backpropagate the electron beam in an inverse way as of multislice simulation [10]. Once the phase map is obtained, it may be possible to reconstruct electric field in the sample which can then be used to characterize and image active dopants.

6.3. References

[1] C. Mahr, K. Muller-Caspary, T. Grieb, M. Schowalter, T. Mehrtens, F.F. Krause, D. Zillmann, A. Rosenauer, Theoretical study of precision and accuracy of strain analysis by nano-beam electron diffraction, Ultramicroscopy, 158 (2015) 38-48.

[2] C. Mahr, K. Muller-Caspary, T. Grieb, F.F. Krause, M. Schowalter, A. Rosenauer, Accurate measurement of strain at interfaces in 4D-STEM: A comparison of various methods, Ultramicroscopy, 221 (2021).

[3] Y. Jiang, Z. Chen, Y.M. Hang, P. Deb, H. Gao, S.E. Xie, P. Purohit, M.W. Tate, J. Park, S.M. Gruner, V. Elser, D.A. Muller, Electron ptychography of 2D materials to deep sub-angstrom resolution, Nature, 559 (2018) 343-+.

[4] R. Tovey, D.N. Johnstone, S.M. Collins, W.R.B. Lionheart, P.A. Midgley, M. Benning, C.B. Schonlieb, Scanning electron diffraction tomography of strain, Inverse Probl, 37 (2021).

[5] B. Martineau, D.N. Johnstone, A.T.J. van Helvoort, P.A. Midgley, A.S. Eggeman, Unsupervised machine learning applied to scanning precession electron diffraction data, Adv Struct Chem Imag, 5 (2019).

[6] J.M. Zuo, M. Kim, M. O'Keeffe, J.C.H. Spence, Direct observation of d-orbital holes and Cu-Cu bonding in Cu2O, Nature, 401 (1999) 49-52.

[7] J.M. Zuo, Measurements of electron densities in solids: a real-space view of electronic structure and bonding in inorganic crystals, Rep Prog Phys, 67 (2004) 2053-2103.

[8] J.M. Zuo, I. Vartanyants, M. Gao, R. Zhang, L.A. Nagahara, Atomic resolution imaging of a carbon nanotube from diffraction intensities, Science, 300 (2003) 1419-1421.

[9] W.J. Huang, R. Sun, J. Tao, L.D. Menard, R.G. Nuzzo, J.M. Zuo, Coordination-dependent surface atomic contraction in nanocrystals revealed by coherent diffraction, Nat Mater, 7 (2008) 308-313.

[10] S. Gao, P. Wang, F.C. Zhang, G.T. Martinez, P.D. Nellist, X.Q. Pan, A.I. Kirkland, Electron ptychographic microscopy for three-dimensional imaging, Nat Commun, 8 (2017).

APPENDIX A

OPERATION MANUAL FOR SCANNING ELECTRON NANODIFFRACTION

This operation manual details the procedure of performing scanning electron nanodiffraction (SEND) or four-dimensional scanning transmission electron microscopy (4D-STEM) in a Thermo Fisher Scientific microscope. The examples used throughout this manual are given based on the Thermo Fisher Scientific Themis Z Aberration-Corrected (Scanning) Transmission Electron Microscope installed at Materials Research Laboratory at University of Illinois Urbana-Champaign. But in principle, it can be extended to most of the transmission electron microscopes manufactured by Thermo Fisher Scientific (formerly FEI). The major mode used for SEND/4D-STEM applications is called microprobe STEM (μP STEM) mode. Most of the electron beam alignment for SEND should be done in vacuum if possible. The entire process is estimated to take around 0.5~1 hour depending on the initial condition and user experience.

A.1. Align Microscope for Microprobe STEM

Load alignment files

1. Load full alignment for STEM mode

2. Load FEG register for μP-STEM or STEM mode (see Steps 4 and 5 for adjusting the convergence angle).

3. Find beam (if no beam on flu-cam)

   a. Make sure the sample holder is fully inserted, the sample grid is not blocking the beam, and correct detector is inserted.

b. Go to **Mono** tab > **Monochromator** > **Find beam**.

c. After finish, check if these settings are correct: aperture C2 should be 50 µm; spot size should be 9 (if not, go to **Beam settings** > **Spot number** to change).

d. (Optional) Manually center the beam if needed. Activate **Monochromator Tune** > **Shift & Focus**. Use **MF-X, MF-Y** knobs to shift beam. Use **Intensity** knob to change focus of beam. The screen current with 50 µm C2 aperture should be around 0.01~0.03 nA, depending on the sample.

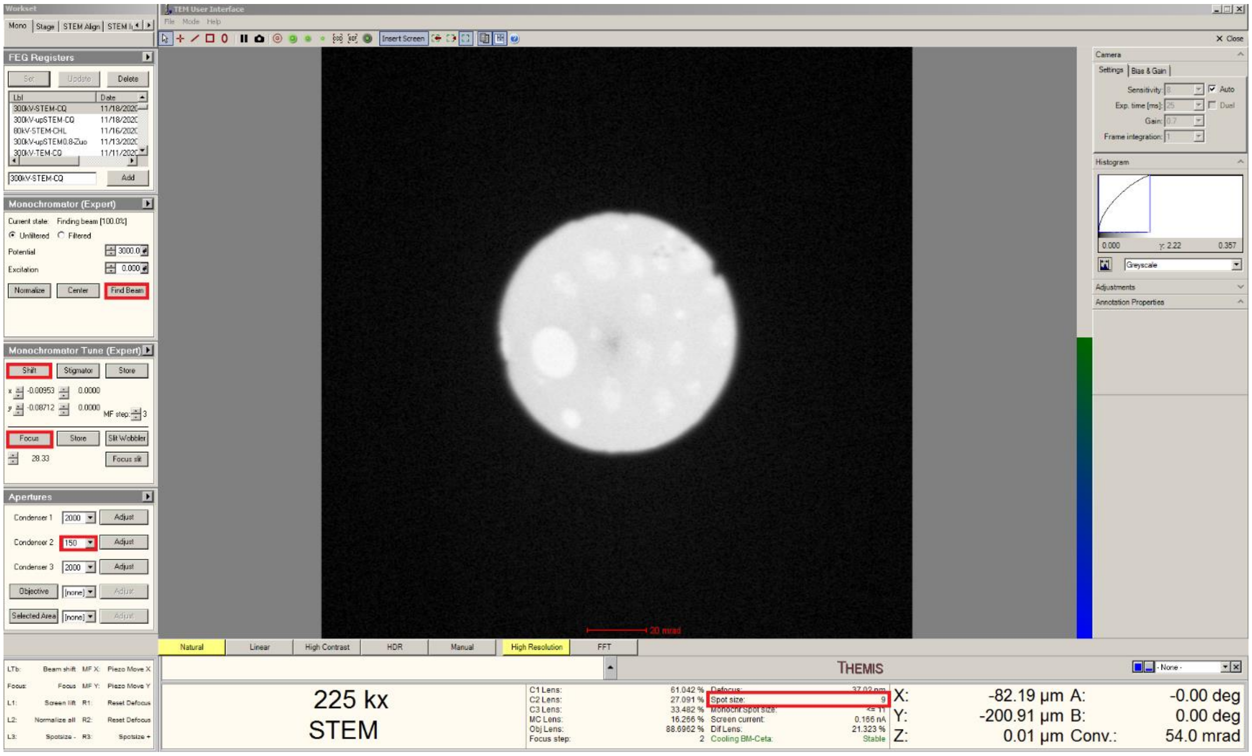

Lbl	Date
300kV-STEM-CQ	11/18/2020
300kV-upSTEM-CQ	11/18/2020
80kV-STEM-CHL	11/16/2020
300kV-upSTEM0.8-Zuo	11/13/2020
300kV-TEM-CQ	11/11/2020

Current state: Finding beam [100.0%]
● Unfiltered ○ Filtered
Potential 3000.0
Excitation 0.000

x -0.00953 0.0000
y -0.08712 0.0000 MF step: 3
Focus 28.33

Condenser 1 2000
Condenser 2 150
Condenser 3 2000
Objective [none]
Selected Area [none]

LTb:	Beam shift	MF X:	Piezo Move X
Focus:	Focus	MF Y:	Piezo Move Y
L1:	Screen lift	R1:	Reset Defocus
L2:	Normalize all	R2:	Reset Defocus
L3:	Spotsize -	R3:	Spotsize +

225 kx
STEM

C1 Lens:	61.042 %	Defocus:	37.02 nm
C2 Lens:	27.091 %	Spot size:	9
C3 Lens:	33.482 %	Monochr.Spot size:	<= 11
MC Lens:	16.266 %	Screen current:	0.166 nA
Obj Lens:	88.6962 %	Dif Lens:	21.323 %
Focus step:	2	Cooling BM-Ceta:	Stable

X:	-82.19 µm	A:	-0.00 deg
Y:	-200.91 µm	B:	0.00 deg
Z:	0.01 µm	Conv.:	54.0 mrad

Fig. A.1. Set up alignment for microprobe STEM.

Set the Convergence Angle

4. Switch to µP-STEM mode

   a. Switch to STEM mode: go to **STEM Align** tab > **STEM Imaging**, activate **STEM** button.

   b. Switch to µP-STEM mode: go to **Stage** tab > **Beam Settings**, activate **Free Ctrl** button. In **FreeCtrl** panel of the flap-out, Mode switch to **Probe**, Minicondensor switch to **Microprobe**, Angle range switch to **Large**.

5. Set convergence angle as desired

   a. Go to **Stage** tab > **Beam settings** > **Free Ctrl**, and select **MF-Y Convergence angle**, use **MF-Y** knob to adjust convergence angle.

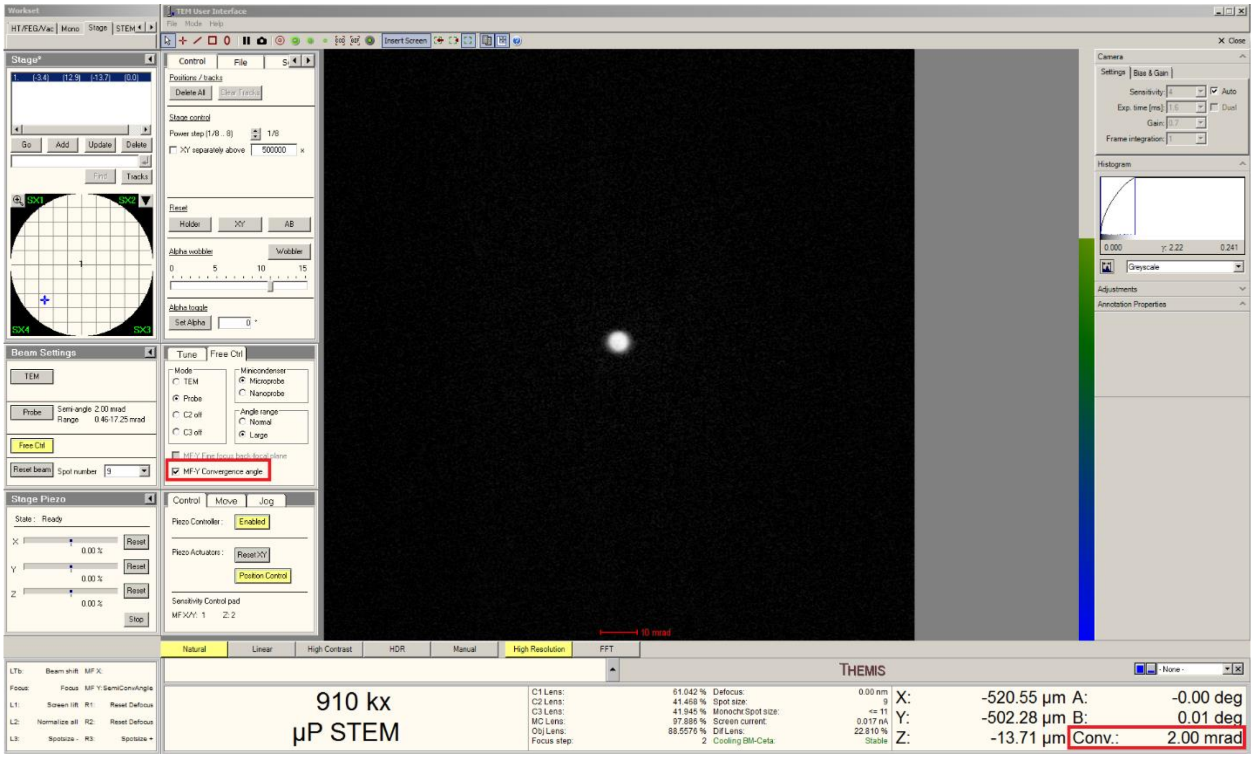

Beam Settings

Semi-angle 2.00 mrad

Range 0.46-17.25 mrad

Spot number 9

Mode: ○ TEM ● Probe ○ C2 off ○ C3 off

Minicondenser: ● Microprobe ○ Nanoprobe

Angle range: ○ Normal ● Large

☐ MF-Y Fine focus back-focal plane

☑ MF-Y Convergence angle

Stage Piezo

State : Ready

Piezo Controller : Enabled

Sensitivity Control pad

MF X/Y: 1 Z: 2

910 kx

µP STEM

C1 Lens:	61.042 %	Defocus:	0.00 nm
C2 Lens:	41.468 %	Spot size:	9
C3 Lens:	41.945 %	Monochr.Spot size:	<= 11
MC Lens:	97.886 %	Screen current:	0.017 nA
Obj Lens:	88.5576 %	Dif Lens:	22.810 %
Focus step:	2	Cooling BM-Ceta:	Stable

X:	-520.55 µm	A:	-0.00 deg
Y:	-502.28 µm	B:	0.01 deg
Z:	-13.71 µm	Conv.:	2.00 mrad

Fig. A.2. Set the convergence angle.

Press button to switch to the following modes:

- Diffraction Mode → Light On (As shown)
- Probe Mode → Light Off

Fig. A.3. Switch to probe mode.

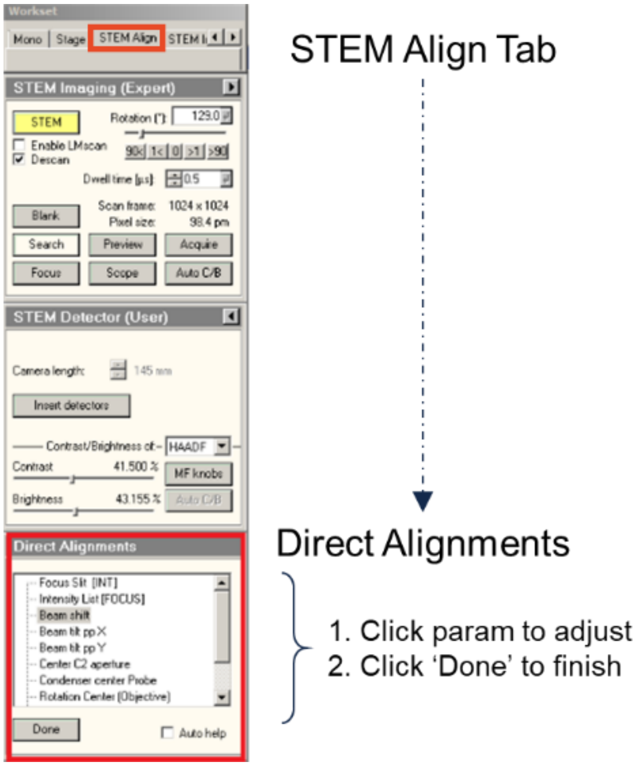

Rotation (°) 129.0

☐ Enable LMscan

☑ Descan

Dwell time [µs] 0.5

Scan frame: 1024 x 1024

Pixel size: 98.4 pm

Camera length: 145 mm

Contrast/Brightness of: HAADF

Contrast 41.500 %

Brightness 43.155 %

☐ Auto help

STEM Align Tab

Direct Alignments

1. Click param to adjust
2. Click 'Done' to finish

Fig. A.4. Direct alignments.

μP STEM Mode: Probe Alignment

6. Go to probe mode (i.e., deactivate **Diffraction** button)

7. Adjust the magnification until you can see the beam.

8. Go to **STEM align** tab > **Direct Alignments**

9. Activate **Beam shift** to center the beam in screen (go to lower mag if cannot see beam)

10. Activate **Intensity list (FOCUS)**, use **focus** knob to focus the beam to its smallest size.

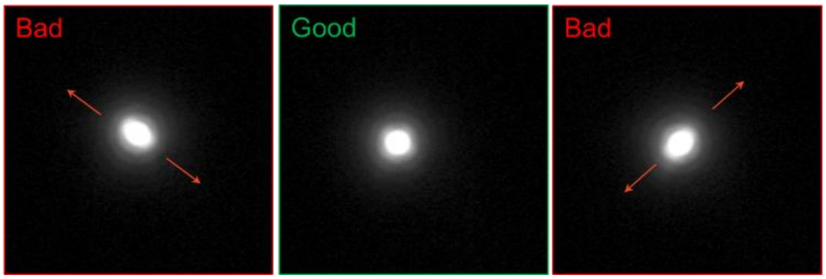

Fig. A.5. Focus the probe with intensity list.

11. Go to **Stigmator** > **Condenser**, use **MF-X** and **MF-Y** to make the beam circular (a little bit three-fold symmetry). The interference fringes shown below are an indicator of good alignment.

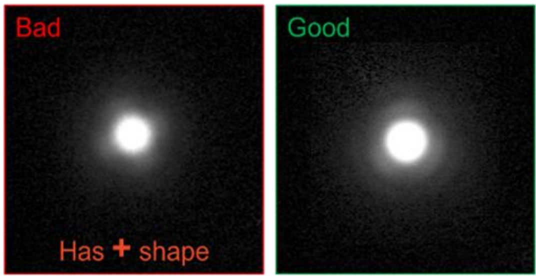

Fig. A.6. Correct astigmatism.

12. Activate **Beam tilt pp X/Y**, use **MF-X** and **MF-Y** to make two beams overlap.

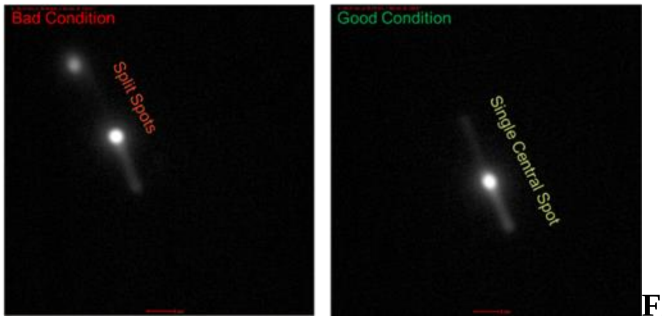

Fig. A.7. Pivot point alignment.

13. Activate **Rotation Center (Objective)**, use **MF-X** and **MF-Y** to make beam stable.

14. Repeat 9-13 until the beam is stable.

µP STEM Mode: Descan Alignment

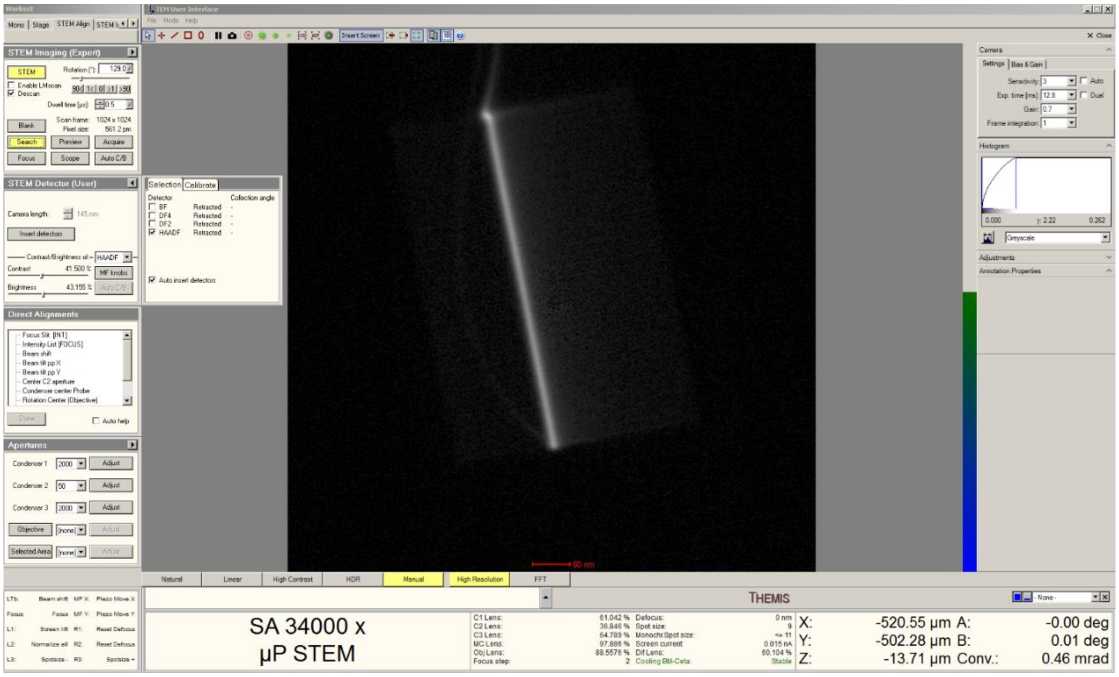

SA 34000 x
µP STEM

C1 Lens: 61.042 %
C2 Lens: 36.846 %
C3 Lens: 64.789 %
MC Lens: 97.886 %
Obj Lens: 88.5576 %
Focus step: 2
Defocus: 0 nm
Spot size: 9
Monocht Spot size: <= 11
Screen current: 0.015 nA
Dif Lens: 60.104 %
Cooling BM-Ceta: Stable
X: -520.55 µm A: -0.00 deg
Y: -502.28 µm B: 0.01 deg
Z: -13.71 µm Conv.: 0.46 mrad

Fig. A.8. Descan alignment.

15. Activate **Diffraction** mode and go to 160k× magnification and start scan (Click **Search** button in **STEM align** tab).

16. Go to probe mode and go to low enough mag to ensure the entire scanning beam is visible.

17. In **Direct Alignment** panel, use **Descan shift line/frame** to make the beam a stationary spot. The beam constantly moving across the screen indicates poor alignment in **shift line** (slow scan direction). An extended line of beam instead of a spot indicates poor alignment in **shift frame** (fast scan direction).

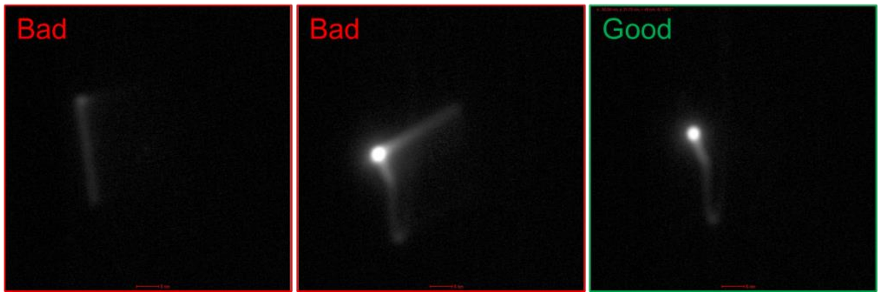

Fig. A.9. Descan alignment conditions.

18. Go to diffraction mode, **Direct Alignment** > **Descan pivot point** to make diffraction stable when scanning.

µP STEM Mode: Measure the Probe / Verify Alignment

19. Go to probe mode.

20. Go to **Camera** tab > **CCD/TV Camera**

21. Set a small integration time (<0.05 s) and large frames combined (50~100) to protect CCD from the strong beam.

22. Perform the following steps reasonably quickly to minimize CCD exposure to the direct beam:

   a. Start **Search**

   b. Lift screen (deactivate **Insert Screen** button on the flu-cam)

   c. Stop **Search** when you see the probe on the CCD.

   d. **Insert Screen** to protect the CCD.

23. Draw a **Line Profile** (Unary operation) across the center of the probe, and measure FWHM of the probe using **Energy Window Tool**. Change the CCD settings if the peak is saturated.

24. At 300kV, for convergence angle of 0.46 mrad, FWHM should be about 1.7-1.8 nm. For convergence angle of 0.8 mrad, FWHM should be about 1.1-1.2 nm. If larger than this range significantly, refine the µP STEM alignment.

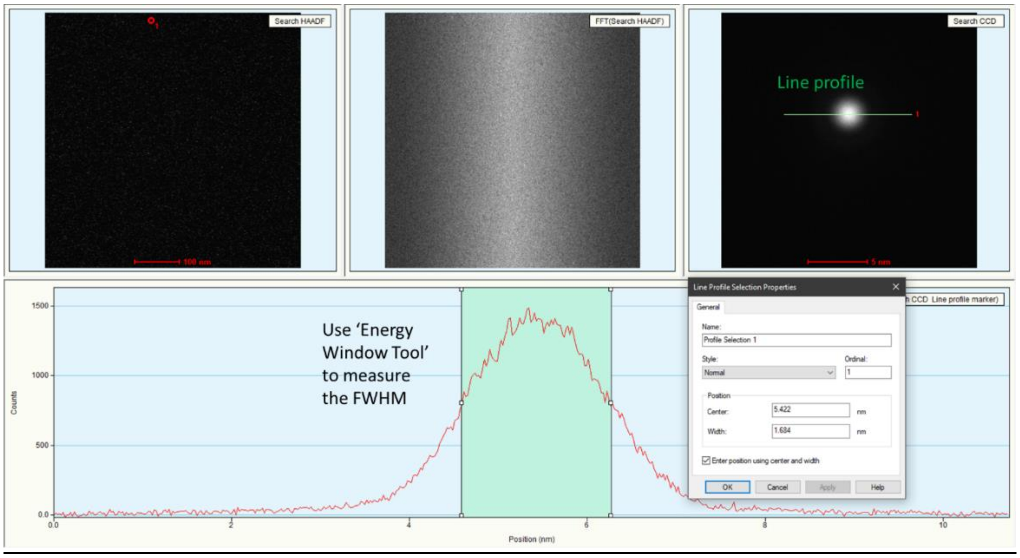

Name: Profile Selection 1
Style: Normal
Ordinal: 1
Position
Center: 5.422 nm
Width: 1.684 nm
☑ Enter position using center and width

Fig. A.10. Measure probe size.

A.2. Collect 4D Electron Diffraction Datasets

Adjust the Sample Height

25. Place beam on the point of interest.


1. Click the 'Beam Position Marker Tool'

2. Click on the 'Search HAADF' on the 'O_1' and drag to point of interest

Fig. A.11. Place beam on the point of interest.

26. Go to probe mode.

27. Adjust the Z-height until the beam becomes a focused spot instead of a diffraction-like feature. When the sample is tilted to high angle, the beam may not be focused perfectly at any Z-height, find the best possible condition instead.

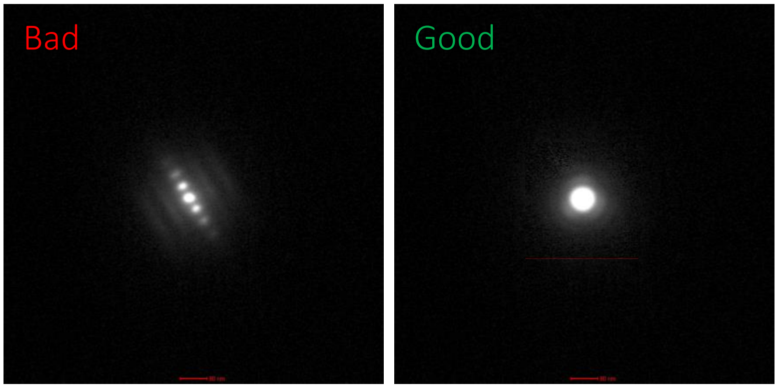

Fig. A.12. Adjust sample height.

Test camera settings

28. In diffraction mode, go to **Camera** tab > **CCD/TV Camera**

29. Select BM-Ceta as acquisition camera. Make sure **Insert** button is activated.

30. For typical drift corrected SEND, use the following settings:

    a. **Integration time**: 0.1 s

    b. **Sampling**: 1

    c. **Readout area**: Quarter (when drift correction is applied, HAADF detector will block the CCD area outside the quarter region)

31. In flap-out, switch Settings to **Acquire** mode. Adjust **Frames combined** according to beam dose (select **Medium dose** for common cases). **Readout mode** to High Speed for fast scanning.

32. Acquire an image of the diffraction pattern to see if all parameters are optimized and adjust camera length and shift the direct beam to center of the CCD (**Direct Alignments** > **Diffraction alignment**) as needed.

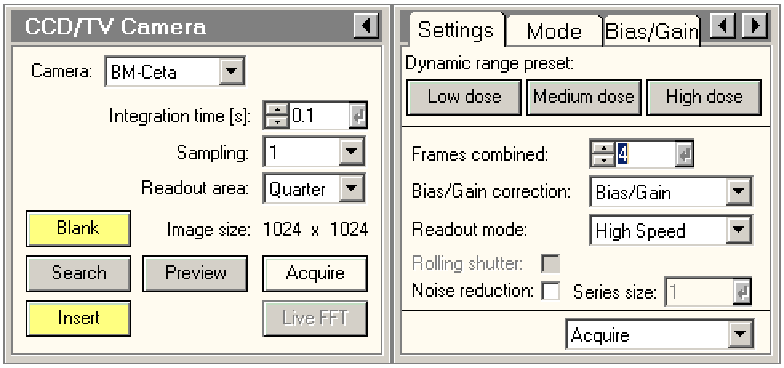

Camera: BM-Ceta
Integration time [s]: 0.1
Sampling: 1
Readout area: Quarter
Image size: 1024 x 1024

Frames combined: 4
Bias/Gain correction: Bias/Gain
Readout mode: High Speed
Rolling shutter: ☐
Noise reduction: ☐ Series size: 1
Acquire

Fig. A.13. Test camera settings.

Configure SEND Acquisition

33. Acquire an image of the region of interest using **STEM Imaging**

34. Go to **STEM EDS** panel > **Experiments** > **SpectrumCollection** > **Drift corrected spectrum image**

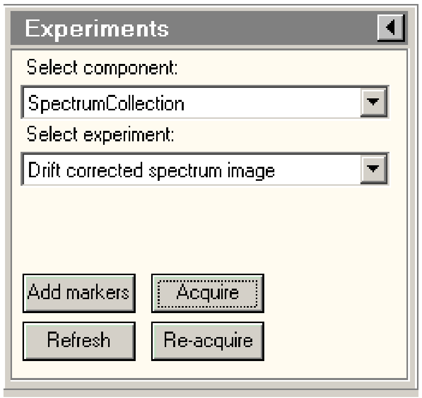

Select component: SpectrumCollection
Select experiment: Drift corrected spectrum image

Fig. A.14. SEND acquisition.

35. Click **Add markers** button, select region to scan. Double click the box to set the size of the box accurately.

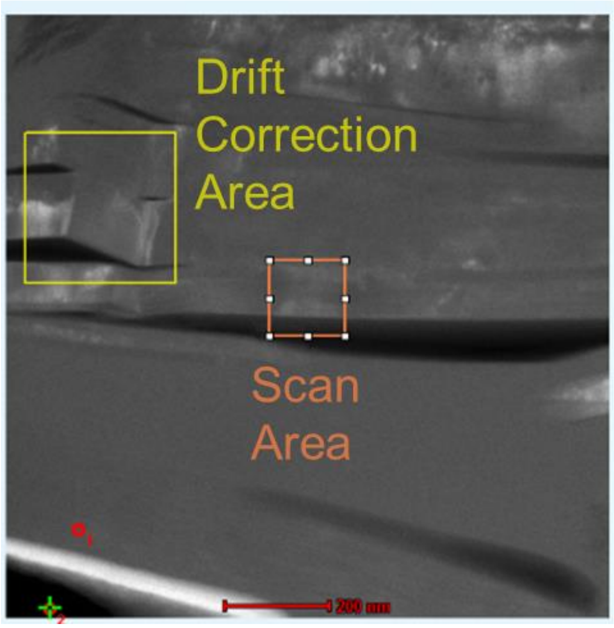

Fig. A.15. Set up scan and drift correction.

36. In **Experiments** > **Settings**, update the scan parameters accordingly:

Parameter	Description
Image Size (X) and <...> (Y)	Scan steps in X and Y
Dwell time (ms)	Set to 100 to match with the 0.1s of the integration time of camera
Acquire Ccd images	Set to 'Yes' to enable diffraction acquisition with CCD
Number of Acquisitions in Slice	How many frames before checking drift (usually set to ***equal*** Image Size X)
Number of Slices per Reference	How many checks before taking a new reference image (usually set to a number ***larger than*** Image Size Y to avoid multiple references in one scan)

Tab. A.1. Parameters for SEND acquisition.

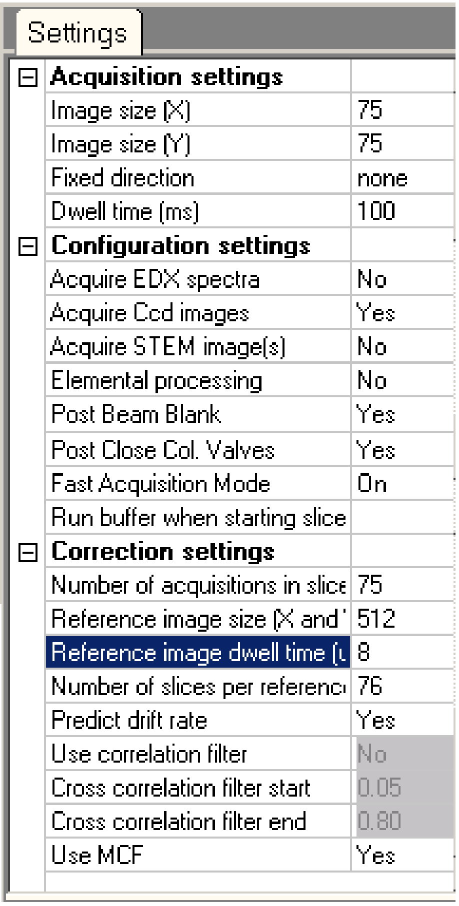

⊟ **Acquisition settings**	
Image size (X)	75
Image size (Y)	75
Fixed direction	none
Dwell time (ms)	100
⊟ **Configuration settings**	
Acquire EDX spectra	No
Acquire Ccd images	Yes
Acquire STEM image(s)	No
Elemental processing	No
Post Beam Blank	Yes
Post Close Col. Valves	Yes
Fast Acquisition Mode	On
Run buffer when starting slice	
⊟ **Correction settings**	
Number of acquisitions in slic	75
Reference image size (X and	512
Reference image dwell time (	8
Number of slices per referenc	76
Predict drift rate	Yes
Use correlation filter	No
Cross correlation filter start	0.05
Cross correlation filter end	0.80
Use MCF	Yes

Fig. A.16. Parameters for SEND acquisition.

Start Data Acquisition

37. Lift the screen.

38. Click **Acquire** button to start acquisition.

APPENDIX B

IMTOOLBOX: STRAIN ANALYSIS SOFTWARE FOR FOUR-DIMENSIONAL DIFFRACTION DATASETS

imToolBox is a software package developed to facilitate analysis of large four-dimensional diffraction datasets (4D-DDs) collected by scanning electron nanodiffraction (SEND) or 4D-scanning transmission electron microscopy (4D-STEM) techniques with focus on strain analysis. The main features of *imToolBox* include:

1. Support mainstream data formats (ser/dm3/dm4/etc.) of 4D-DDs even when the data file is much larger than the memory size.
2. Easy visualization and preprocessing of 4D-DDs.
3. Strain analysis with numerous options and diagnostic tools for the best results.

Installing imToolBox

1. Download and install Matlab Runtime Version: R2020a (9.8) from https://www.mathworks.com/products/compiler/mcr.html
2. Download imToolBox.exe and save to any directory.

Loading 4D-DDs

There are three major ways to read 4D-DDs into *imToolBox*:

1. Reading the 4D-DDs contained in a single data file entirely into memory. Data format supported: ser, dm3, dm4, mrc, avi, dfp, img.

2. Reading only a small chunk of the dataset currently being processed instead of the entire file into memory. This works best when the data file is too large to fit in the memory at once. Data format supported: ser, dm4.
3. Reading a series of image files numbered in sequence. Data format supported: tiff, bmp, jpg, png.

Preprocessing 4D-DDs

A number of functions are included in *imToolBox* for preprocessing of 4D-DDs, including contrast/gamma adjustment, binning, cropping, masking, and aligning diffraction patterns for imperfect descan. Diffraction pattern alignment works by doing cross-correlation of the transmitted beams from different patterns to calculate relative shift in the diffraction pattern. The shift values can be stored in a separate file without modifying the raw data and can be loaded by the software when the data file is closed and opened again.

Visualizing 4D-DDs

To easily visualize large 4D-DDs, we provide methods including:

1. Virtual bright/dark-field (VB/DF) imaging: place a circular detector of any radius at any desired position of the diffraction pattern to integrate all intensities within the detector. VB/DF images can be generated to provide an overview of the sample with diffraction contrast.
2. Virtual annular dark-field (VADF) imaging: place a customized annular dark-field detector on the diffraction pattern to integrate all intensities within the detector

region. VADF images also provide overview of the sample to compare with ADF images acquired by physical ADF detectors to examine sample drift.

3. Stack averaging: average all diffraction patterns in 4D-DDs.
4. Diffraction pattern grouping: use an unsupervised machine learning method, K-means clustering, to group diffraction patterns based on their similarity (defined by correlation).

Strain Analysis

Choose from different strain analysis schemes:

1. One pair: calculate one-dimensional strain from the distance of a pair of diffraction peaks.
2. Center 3x3: calculate two-dimensional strain components by fitting a reciprocal lattice to the center beam and 8 diffracted beams around it.
3. All: calculate two-dimensional strain components by fitting a reciprocal lattice to all diffraction peaks detectable in the pattern.
4. Center 6: calculate two-dimensional strain components but with focus on just one direction.

Choose from different methods to measure diffraction peak positions:

1. Circular Hough transform: fit a circle to the edge of the diffraction disk to find the center position. Works best with large diffraction disks.
2. Template matching: find the position of the diffraction peak by doing cross-correlation with a template. Works best when all diffraction peaks have similar intensity distribution: spot patterns or kinematic disk patterns.

3. Peak fitting: use Gaussian or Lorentzian peak fitting to find the peak position. Works best with spot patterns from parallel illumination.
4. Neural network: use trained convolutional neural networks to find the position of diffraction peaks. Requires network training for different experimental conditions.

Full diagnostic capability:

1. Output peak detection and lattice fitting results with estimated uncertainty.
2. Display all intermediate steps of detection to help pinpoint the error-causing issue.
3. Process only a selected range of the dataset to save time.

Versatile calculation and display of strain maps:

1. Define reference for strain calculation by choosing one pattern or average over a range of patterns in the dataset.
2. Define x direction for strain calculation.
3. Plot the strain results in 2D maps or 1D profile.
4. Adjust display range of strain maps.